Alma Mater Studiorum · Università di Bologna

School of Science
Department of Physics and Astronomy
Master Degree Programme in Astrophysics and Cosmology

A new method of stellar spectra extraction from MUSE data cube in an high sky emission region: the complex case of Trumpler 14

Graduation Thesis

Supervisor:
Prof. Leonardo Testi

Co-supervisors:
Dr. Giacomo Beccari
Dr. Dominika Itrich

Submitted by:
Giuseppe Milazzo

Academic Year 2022/2023
Graduation date III

Abstract

The formation of planetary systems is an important topic still at the center of the scientific research. Understanding how planets form is strictly linked to knowing what the origins of our Solar System are and, in particular, the study of protoplanetary discs (PPD) is fundamental. Most of the detailed studies on protoplanetary discs so far have focused on nearby star-forming regions, these are not really representative of the environment where most stars (and therefore planets) form. Most stars form in star clusters, and in this case the environment can have a strong effect on the development and life of the discs. For this reason it is important to study how discs evolve in young star clusters. The time factor is important because the lifetime of the discs is very short, the classical lifetime is of the order of Myrs. Many factors take part in the discs' evolution and one of the most important ones is the external photoevaportation, which is due to the presence of hot stars emitting a large amount of high-energy photons. This emitted radiation is able to photoevaporate the discs of the nearby stars. This means that there are regions in stellar clusters in which the formation of planets is strongly dependent on the presence of those hot stars. This work aims to study the external photoevaporation effect. The object at the center of the discussion is the open cluster Trumpler 14 (Tr 14) located in the Carina star forming region. This is one of the youngest clusters known in astronomy, in fact its age is about 1Myr. The observations are made with MUSE, that is an instrument mounted at the Very Large Telescope (VLT). This instrument is essential for the study because the goal of the work is to extract spectra of the stars, as well as the emission lines originated from the disc-star interaction and the disc-photoevaporation. The main problem is the behaviour of the background because, in the regions taken into account, the sky around the stars that we aim to observe is emitting in a non homogenous way and so it cannot be easily subtracted from the stellar spectra. The main contribution to the sky emission is caused by the radiation of the massive stars of the cluster. These stars create a region of ionized gas emitting in the lines that are also used as main diagnostics for star-disc interaction and photoevaporation. This work also aims at finding a method to optimize stellar spectra extraction in the case of this particular and hostile situation. The interest of producing those spectra is to make an accurate spectral classification of the stars and provide a robust estimate of their emission lines. By applying our new method to one of the MUSE fields in Tr14, we were able to detect [OI]$\lambda 6300\mathring{A}$ emission in 4 out of 141 stars. For two of these detection the measured flux is found to be very uncertain due to the remaining noise from the sky subtraction. By comparing with external photoevaporation models, we find that the observed fluxes from these four stars are consistent with relatively large discs ($\sim$ 100AU radius), while the upper limits measured on the other stars suggest that most of them have already lost the outer discs to photoevaporation. Finding an effective method to extract stellar spectra will play an important role for the future analysis of protoplanetary discs in this and similar region. The next step in this research will be to apply the method to the full cluster observations and derive the survival rate of outer discs in Tr 14 as a function of the far ultraviolet (FUV) field.

Contents

Chapter 1

Introduction

During a clear night it's possible to see hundreds of stars, when the eyes adapt to the darkness of the night also the fainter stars appear. So the number of the stars increases more and more and counting them is an impossible task. The experience to watch this show is flabbergasting and overwhelming. The truth is that the stars above us are only a very small part of our galaxy. The Milky Way contains hundreds of billions of stars. Imagining this quantity is impossible for our mind. Now it's reasonable to suppose that it is common that stars have planets around them. So the number of planets in our galaxy is bigger than of the stars. For a long time our knowledge about planets was small and only in the recent times the scientific research could study these objects. A very interesting subject is how planets form. Nowadays the knowledge about this topic is progressively growing and it's possible to give it a physical description. Firstly, it is well known that planets form around stars, for this reason is important to start the discussion introducing the mechanism that describes star formation.

1.1 Star formation

Star formation is a process that needs the presence of cold neutral medium (CNM) and perturbations (Shu et al., 1987). The CNM is a part of the insterstellar medium (ISM) and it is composed by dust grains and molecules (the most common are hydrogen molecule H_2, carbon monoxide molecule CO). The molecular gas from which stars form is found in molecular clouds. This is the location in which star formation takes place. Stars are the product of the contraction of molecular clouds. It's possible to determine the conditions for the contraction of a cloud that leads eventually to the formation of a star embryo, the protostar. To simplify the calculations let's assume that the cloud is spherical, homogeneous, static (no rotation and self-gravitating) and isothermal with no magnetic fields. The condition, under which the collapse could start, relates the gravitational force of the cloud and the gas pressure. The condition to start the

contraction for a hydrogen molecule of mass H, located at the border of the cloud, can be written as:

$$\frac{GMH}{R} \geq kT \tag{1.1}$$

where M, R and T are the mass, the radius and temperature of the cloud. It's useful to transform this relation into a condition that contains the two fundamental parameters of the environment that are the density ρ and temperature T. From the condition of spherical symmetry the mass can be written as:

$$M = \frac{4}{3}\pi R^3 \rho \tag{1.2}$$

and so the radius is

$$R = \frac{1}{\left(\frac{4\pi}{3}\right)^{\frac{1}{3}}} \frac{M^{\frac{1}{3}}}{\rho^{\frac{1}{3}}} \tag{1.3}$$

knowing that $H = 3.2 \cdot 10^{-24} g$, $G = 6.67 \cdot 10^{-8} dyne \cdot cm^2 \cdot g^{-2}$ and $k = 1.4 \cdot 10^{-16} erg \cdot K^{-1}$, let's substitute R in the relation (1.1) and after some algebraic passages the final relation is find

$$M_J \geq 10^{23} T^{\frac{3}{2}} \rho^{\frac{-1}{2}} [g] \tag{1.4}$$

M_J is defined as Jeans Mass. This relation set the minimum mass at which the collapse can start. So, M_J depends on cloud temperature and density. Looking at the exponents of temperature and density it's possible to affirm that there are privileged conditions under which cloud collapse could happen. In a case of a cloud filled by hot and rare gas the gravitational collapse is very unlike. The Jeans Mass limit is huge, a cloud must have a mass bigger than M_J in order to start the collapse and to win a great thermal energy that tends to expand the cloud. Instead in the case of cold and dense cloud the Jeans Mass is smaller than the previous case. This limit can be exceeded and so it's probable that the contraction could happen. Jeans treatment is useful to specify what are the environment conditions preferred to have star formation. As written above, perturbations are needed in order to have the cloud collapse. The mechanisms which trigger star formation are the following:

1. Shock front (e.g.compression induced by supernovae explosions)
2. Clouds collision
3. Gas compression in the spiral branch
4. Galaxies interaction (e.g. merging)

Until now the discussion was centered on a molecular cloud with particular features. It is important for the analysis introduce a more realistic case. CNM is find in complex structures called *Giant molecular clouds* (GMSs). They contain most of the CNM and their typical mass is $10^4 M_\odot$. GMSs are not homogeneous (Langer et al., 1995; Heithausen et al., 1998), the internal structure is characterised by some overdense regions called *clumps*. *Star forming clumps* are defined as that clumps from which stars form (McKee et al., 2007). *Cores* are the region, inside that clumps, in which individual star or small star systems (e.g. binaries) form (Fig.[1.1, panel 1.]). Star formation is typically divided in two parts: low-mass star formation and high-mass star formation. This work is focused on describing the first one. Low-mass star undergo a pre-main sequence phase.

1.2 Formation of a planetary system

The complexity of the molecular cloud is not only referred to its structure. A realistic case is a molecular cloud with some rotation and magnetic field. The collapse of the cores generates a protostar still embedded in the parental cloud. The newly born star is defined as *Young Stellar Object* (YSO). YSOs are classified in four different classes based on their spectral energy distributions (SED) features which suggest us different stages of evolution. In Fig.[1.1] there is a complete scheme of the evolution of a YSO. The YSO classes are the following:

- **Class 0**: this is the first stage, the protostar has just formed and it is embedded in the parental cloud. The small initial velocity of the cloud is magnified by the collapse and in order to conserve the angular momentum a disc forms around the protostar. The emission of the disc is completely hidden by the cloud, but it is observable at the mm wavelength range (Tobin et al., 2013). The momentum is dissipated via outflows (Frank et al., 2014).

- **Class I**: in this stage the protostar is still enshrouded by optically thick material. In this phase the angular momentum is also dissipated trough outflows (Frank et al., 2014) impacting strongly on the ambient medium. The momentum excess is also dissipated trough viscous processes which drive accretion onto the protostar (see next section).

- **Class II**: this is the classical TTauri (cTT) phase. Due to the envelope dissipation the protostar becomes visible in the optical band, but reddened. The PPD is composed by dust and gas and it is optically thick and evolves viscously (see next section). The cTT is still accreting material from the disc.

- **Class III**: this is the last stage in which the PPD is depleted. The protostar is no more accreting and it is classified as an evolved TTauri.

It is not clearly understood in which phases planets formation starts. But it is sure that planets formation needs a dusty disc. The process of formation can be model in two ways: core accretion scenario, in which solid particles accrete others particle till they form a planet; or disc fragmentation scenario, planets form by fragmentation from a massive and gravitationally unstable disc.

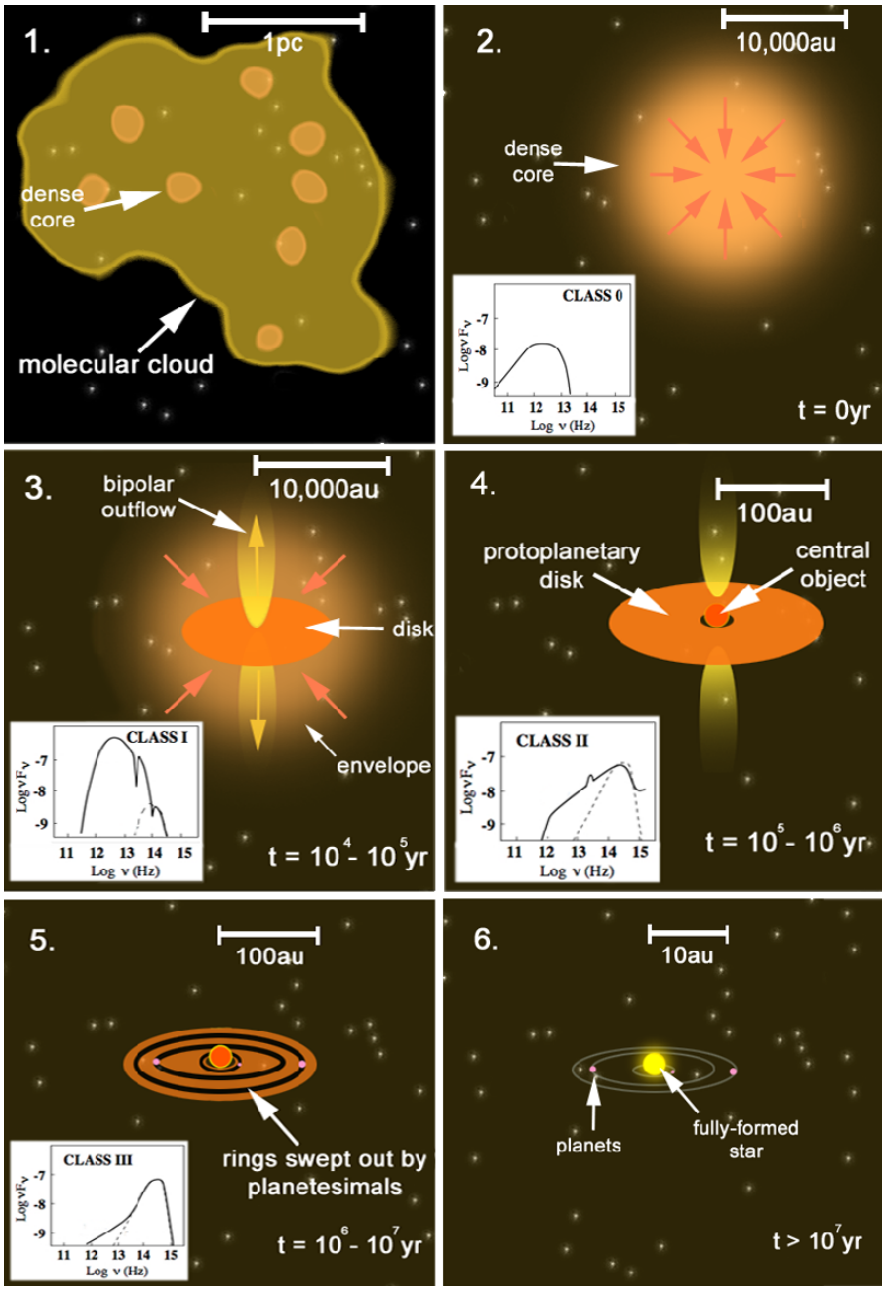

Figure 1.1: *Scheme of YSOs evolution(taken from PhD thesis of Frost A.J.,2020)*

1.3 Protoplanetary discs physics

The main actor in the formation of planets is surely the PPD. This section is dedicated to a description of the disc physics. As mentioned in the previous section the disc can dissipate angular momentum and this leads to accretion onto the star. This happens only if there are present turbulent processes. The viscosity ν plays an important role in describing the process of accretion. The description, given by the work of (Lynden-Bell and Pringle, 1974), is based on the idea that some infinitesimal particles bring the angular momentum toward orbits at infinite radius and in the meanwhile the remaining mass moves inward after transfering all the angular momentum to that particles. The result is that some parts of the disc are accreted by the star. The exchange of angular momentum can be explained only if there is a treatment of the process in which viscosity is present. The classical parametrization of the viscosity is due to the simple, but effective, simplification proposed by Shakura and Sunyaev, 1973. The viscosity ν depends on: a dimentionless parameter called α, a characteristic length and a turbulent velocity. Generally the characteristic length is assumed to be less than the height H of the disc and the turbulent viscosity is smaller than the sound speed c_s. According to these conditions the viscosity has this form: $\nu = \alpha H c_s$. The dimentionless parameter must be $\alpha \leq 1$ for the two stated limits. The equations that describe the dynamics of a viscous fluid are: the continuity equation and the Navier-Stokes equations. The PPD is assumed to be infinitesimal thin and axisymmetric. Under the first assumption the two equations can be written in cylindrical polar coordinates centered on the star. Considering the symmetry of the disc the continuity equation is written in the following way:

$$\frac{\partial \Sigma}{\partial t} + \frac{1}{R}\frac{\partial}{\partial R}(R\Sigma v_r) = 0 \tag{1.5}$$

where Σ is the surface density, R is the disc radius and v_r is the radial velocity. The Navier-Stokes equation is the general equation which describes the evolution of the surface density Σ in case of a Keplerian disc. This equation is derived by solving the momentum equation for a thin disc in which viscous forces are included. So the Navier-Stokes equation has the following expression:

$$\frac{\partial}{\partial t}(\Sigma \Omega R^2) + \frac{1}{R}\frac{\partial}{\partial R}(\Sigma v_r \Omega R^3) = \frac{1}{R}\frac{\partial}{\partial R}\left(\nu \Sigma R^3 \frac{d\Omega}{dr}\right) \tag{1.6}$$

where Ω is the orbital frequency. Combining the equations (1.5) and (1.6) and putting $\Omega = \sqrt{GM_*/R^3}$, where M_* is the mass of the star, the term with the radial velocity are eliminated. In this way is obtained the disc evolution equation

$$\frac{\partial \Sigma}{\partial t} = \frac{3}{R}\frac{\partial}{\partial R}\left[R^{\frac{1}{2}}\frac{\partial}{\partial R}(\nu \Sigma R^{\frac{1}{2}})\right] \tag{1.7}$$

this is a diffusive partial differential equation and it is generally non linear. Although this is non linear, it's possible to find some solutions. In particular if the viscosity ν is

not dependent on the surface density Σ. As demonstrated by (Lynden-Bell and Pringle, 1974) the simpler assumptions are to put the viscosity constant in time and independent on R and Σ. Under these assumptions, the solution of the equation (1.7) is called "*spreading ring*". The solution is derived considering an infinitesimal ring of mass m, whose shape is represented by a δ function centered at a generic radius R_1, that is:

$$\Sigma(R, t = 0) = \frac{m}{2\pi R_1}\delta(R - R_1) \tag{1.8}$$

The solution, taking care of these assumption, is the following:

$$\Sigma(x, \tau) = \frac{m}{2\pi R_1^2}\frac{x^{\frac{-1}{4}}}{\tau}e^{\frac{-(1+x^2)}{\tau}}I_{\frac{1}{4}}\left(\frac{2x}{\tau}\right) \tag{1.9}$$

where $I_{\frac{1}{4}}$ is a modified Bessel function, $x = R/R_1$, $\tau = 12\nu t/R_1 = t/t_\nu$. The viscous time scale is defined as:

$$t_\nu \sim \frac{R_1^2}{\nu} \tag{1.10}$$

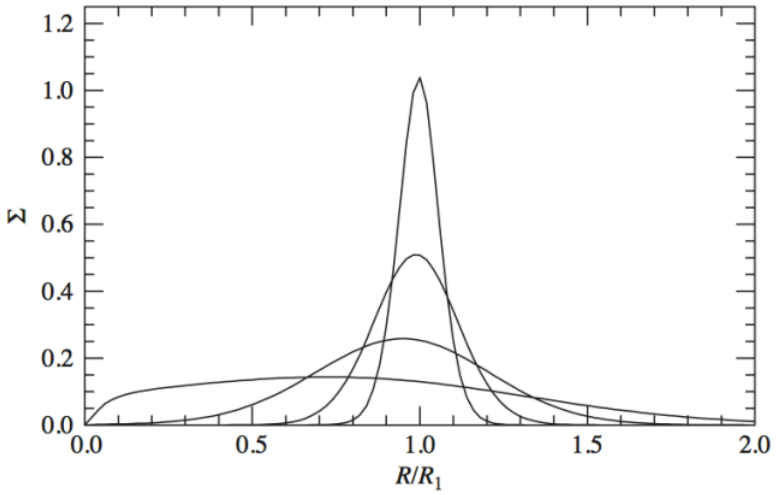

Figure 1.2: *Evolution of the surface density Σ for a "spreading ring" solution (taken from Hartmann et al., 2009).*

This solution describes what happens to a disc in which viscous forces are present. The angular momentum transfer is essential to explain the accretion. The viscosity permits to the various rings of the disc to transfer outward the angular momentum. The results is that the innermost rings cannot maintain the same position around the star and start to sink inward and so been accreted. The radius, at which the transition happens, is defined as $R_{tr} \sim R_1(t/t_\nu)$. As time passes the transfer of angular momentum outward is carried by a negligible mass to an infinite radius. This motion is described in Fig.[1.2].

1.4 Protoplanetary discs depletion

As discussed in section 1.2 the PPD evolves over time. In the section 1.3 the solutions explain how the accretion is originated. In reality the disc evolution is not only triggered by accretion. Now the treatment takes care of others factors which can play a decisive role on the evolution of a PPD. This section is dedicated to give an overview of these phenomena. The depletion of a disc is also caused by two main factors: photoevaporation and tidal encounters. The first phenomenon is divided in two cases: internal photoevaporation and external one. The external photoevopartion and tidal encounters are dependent on the environmental conditions in which the star is present. The first case is the one in which the environment does not impact on the star-disc system. The only actors that affect the disc depletion are accretion and internal photoevaporation. Once the star becomes visible, dissipating the envelope around it (class II YSO), the wind released by star impacts strongly on the disc. Photoevaporation effect is driven by the UV and/or X-ray radiation of the star. The radiation heats the gas present on the disc surface. The gas heated gets thermal energy and can escape from the potential well of the central star. This happens at those radii from the star where the potential energy can be easily exceeded by the thermal energy gained by the gas. The result of the process is the presence of an outflow in a form of a photoevaporative wind (Alexander et al., 2014). The equation, which expresses the evolution of the surface density for a viscous PPD, is more complex. In order to represent the effect of the internal photoevaporation the equation (1.7) becomes:

$$\frac{\partial \Sigma}{\partial t} = \frac{3}{R}\frac{\partial}{\partial R}\left[R^{\frac{1}{2}}\frac{\partial}{\partial R}(\nu \Sigma R^{\frac{1}{2}})\right] + \dot{\Sigma}_{wind}(R,t) \tag{1.11}$$

where $\dot{\Sigma}_{wind}$ is the mass loss therm, its form varies in base on the model which describes the photoevaporation (Alexander et al., 2014).

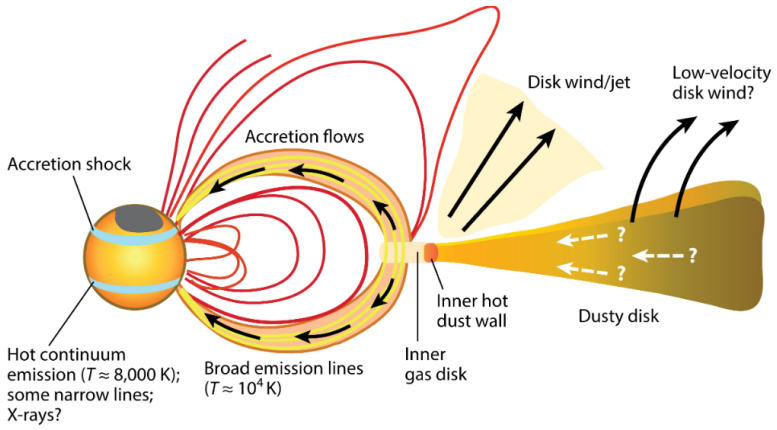

Figure 1.3: *Scheme of the accretion and effect of stellar wind on the disc (from Hartmann et al., 2016)*

As explained above, stars form inside the cores and clumps within GMCs. Stars do not form individually, but in clusters or in associations. So, stars share the initial stage of their evolution in a complex environment. The environment conditions can have a strong impact on the star-disc system. The phenomena taken into account are: the external photoevaporation and the tidal truncation. The first one is dependent on the presence of hot stars (O,B class stars) which emit a combination of far-ultraviolet (FUV) photons and extreme-ultraviolet (EUV) photons. As well as the internal photoevaporation what drives the depletion of the disc is the process of heating of the gas. The FUV and EUV fluxes of hot stars, combined with the weak gravity of the external parts of the disc, can have a very strong impact in reducing the disc dimensions in a vigorous outside-in depletion. The results of this phenomenon is observable: the outflows generated by the external photoevaporation give to the star-disc system a cometary morphology. This type of objects are commonly called "*proplyds*" as shown in the Fig.[1.4] below.

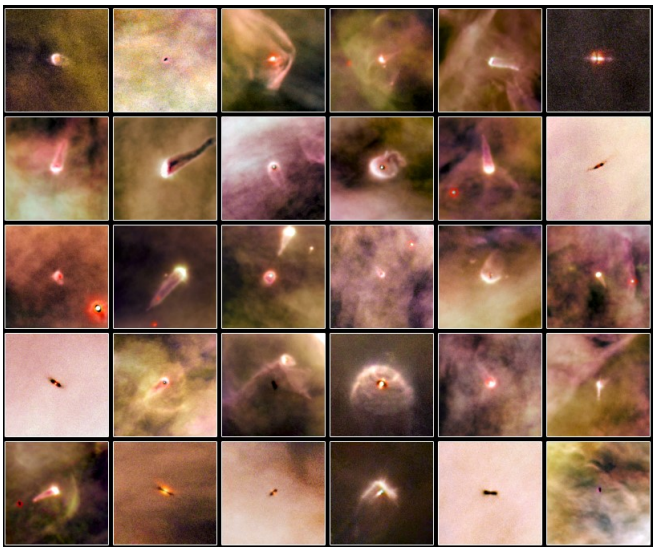

Figure 1.4: *Images of various proplyds in the Orin Nebula. The cometary shapes are produced by the action of strong stellar winds (taken from Ricci L. article in ESA website)*

The other actor in the depletion of PPDs is the tidal truncation. The crowding of the newly-formed clusters can cause the possibility of gravitational interaction between stars. Moreover, if the environment is too dense a PPD can undergo truncation and mass-loss due to close encounters. The main point is to understand what process plays a major role in the PPD destruction. An important work was made about this argument by Winter et al., 2018. In this paper the authors study the evolution of a PPD having a mass of $M_d = 0.1 M_\odot$ and the central star with $M_* = 1 M_\odot$. Firstly, some assumptions are set in order to reconstruct a stellar population with a initial mass function (IMF). In this way it's possible to identify the number of the hot star, which are the causes

of photoevaporation, and give a value to the FUV flux in therm of a parameter called G_0. The less numerous massive and hot stars dominate the external photoevaporation, because they are the main emitters of FUV photons. Another important quantity is the stellar density n_c. Having these two parameter it possible to set the environment features. A relation, which links these quantities, can be find. From the simulation made by (Winter et al., 2018) it is possible to have an example of this relation:

$$G_0 = 1000\left(\frac{n_c}{pc^{-3}}\right)^{\frac{1}{2}} \tag{1.12}$$

The effects on the disc are estimated trough its evolution in size. This evolution is determined looking at the variation of the outer radius of the disc R_{out}. The initial value of the outer radius is set as $R_{out} = 100au$. The effect of the tidal truncation is described with a probabilistic approach. The results show that the dimension of the disc does not vary so much. To prove the likeness of this conclusion these results are compared with the effects due to the phtoevaporation. From this comparison it's possible to state that in a classical lifetime of a PPD (3Myr) external photoevaporation is the main actor in the depletion of PPD and star-disc interaction is a secondary mechanism. The behavior of the disc depletion can be seen in Fig.[1.5].

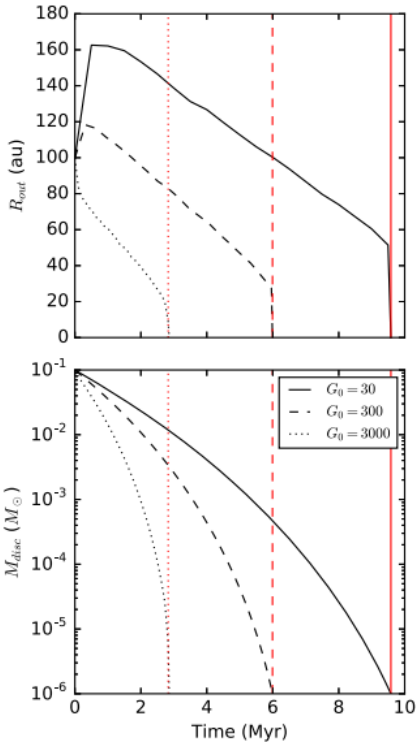

Figure 1.5: *Outer radius (top) and disc mass (bottom) evolution. The effect of photoevaporation is varying with the value of G_0. The bigger is G_0 the smaller is the disc dimension (from Winter et al., 2018)*

1.5 Role of the thesis

The disc dispersal plays an important role on planets formation since the depletion effects are present during the planet-forming epoch. As discussed until now the photoevaporation has the meanly effect on the PPD depletion. The removal of the gas from the disc increases the dust-to-gas ratio. This quantity is crucial on driving the collecting mechanism for the planetesimal formation and terrestrial planets formation is preferred to a gas-giant planets (Alexander et al., 2014). Also the dispersion of PPD has a dynamical effect on the planets orbits (e.g. migrations). So the architecture of a planetary system can be affected by photoevaporation. To understand this phenomenon is important to observe the mass-loss rate and this is possible trough spectroscopic observations. This thesis aims to find an effective method to extract stellar spectra. The procedure to do so is explained in the following chapters and it is not a simple task. The main difficulties are the background extraction and the sky subtraction. The importance of this work is due to study for the first time regions of our galaxy relatively far from us. This work is only a first step of a scientific research which aims to find the conditions of the formation of a planetary system that can support life. In fact, this work is also important to understand if our Solar System had some particular initial conditions which permitted its actual shape. Again, the environment in which a star born affects its PPD evolution and its planets formation.

Chapter 2

Data and instrument set-up

The effects of star-disc interaction and photoevaporation have an observational response. Their manifestation is in the form of outflows. The only way to study these processes is via spectroscopy. In this section a complete description of the data and instrument is given. The data are the same of (Itrich et al., 2023), so their description follows the same one of this paper.

2.1 Instrument description

All the information of an astrophysical object are carried by photons. Their detection is essential in order to make science. In astronomy there are two main ways to collect photons: photometry and spectroscopy. In this work both are used, but the main actor is spectroscopy. The astrophysical problem taken in consideration is studied by a spectra analysis of stars. A spectrum is created when the light passes trough a split or a prism and it is divided in all its wavelengths. Having a spectrum is the way to access to a lot of information. What characterize a spectrum are the lines. While studying the lines is possible to give a physical explanation of the processes which emit that photons. In this case spectra are obtained by an integral-field spectroscopy (IFS). This technique is known as 3D spectroscopy, because it creates a 3D data cube in which there are two spatial dimensions (X,Y) and one spectral dimension (λ). IFS has a lot of benefits over the classical spectroscopy methods. For example minimal slit losses, ease of removing the dispersion caused by atmospheric effects and no requirement for target acquisition. In recent time new instrumentation have been developed in order to improve IFS and the most famous one is the integral field unit (IFU). An IFU receives signal from the pixels in the field and produces a spectrum for each one. All the spectra created are stored in a data cube, where the spectral dimension is coming from the spectrograph. So finally the data cube is formed and it is composed by various "*spaxels*", which are pixels in which there is also the spectral information (Fig.[2.1]). An IFU can have two

types of configurations: an optical fiber array and an image-slicers method.

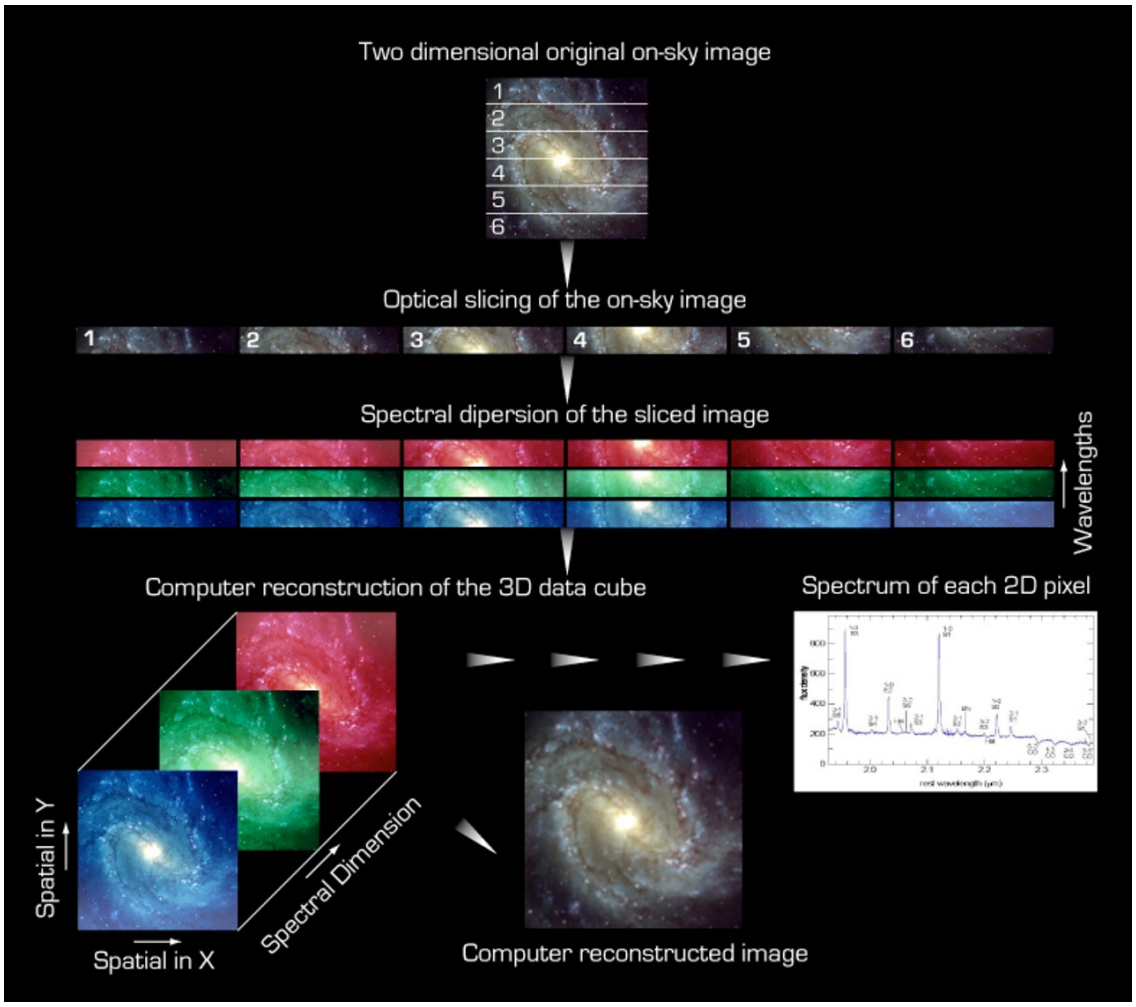

Figure 2.1: *Scheme of an integral field spectroscopy, taken from ESO.*

The data were acquired by the Multi Unit Spectroscopic Explorer (MUSE), shown in Fig.[2.2](Bacon et al., 2010). It is a second generation instrument mounted on the Nasmyth focus of UT4. UT4 is one of the telescopes of the Very Large Telescope (VLT). VLT is a facility of the European Southern Observatory (ESO), located in the Chilean region of Antofagasta. It has a large field of view (FOV) of $1' \times 1'$. Its observational spectral range is between 4500 and 9300Å. MUSE has 24 IFUs which of these is provided of a CCD. The spectral resolution is 2.6Å. The data are sampled per pixel is 1.25Å. A MUSE data cube can contain 10^4-10^5 spectra and it is composed by *spaxels*. Each layer of the cube corresponds to an image taken at that wavelength (Fig.[2.3]). MUSE can have three different modes: a wide field mode (WFM) with and without adaptive optics correction and a narrow field mode (NFM) with adaptive optics.

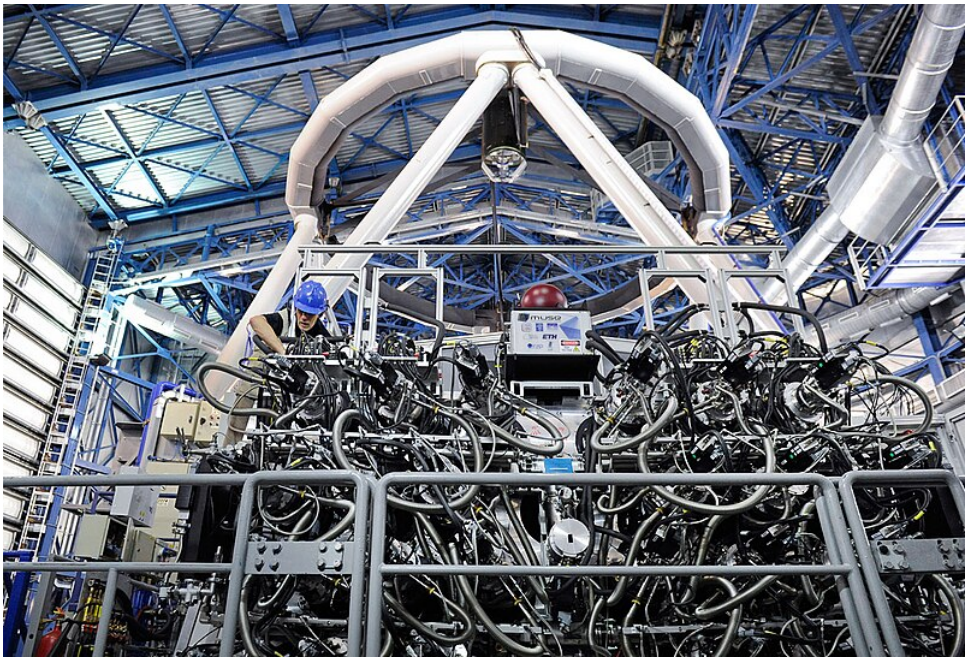

Figure 2.2: *A picture of MUSE installed on Nasmyth focus of UT4 at Very Large Telescope (VLT), credit: ESO.*

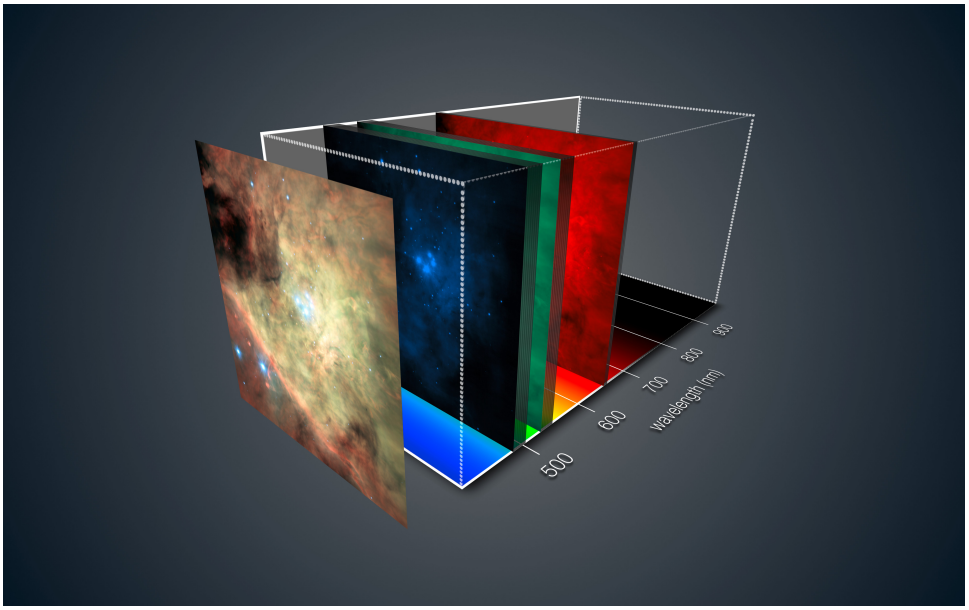

Figure 2.3: *A 3D data cube scheme in which there are two spatial dimension and a spectral dimension. Each slice is an image of that object in a precise wavelength. Taken from ESO.*

2.2 Description of the observed object

The observed object is the open cluster Trumpler 14 (Tr14), located in the Carina Nebular Cluster star forming region at a distance of 2.35kpc (Göppl and Preibisch, 2022). This cluster is the perfect candidate to study the dissipation of PPD due to external photoevaporation process, because it is one of the youngest stellar clusters in our galaxy with an intense radiation field. In fact, Tr14 hosts no less than 13 O class stars (Walborn et al., 2002). The presence of such massive, unevolved stars suggests a young age for the cluster ($< 10^6$ yr, Morrell et al., 1988; Penny et al., 1993; Massey et al., 2001). The young age of Tr14 is also confirmed by many works (Feinstein et al., 1973; Carraro et al., 2004; Vazquez et al., 1996; DeGioia-Eastwood et al., 2001; Tapia et al., 2003), in which the fitting of evolutionary tracks to optical and near-IR (NIR) photometric data estimates the age of this cluster. Morphologically, Tr14 is a centrally concentrated open cluster, roughly spherical in the optical and slightly elongated as traced by the NIR (Tapia et al., 2003) and X-rays observations(Townsley, 2006). In Fig.[2.4] a colour composite image of Trumpler 14 is shown (Ascenso et al., 2007).

Figure 2.4: *A colour composite image of Trumpler 14, taken from (Ascenso et al., 2007)*

It is important for the discussion to give also a description of the region in which Tr14 is located. As mentioned before the Carina star forming region hosts this cluster. In Fig.[2.5] there is a pretty panoramic of the huge nebula complex of the Carina. What is observable in visible band of a star forming region is the emission of the ionized gas. This gas is ionized by the radiation from the newly born stars. For this reason a star forming region, which experiences ionization, is commonly called "HII" region. This name derives from the fact that hydrogen atoms are fully ionized. The part of the nebula, in which Tr14 is located, presents ongoing star formation and so a strong emission from the ionized gas is present (Smith et al., 2008). Moreover also the Tr14 stars are the cause of such ionization. The emission of the nebula impacts inevitably the observations. This will be fully discuss in the following chapters.

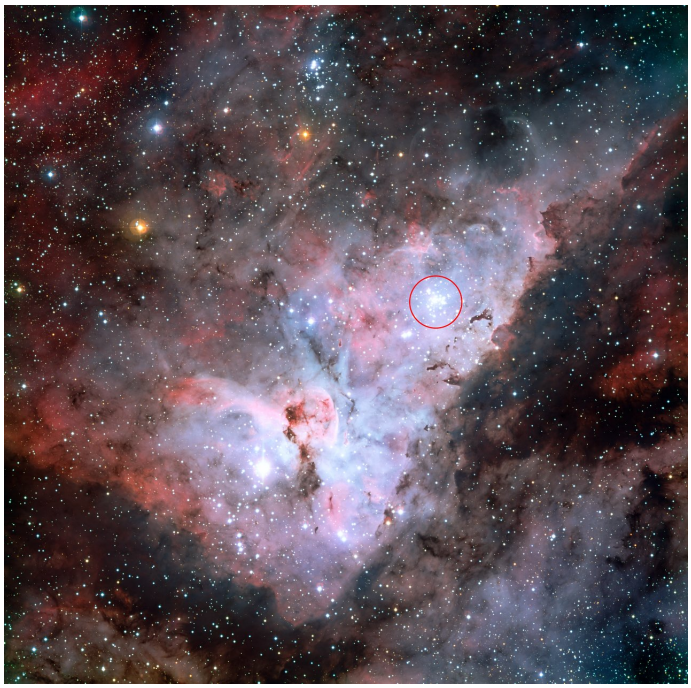

Figure 2.5: *Image of the Carina star forming region. Trumpler 14 position is marked with the red circle, credit: ESO.*

2.3 Observation description and data reduction

The observation was made in 2016 with MUSE. The data were acquired without adaptive optics using the Wide Field Mode (WFM) configuration of the instrument. The total field of view is $1' \times 1'$ and the spatial sampling is 0.2". Trumpler 14 and the nearby region were observed by 22 pointings. For each pointing the total integration time is 13min. The observation was made taking care to have spatial overlaps between pointings, in this

way it was possible to cover smoothly the observed area. Every pointing was observed three times with a 90° rotation of the dither pattern in order to remove the instrument artefacts. This work is centered on the study of only one pointing of this program, which is the pointing "6" (showed in Fig.[2.6]). Here are reported the details of this pointing. Due to the bad weather condition some observation were repeated, but this is not the case for pointing 6. The following table shows the observational log.

Pointing	Coordinates (h:m:s d:m:s)	Date	Seeing (")	Grade	Calibration standard
6	10:44:00.6-59:31:38.6	28.02.2016	0.90	B	GD71

Table 2.1: *Observational log. The seeing listed in the table is a mean value. The B grade means that the observation is mostly within constrains.*

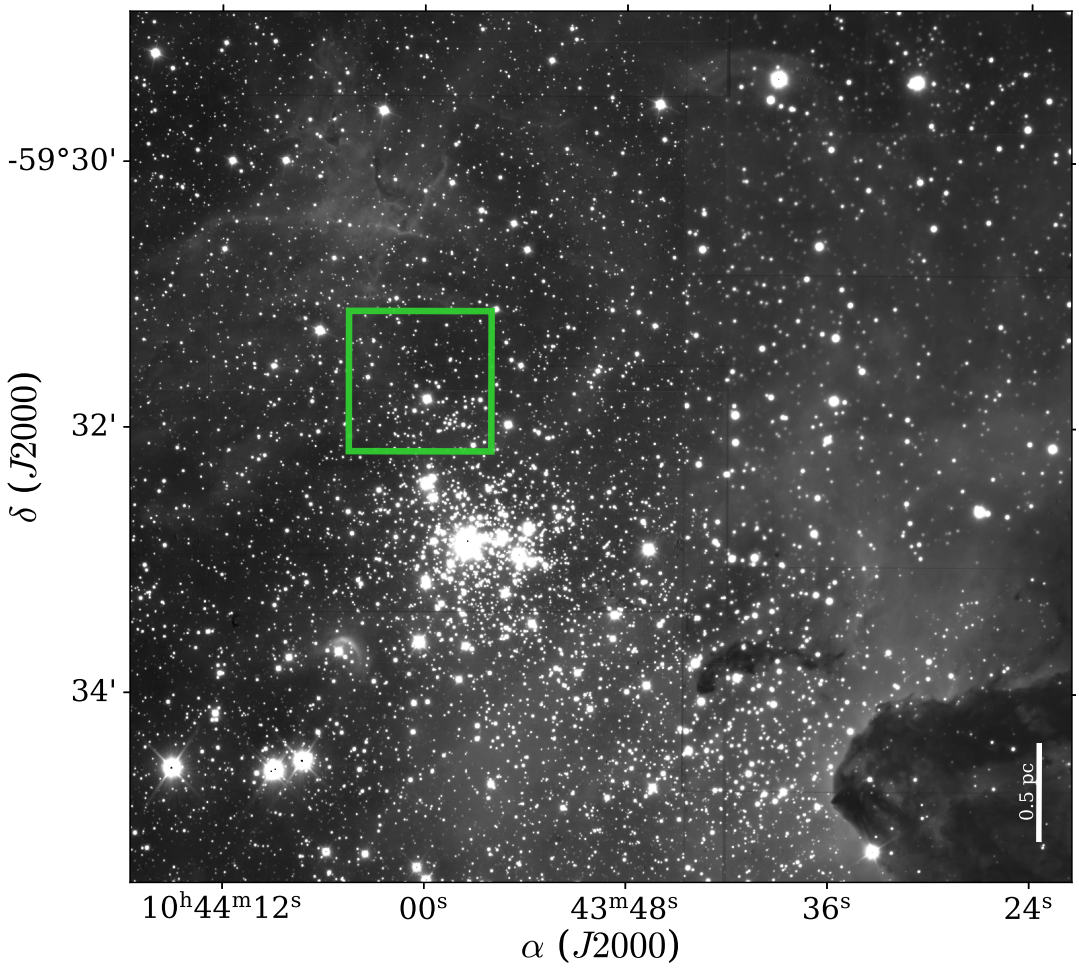

Figure 2.6: *Image of Tr14 in which pointing 6 is marked with a green square.*

Observation data were collected using the dedicated ESO pipeline built into EsoReflex v.2.8.3 (Weilbacher et al. 2020). This pipeline provides wavelength and flux calibrated IFU cubes. The calibrated exposures are combined into a 3D data cube. In addition to creating 3D data cubes, ESO's pipeline extracts photometric images in the standard Johnson-Cousins bands (Fig.[2.7]). These images are used as a guide to select sources for spectral extraction from the IFU cube.

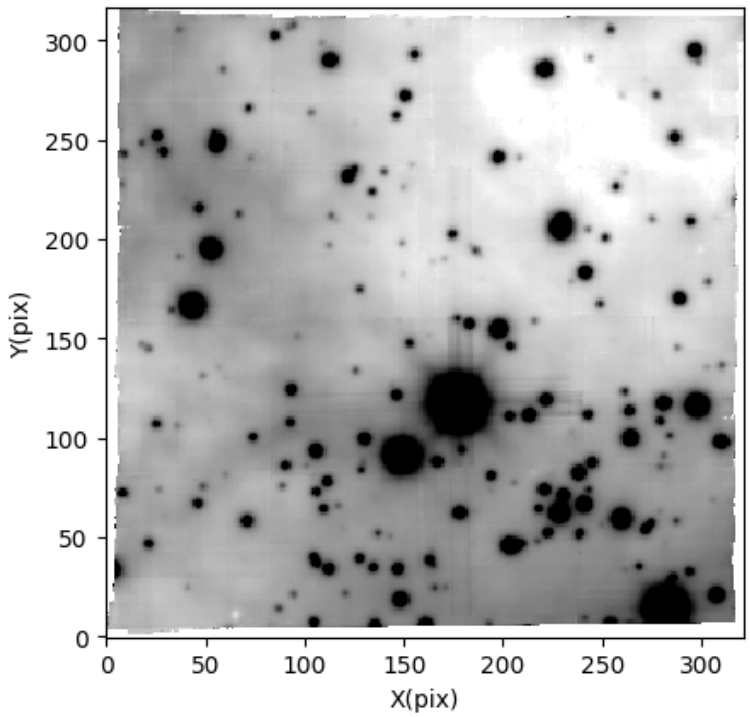

Figure 2.7: *Photometric images in the standard Johnson-Cousins bands (Filter I) of panel 6 computed from our MUSE spectral cube.*

MUSE coordinates were corrected using Gaia DR3 catalog (Gaia Collaboration et al. 2022). The corrections were estimated with the median differences in right ascension and declination between MUSE and Gaia. In order to have corrected coordinates the corrections must be added to the original MUSE coordinates. Regarding the pointing 6, the corrections are listed in the following table.

Pointing	$\Delta\alpha$ (")	$\Delta\delta$ (")
6	-5.75 ± 0.16	-0.59 ± 0.07

Table 2.2: *Coordinates corrections for pointing 6.*

After this correction, the new coordinates were matched with the Gaia ones. This task is made in order to refine the astrometric correction and estimate its accuracy. This was determine by defining the best matching radius which is the separation between the two catalogues. The best radius for this cross-matching was found to be 0.5".

2.4 Main data problem

As discussed in the section (2.2) Trumpler 14 is located in the Carina star forming region. This means that nebular emission is diffuse, strong and spatially variable. The observation is inevitably affected by strong sky emission. From the previous figure (Fig.[2.6]) it is possible to appreciate the diffuse background emission. It is also possible to see that sky emission is not equal over the field of view, but it is highly variable. The combination of high sky emission and its spatial variability are the main difficulties in extracting stellar spectra. These two features of the background bring uncertainties on the measurements. The main goal of this thesis is to find an effective method to extract stellar spectra and measure emission line fluxes. But to do so it is essential to quantify the behaviour of the background. Sky emission is described by its spectrum. As it will be discussed in the chapter 3, in addition to the extraction of the stellar spectra, the proper analysis require also extraction of the background spectrum. In the chapter 4 the discussion will consider the important role of the sky subtraction task in order to calculate the intensities of the spectral lines and so it is fundamental to take carefully the subtraction of the nebular emission. So this work aims to find a way to study the star spectra with the presence of this hostile background behaviour. This work is fundamental also because the future research will surely face this observational problems. In fact all of the YSOs are embedded inevitably in star forming region and their future observations will be affected by sky emission.

Chapter 3

Data analysis

In this chapter the procedure of the stellar spectra extraction is explained. Before starting to discuss about the series of steps of the data analysis, it is important to specify that there is not the need to calibrate the data. The MUSE pipeline not only creates data cubes, but also it calibrates them. The other product of the pipeline are the photometric images in several photometric filers (the images in I and V filters are used in this thesis), as reported in the previous chapter. This images are essential to start the analysis. In fact, the first step of the procedure is to find the positions of stars in the field.

3.1 Stars identification

The data analysis starts from the identification of stars positions. Identifying astronomical sources is an essential step in order to make photometry on that sources. This work uses the python Photutils package, which includes tasks designed specifically to detect point-like sources in an astronomical image, which means stars positions detection. In real astronomic observations stars do not appear as points. The instrument, during the observations, inevitably has a response that spreads the stars light over the detector. The point spread function (PSF) is the true instrument response for stellar sources. In addition to the instrument response, atmospheric seeing degrades the stellar image even further. The real PSF is a combination of the two and in the optical is generally dominated by the the atmospheric seeing. A widely-used tool in astronomy is DAOFIND algorithm (Stetson et al., 1987). In this work the used tool is `DAOStarFinder`, which is a class that provides an implementation of the DAOFIND algorithm with photutils. This tool essentially uses a function to identify peaks of stars PSFs in an image that are above a specified threshold value. This is not a single step task, but some passages must be followed. Firstly, stars' PSFs must be represented by a distribution, which means searching the best representation of the PSFs shapes. In our seeing dominated case PSFs are described by a Gaussian distribution. The input parameters, passed to

`DAOStarFinder`, in order to shape the distribution, are the following: `fwhm`=4.5 full-width half-maximum (FWHM) of the major axis of the Gaussian kernel in units of pixels and `sigma radius`=2 truncation radius of the Gaussian kernel in units of sigma (standard deviation of the Gaussian). The second step is to search the peak of the Gaussian distributions in the image and so find the so-called *centroids* of all stars. To find a *centroid* is important to pass a threshold parameter to `DAOStarFinder`. The threshold is used as a limit value in order to select those sources with a peak value above this limit, in this case `threshold`=1· sigma. Finally, after the program finds the sources, all the *centroids* are saved into two arrays (one per filter). The X and Y coordinates are assigned to each star and these coordinates are expressed in pixels unit. In the following figure (Fig.[3.1]) the photometric images with marked stars *centroids* are shown.

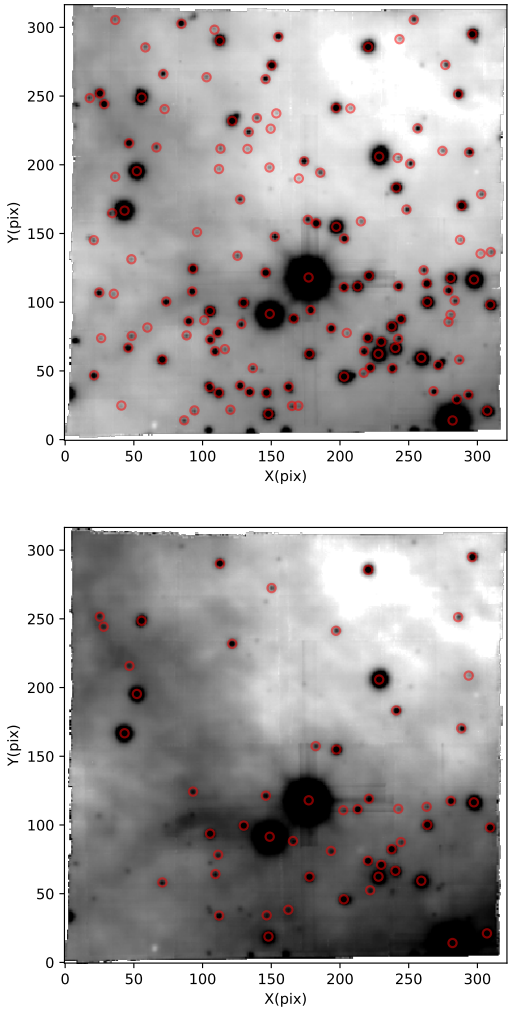

Figure 3.1: *Photometric images of pointing 6 in filter I (top) and filter V (bottom). The stars centroids are marked with red cirlces*

Looking at the previous figure (Fig.[3.1]) it is possible to see that in the filter V image there are less detected sources than the filer I one. This is caused by the presence of the nebular emission which mostly affects the V band and makes it difficult to identify the peaks of stars PSFs. In addition, interstellar extinction also has a larger effect at shorter wavelengths, limiting the number of stars that can be detected in V. For the subsequent analysis, we decided to use the stellar positions identified in the I-band, after having checked that the I-band *centroids* agree with the V-band ones, for the stars detected in both bands.

3.2 Aperture correction

The second step of the data analysis is to calculate the aperture correction (AC). It is an important part of the photometry procedure, because it allows us to compute the corrected magnitude values. Magnitudes are the products of the aperture photometry (AP). AP consists in making the sum of the pixels counts within a circular aperture centered on the centroids of the sources. Then this resulting sum must be subtracted by the product between the nearby median value of the sky counts per pixels and the number of pixels contained inside the aperture. AP equation has the following expression:

$$Mag = -2.5 \cdot \log_{10}(C - A \cdot S) + 25 \tag{3.1}$$

where C represents the counts inside the aperture of the source, A is the area of the source aperture and it is dependent on the aperture radius, and S is the values of the nearby median value of the sky counts per pixels. For clarity C contains not only the counts referred to the source but also the counts of the background inside the aperture. To have a good magnitude measure all the flux from the star is needed. In order to have good magnitudes values it is necessary to choose an aperture as large as possible. But this can be done only if there are very isolated sources and this is not the case of this work. The studied field of view presents star crowding and so it is important to choose apertures taking care of this situation. It is then necessary to reduce the apertures size. In a fixed aperture only a fraction of the flux is received, this fraction is dependent on the PSF and on the aperture radius. Reducing the source aperture area means having inevitably information losses. In order to fix this, AC can correct the photometric calculations. Essentially, AC is the difference between two magnitudes calculated for two different aperture radii. And so it is possible to express AC in this way:

$$AC = Mag(r_1) - Mag(r_2) \tag{3.2}$$

where the magnitudes are calculated with the equation (3.1). In this work the evaluation of AC is a very important step and it is done following some specific decisions. Firstly, some stars are selected in order to calculate the AC. They must be sufficiently bright,

but not saturated, and isolated. As reported above it is not possible to find completely isolated sources, in fact it may be difficult to find stars with perfect characteristics. This is not a problem, because the AC can be estimated also with a limited sample of stars. However it is important to select stars in different positions across the field, in order to avoid a representation of only one part of the image. In the following figure (Fig.[3.2]) the selected stars are shown.

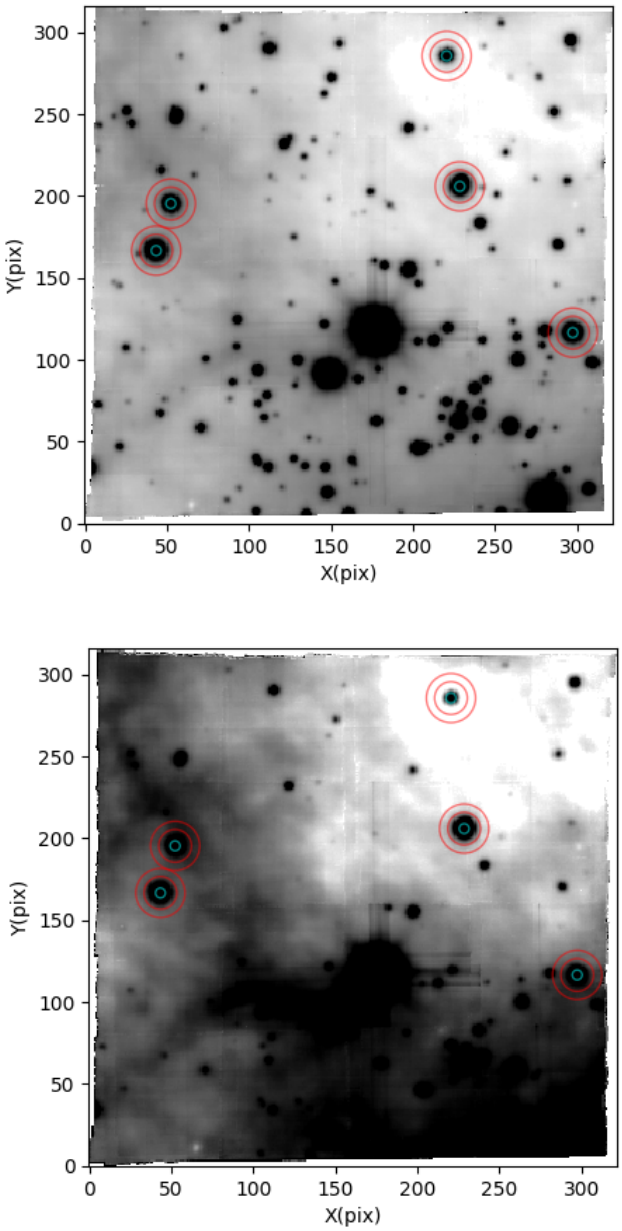

Figure 3.2: *Selected sources for the AC calculation in filter I (top) and filter V (bottom). Cyan circles are the sources apertures (3 pix radius) and red circles are the sky annulus (10 and 15 pix radii).*

In order to verify if a star presents saturation the curve of growth needs to be checked. This verification is done making photometry for different apertures, in this way a magnitude-aperture radius relation is found. The name "curve of growth" is referred to the behaviour of the magnitude evaluation calculated for increasing aperture radii. In Fig.[3.2] the five curves of growth for the respective stars are shown. It is possible to see the shape of the curves: initially magnitudes start to grow as the radius is growing, but at a certain radius the magnitude growth stops and this means that the light emitted by the star is almost fully contained within the radius in which the "magnitude plateau" begins. This is the classical behaviour of a curve of growth of a bright, isolated and not saturated source. Again the chosen stars are selected on base of: their position in the field and their curves of growth behaviours. After proving the goodness of these five sources, the next step to calculate AC is to choose two apertures in which to estimate the magnitudes. This important choice is done looking again at the curves of growth. It is possible to see that at 10 pixels radius the magnitude does not change anymore, and so it can be affirmed that the whole light from the source is completely included within an aperture of 10 pixels radius wide. This is the first radius chosen for the calculation of the AC. The other radius is set equal to 3 pixels (cyan circles in Fig.[3.2]). This aperture radius is also used to make photometry on the entire stellar sample (see next section). This specific radius choice is made according to a trade off. The chosen aperture must be sufficiently wide in order to collect a reasonable fraction of the stellar flux and at the same time it must be small to reduce the effect of the background. To give a quantitative motivation of this choice, a condition is set: the aperture must contain a percentage of counts between [60%-70%]. This percentage is calculated dividing the number of counts within 3 pixels wide aperture and the number of counts within the 10 pixels wide aperture.

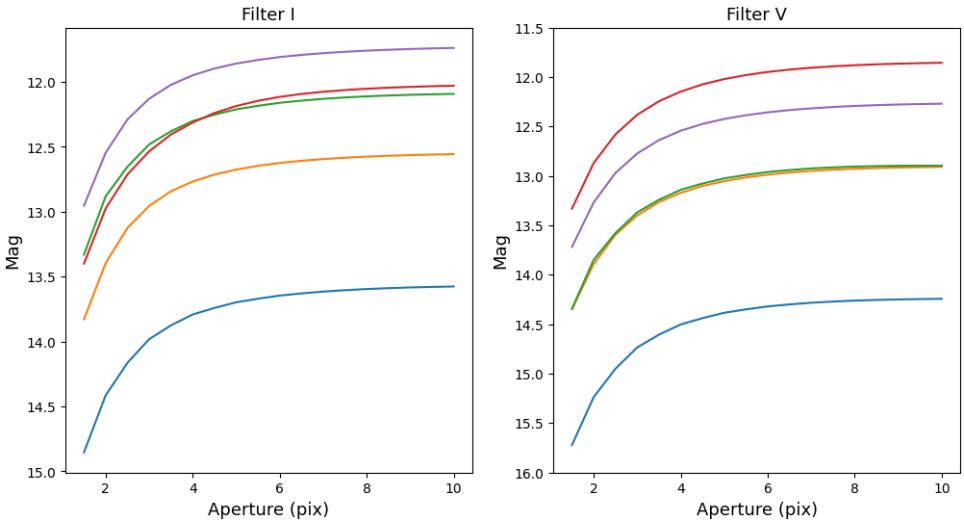

Figure 3.3: *Curves of growth of the selected sources in the two filters.*

To compute the magnitude of the stars it is also needed to set the sky annulus. As it is noticeable from equation (3.1), magnitudes are also depended from the sky counts. In photometry a sky annulus is important to have a measurement of the background emission. The annulus apertures must be chosen following a dedicate reasoning. The sky counts contained in an annulus must be representative of the sky emission inside the source aperture. This is essential in order to subtract the right background value. The sky annulus must be sufficiently near to the source, but not so close to include star PSF wings. Moreover, to get a more precise sky emission evaluation, a wide annulus is needed. In a case of isolated stars the annulus choice is not a problematic task. In this case the observation is affected by stellar crowding and furthermore the background is strongly variable. Sky annulus apertures are set by a compromise. In the figure below (Fig.[3.4]) three sky spectra obtained from different apertures are shown. The blue spectrum is extracted from an annulus with radii of 7 and 12 pixels. The blue spectrum has a higher count value than the others. It can be explained by the fact that the annuls is too close to the star and it includes a part of the star light. Instead, the green spectrum has the lowest count than the others, because it is far from the source. As discussed above, a sky annulus too distant from the source is not convenient, because it could contain flux from other stars and it could not be representative of the sky at the star position because of the high sky variability. The orange spectrum is the compromise. An annulus having 10 and 15 pixels aperture radii is chosen for the AC calculation. The annulus taken in consideration is shown with red circles in the Fig.[3.2]. This annulus could contain some sources, to avoid their contribution sky spectrum is extracted using the median counts values.

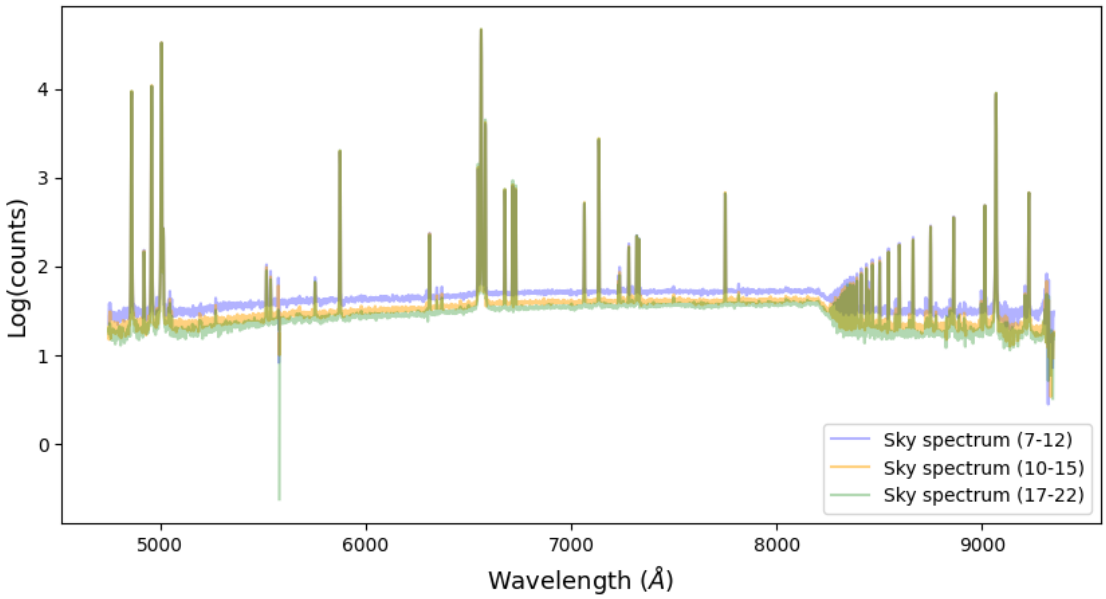

Figure 3.4: *Sky spectra fro different annulus apertures*

Set the apertures and motivated the choices, now it is fundamental to introduce a very important dependence of the AC. The calculation of the AC must be done for all the cube slices, which means evaluating it for different wavelengths. A dependence on wavelength is present and it is shown in Fig.[3.5]. AC is not constant with wavelength because PSFs are dependent on wavelength. This happens because the stars PSFs are not the same for different wavelength. In order to find the correct magnitude values is fundamental to find the value of the correction for each cube. This task is made calculating the median value of the AC of the selected stars sample for each slice. What is produced is an "AC spectrum" shown in blue in Fig.[3.5]. This spectrum has some significant noise and it cannot be used directly to find a proper value of the AC as a function of the wavelength. Finding a relation, from which useful AC values are evaluated, is not a simple procedure. Firstly, wavelength binning of the spectrum is done. For each bin the median value of the small set of ACs is calculated and these values are represented as red dots in Fig.[3.5]. After this for each median value a corresponding standard deviation is calculated. Finally, a best fit of the red dots is done and it is shown as a purple line in Fig.[3.5]. To do the best fit of those points a polynomial function of the fifth order is used. This line is the relation between AC and wavelength. Having all the AC values for each wavelength means to be able to find the corrected magnitudes value, and so fluxes, for all the slices. The result is the extraction of a corrected spectrum of each star. In the next section this procedure is explained.

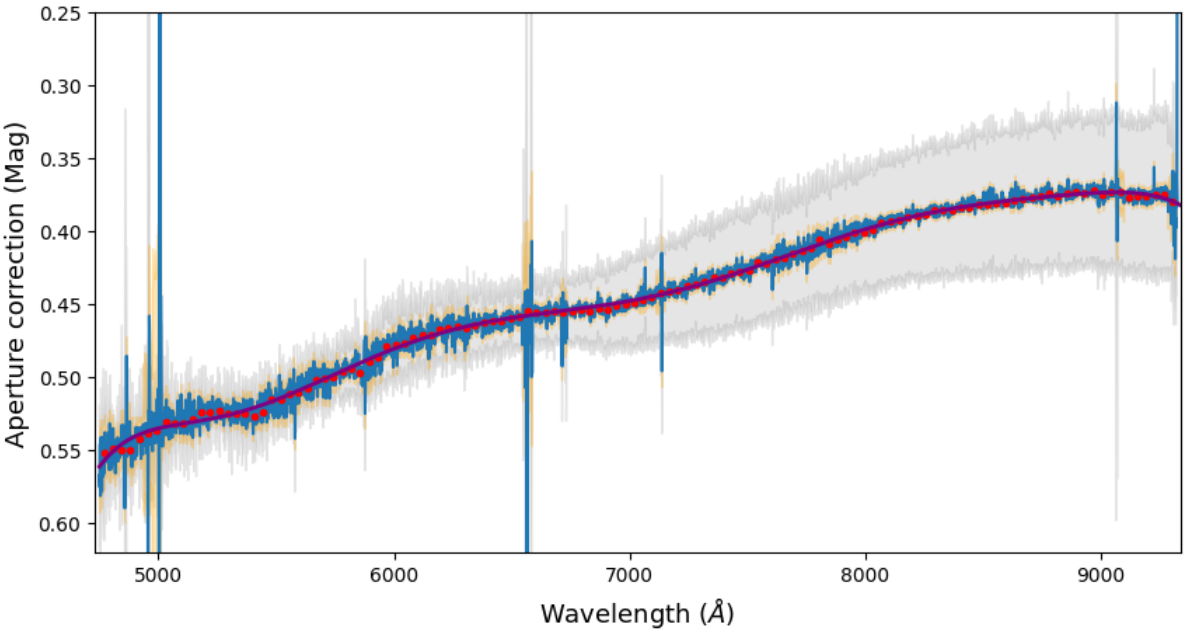

Figure 3.5: *Aperture correction dependence on wavelength.*

3.3 Spectra extraction

This section describes the procedure to extract all stars spectra. Essentially it is needed to do photometry of all stars for each of the cube slices. As reported in the previous section, the central aperture is fixed to 3 pixels radius and sky annuls is set between 10 and 15 pixels radii. These apertures decision is now extended to all the sources. If magnitudes (or fluxes) are computed using this procedure, not all the fluxes from the stars would be accounted for, resulting in a bias (function of wavelength) in the extracted spectra. To avoid such bias the AC is needed. The way to correct stars spectra is to subtract the AC. But it is well known that AC is not constant. In fact in the previous section a relation between AC and wavelength was found. So, it is essential to subtract the proper AC value. The AC-wavelength relation has these information. The formula to compute corrected magnitude is the following:

$$Mag_{corrected}(\lambda) = Mag(\lambda) - AC(\lambda) \tag{3.3}$$

where *Mag* is referred to the so-called "raw spectra" in the sense that they are not corrected. Having the corrected value of magnitude it is possible to construct the final products of this data analysis which are the final stellar spectra. The other important final results of the data analysis is the extraction of background spectra. The next chapter is focused on the study of these spectra. This work is not centered only to spectra extraction but also it has the goal to study the PPD depletion and its observational response is via spectral lines. So it is important to prove the goodness of spectra extraction operation. This will be proved by the comparison with spectra from literature.

Chapter 4

Results

This chapter focuses on the discussion of the work results. The final products of the data analysis are the corrected stars spectra. Firstly, I will discuss the performance of my methodology for the extraction of the stellar spectra. This will be described in the section (4.1) by the comparison of my spectra with the literature ones (i.e. spectra of Itrich et al., 2023). The other important role of the thesis is to study the external photoevaporation effect. Its observational response are spectral lines and they are contained within stars spectra. Having improved spectra means get access to the information carried by lines. The lines taken in consideration in this thesis are described in the section (4.2). In order to prove the lines detection is important to give a quantitative analysis of them and it will be fully explained in the section (4.3). We developed also a method to assess how much the measured line emission is affected by the subtraction of the sky emission.

4.1 Spectra comparison

The results of the data analysis are the stars corrected spectra. For the discussion it is fundamental to prove the goodness of these spectra. It is done with the comparison of these extracted spectra with the spectra in literature. Now, it is important to specify that the terminology "spectra literature" is referred to the work carried by (Itrich et al., 2023). The comparison between spectra is shown in Fig.[4.1]. In particular, the green spectrum is referred to a star of this work catalogue and the blue one is the respective spectrum of the aforementioned paper. The green spectrum is higher than the blue one. This means that the flux of the green spectrum is greater than the flux of the blue spectrum. The difference between the two spectra is due to the fact that in the Itrich work the spectra are extraction without the aperture correction. So blue spectrum is affected by information loss, instead the green one is corrected. From this explanation it is clear that AC is essential to extract spectra in an accurate way. Essentially, improvement is coming from the extraction procedure. The AC is the first one, because it's crucial to

correct the information losses.

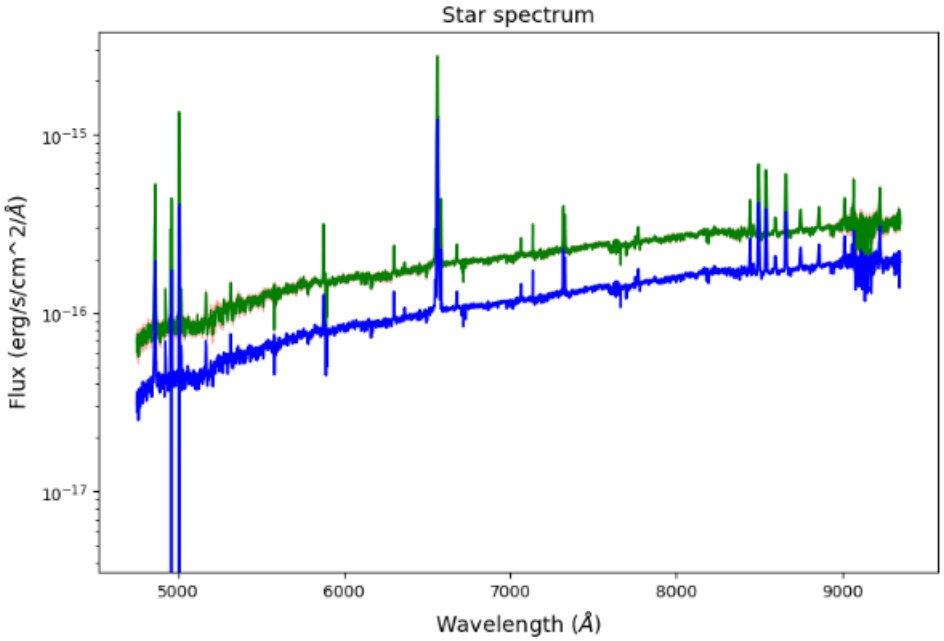

Figure 4.1: *Comparison between literature spectrum (in blue) and extracted spectrum in green. The red area around green spectrum is the propagation of the median RMS of the continuum.*

Another useful comparison is to confront not corrected ("raw") spectra, which means spectra in which AC is not applied. In figure 4.2 this comparison is shown, as before the literature spectrum is in blue. As it can be seen, the green spectrum is still above the blue one. It is not obvious this behaviour, because the aperture used in photometric task is smaller than the aperture used in the paper and so it is expected that the green spectrum is below the blue one. The explanation of the plot in Fig.[4.2] is given looking at the background spectra comparison (Fig.[4.3]). The extracted background spectrum is slightly below the one of the literature (Fig.[4.3] in blue). This has directly an impact on the extraction of the spectrum in the source aperture. The Itrich et al. sky emission is estimated using "sextractor" by constructing a sky image for the entire field of view of the MUSE observations. On the contrary, we estimated the sky in annuli close to each star. This explain why the green spectrum of figure 4.2 is above the blue one. It is important to highlight the fact that a better sky background is computed with our procedure. This is an important point of this thesis, because one of the main goals was to find a method to correct as much as possible for the sky background. After all these comparisons it is necessary to prove the effective utility of these extracted spectra, and this is done extracting the emission lines. In the next sections the discussion is centered on this analysis.

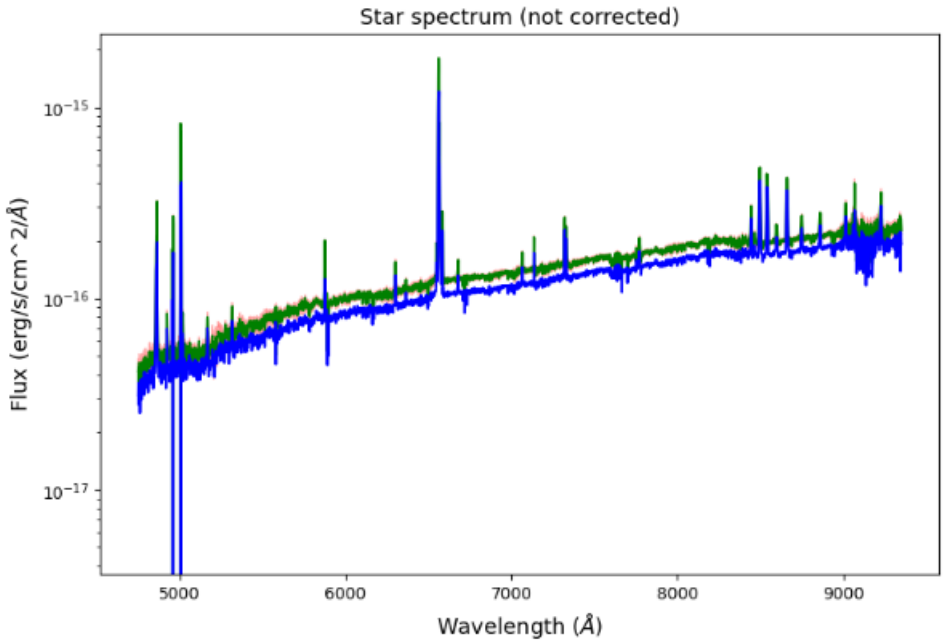

Figure 4.2: *Comparison between literature raw spectrum in blue and raw spectrum of this work in green. The red area around green spectrum is the propagation of the median RMS of the continuum.*

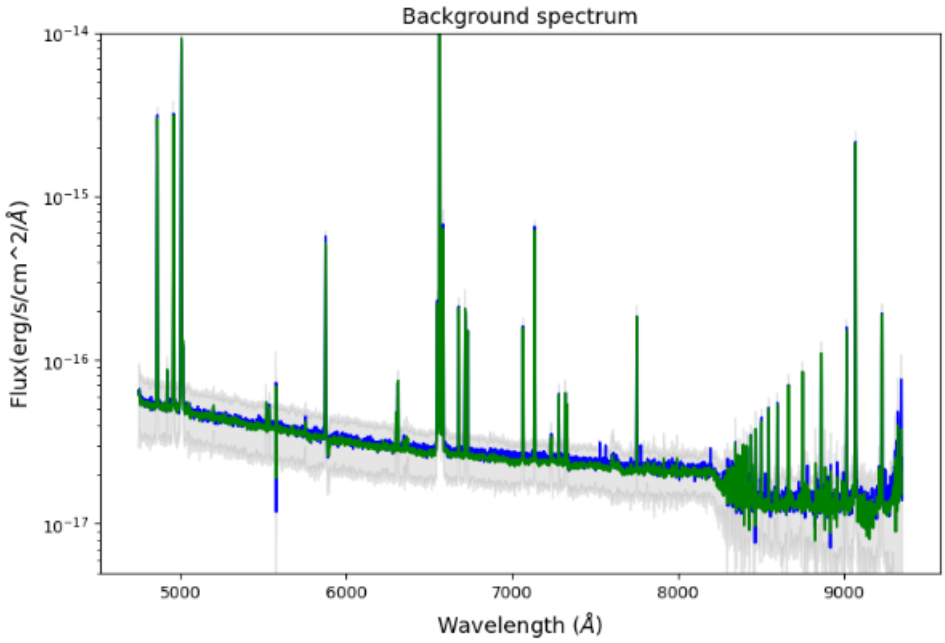

Figure 4.3: *Comparison between background spectra. Literature spectrum is in blue and spectrum of this work is in green. The grey area around the green spectrum is the sky noise propagation.*

4.2 Spectral lines

The other goal of this work is to derive accurate measurements of the emission lines in the spectra. These lines carry a lot of information about the process of the disc dissipation. As fully discussed in the first chapter the main two processes of discs dispersal are: accretion and photoevaporation. In particular, this work is centered on the external photoevaporation process. The observantional response of this phenomena are spectral lines. The study of the discs evolution is linked to the study of spectral lines. In table 4.1 a list of spectral lines is shown. For the spectral analysis some lines have been chosen. In order to prove again the goodness of the method of spectra extraction it is fundamental starting a discussion about the lines detection and their studying. The next section is dedicated to this analysis. It is important to specify that the aim of the thesis is not explaining the radiation processes which generate those lines.

Emission line	Wavelength ($\AA$)	Tracer of
Hα	6563	Accretion
Hβ	4861	Accretion
[OI]	6300	Photoevaporation
OI	8446	Photoevaporation/Accretion
HeI	5876	Accretion
HeI	6678	Accretion
HeI	7065	Accretion
HeI	7281	Accretion
[NII]	6548	Photoevaporation
[NII]	6583	Photoevaporation

Table 4.1: *List of the emission lines studied in this work*

4.3 Integrated flux

This section is dedicated to the evaluation of the integrated flux. This task is done for the emission lines listed in the table 4.1. Doing this calculation is fundamental to prove that selected lines are effectively detected and so it is possible to get information from them, useful to study PPDs depletion. The integrated flux F is defined as the integral of the flux subtracted by the continuum (f) over a wavelength range (λ_1,λ_2), in which the line is contained. This integral has the following expression:

$$F = \int_{\lambda_1}^{\lambda_2} f \cdot d\lambda \tag{4.1}$$

In a real case to calculate F, the integration can not be used, because the flux f is not a continuum function of the wavelength. For this reason the integral is replaced with a sum and the equation 4.1 is written as:

$$F = \Sigma_i f_i \cdot \Delta\lambda \tag{4.2}$$

where f is a discrete function of the wavelength and $\Delta\lambda$=1.25$\mathring{A}$. In practice, the sum of all the elements of the flux f within the wavelength range are summed and then this sum is multiply by $\Delta\lambda$. The $\Delta\lambda$=1.25$\mathring{A}$ is produced by the instrument resolution element (see section 2.1). The error associated to the integrated flux is given by applying the error propagation theory. The following equation represents the F error:

$$\Delta F = \Sigma_i \sigma_i \Delta\lambda \tag{4.3}$$

where σ_i is the error of f_i. After this introduction about the used formula, it is fundamental to explain how the process of the flux integration is done in this work. The formula used in this work for the integrated flux evaluation is the equation 4.2. The first important step is to determine the continuum value in order to subtract it from the flux of the spectrum. To explain this passage it is useful looking at the figure 4.4 (left panel) in which the line plotted is the oxygen forbidden emission line at 6300$\mathring{A}$. It is important to clarify that the evaluation procedure of the continuum is the same for all the line and this oxygen line is just an example, the other emission lines are shown in the dedicated appendix A. To determine the continuum a portion of spectrum is chosen around the considered line. This portion of the spectrum is 200$\mathring{A}$ wide. The continuum is calculated as the median value of the flux within this portion of spectrum. As it is clear the continuum has a constant value and it is shown as a cyan horizontal line in Fig.[4.4] on the left panel (and also in the appendix A plots). The other step in the F calculation is to find the extremes of the sum, i.e. the two wavelength which contain the emission line. These extremes are shown as two vertical red dashed lines. The choice of the extremes is made looking at the shape of emission line, in fact it is needed to choose the extremes as near as possible to the line to minimize the noise. After these two steps it is possible to find the integrated flux values of each line.
The integration task gives the possibility to distinguish with some condition: the detection of the line and the "good" measurements of F. In order to discuss about line detection and integration results, it is essential focus the treatment on the error associated to F. In reality two errors are calculated in this work and they are both useful. Looking at the formula shown in the equation 4.3 the only thing that could change is σ_i, that is the error on the subtracted flux by the continuum. Therefore, f_i has two error sources coming from: the error of the source spectrum and the error of the background spectrum. The first one is calculated as the median of root main square (RMS) of the star spectrum, the RMS propagation over the spectrum is shown in figure 4.4 (left panel) as a red area. The second error is referred to the sky noise which is the standard deviation

of the background spectrum computed in each spectral point separately, its propagation is shown as a light green area in the left panel and as a grey area in the right panel of Fig.[4.4]. The values of the noise computed in each spectral point for the sky are as a function of the intensity of the sky and its variability with the annuli. After finding these two different sets of σ_i values it is simple to derive the two errors of the integrated flux ΔF. For clarity a notation is used: ΔF_{RMS} indicates the error calculated with the RMS of the source spectrum and ΔF_{sky} is the one coming from the sky spectrum. To distinguish if in a given star a line is detected or not a double condition is set:

$$F > 3 \cdot \Delta F_{RMS}; f(peak) > 3 \cdot RMS_{median}(peak) \tag{4.4}$$

where $f(peak)$ is the value of the subtracted spectrum at the peak of the line and $RMS_{median}(peak)$ is the median value of the RMS at the peak of the line. If these two condition are both satisfied it is possible to affirm that the line is detected. Two examples of detected line are shown in the left panels of the figure 4.4 and 4.5. Instead a not detected line is shown in the left panel of figure 4.6. The failure detection of a line means that for that line the integrated flux is considered as an upper limit. This is the first possible result of the integration. Table 4.2 shows the results of the first ten stars of the catalogue for the forbidden line at $6300\mathring{A}$ (the entire table is in appendix B), in this table a column is dedicated to those upper limits and with "True" is indicated their presence (tables of the other lines are in appendix B). The other two results of the integration are distinguished in base on ΔF_{sky}. If $F > 2 \cdot \Delta F_{sky}$ this result is considered as a good result, meaning that the uncertainty in the integrated line flux, introduced by the background subtraction, is relatively small and an example is the figure 4.4. Instead if $F < 2 \cdot \Delta F_{sky}$ the resulting integrated flux is not an acceptable value. Looking at the left panel following figures 4.4, 4.5 and 4.6 it is possible to explain why these F results come out. The so-called "acceptable" result is due to the low sky noise which impacts slightly on the spectrum and so it permits to measure very well the line and calculate the integrated flux. In the left panel of figure 4.4 the light green area, which represents the sky noise, is not large and this explain visually the low impact of the background. Moreover the low contribution of the sky is appreciable from the different order of magnitude of the scales of the plots, in fact in the right panel the background spectrum presents a lower emission than the star or inversely the star emission is stronger than the sky one and so the star light is distinguishable. Instead, in the left panel of Fig.[4.5] the line is detected, but it is not possible to derive an accurate value of the F. This is explain also visually, looking again at the green area. The scales of the plots are equal in this case and so the sky emission contributes in the uncertain of the measure. The sky noise is large and it has a large impact on the star-disc emission. Finally, the upper limit is attributed to those stars for which no line has been observed, Fig.[4.6] shows clearly the absence of the line. In this case the order of magnitude of the sky background is lower than the source one. The absence of a result is not explained by the high sky emission, but the reason simply comes from the fact that no line is present.

This discussed procedure is applied to all chosen line. For brevity only the lines of the star with ID=4 are shown in appendix A.

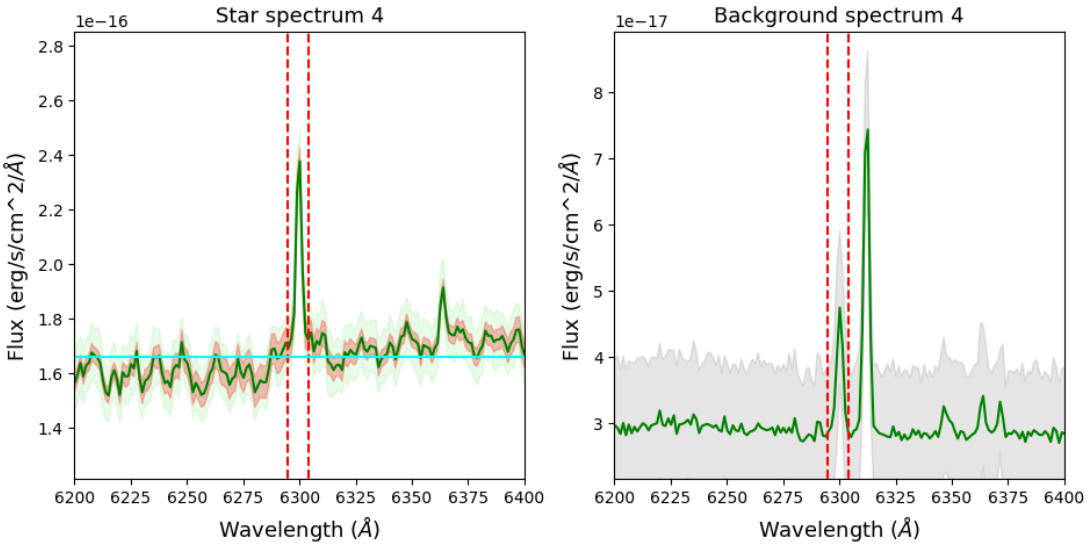

Figure 4.4: *Oxygen line at 6300Å of star 4. Left panel: spectrum is the green line, cyan line is the continuum, red vertical line are the integration extremes, red area is the RMS and light green area is the sky noise. The right panel shows the sky spectrum in green and the grey area is the sky noise.*

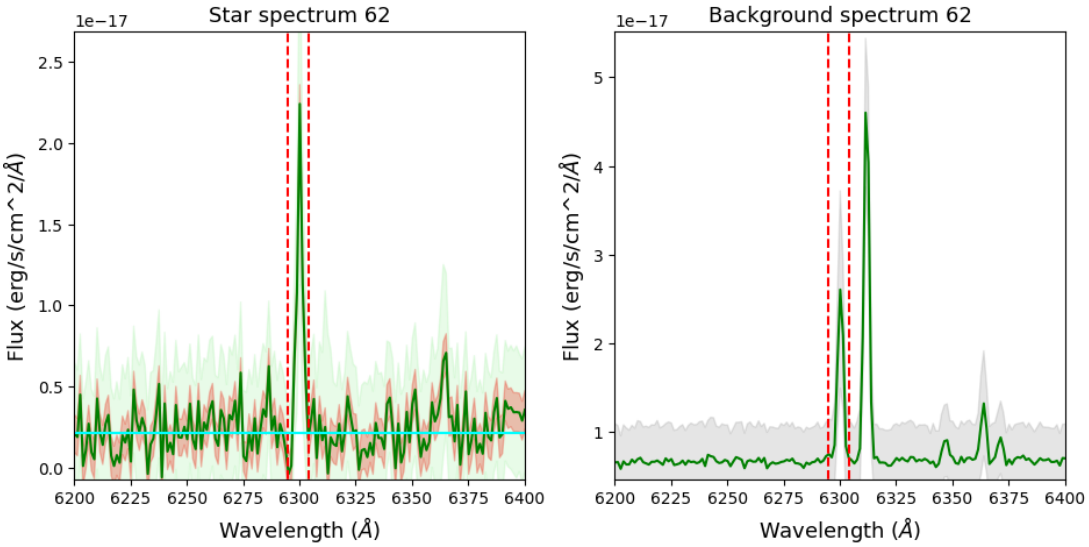

Figure 4.5: *Oxygen line at 6300Å of star 62. Left panel: spectrum is the green line, cyan line is the continuum, red vertical line are the integration extremes, red area is the RMS and light green area is the sky noise. The right panel shows the sky spectrum in green and the grey area is the sky noise.*

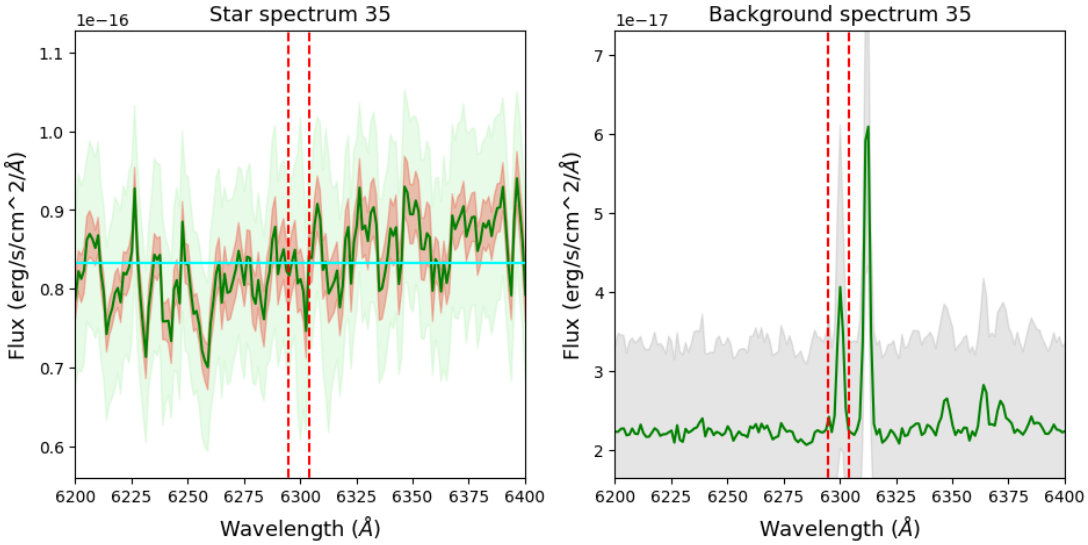

Figure 4.6: *Oxygen line at 6300Å of star 35. Left panel: spectrum is the green line, cyan line is the continuum, red vertical line are the integration extremes, red area is the RMS and light green area is the sky noise. The right panel shows the sky spectrum in green and the grey area is the sky noise.*

Star ID	*f(peak)* erg/Å/s/cm^2	Line peak RMS erg/Å/s/cm^2	F erg/s/cm^2	ΔF_{RMS} erg/s/cm^2	ΔF_{sky} erg/s/cm^2	Upper limit	Good flux
0.0	3.2e-18	1.1e-18	5.4e-17	1.8e-17	6.5e-17	True	False
1.0	6.7e-16	2.2e-16	1.9e-14	6.5e-15	3.0e-16	True	False
2.0	1.2e-17	4.0e-18	2.3e-16	7.7e-17	6.6e-17	True	False
3.0	3.3e-18	1.1e-18	4.7e-17	1.6e-17	6.0e-17	True	False
4.0	7.1e-17	4.1e-18	2.5e-16	7.1e-17	1.1e-16	False	True
5.0	3.3e-18	1.1e-18	4.4e-17	1.5e-17	5.5e-17	True	False
6.0	3.2e-18	1.1e-18	4.4e-17	1.5e-17	5.4e-17	True	False
7.0	3.3e-18	1.1e-18	6.1e-17	2.0e-17	6.6e-17	True	False
8.0	4.5e-17	8.8e-19	1.4e-16	2.8e-17	6.3e-17	False	True
9.0	4.5e-18	1.5e-18	6.8e-17	2.3e-17	1.2e-16	True	False
...	...	...	...	...	...	...	

Table 4.2: *In this table results of the [OI] line integration for the first 10 stars are shown. The stars identification (ID) numbers are listed in the first column; the second and third columns present the peak flux value of the line and the RMS value at the peak of the line; in the fourth, the fifth and the sixth columns the results of the integration are shown, the two errors are calculated with the median value of the RMS and with the sky noise; the seventh column reports the presence of upper limit with "True" and inversely "False" indicated its absence; the last column indicates the presence of good measure of F with "True", on the contrary "False" is a bad measure.*

The following plot gives an overview of the integration results for the oxygen forbidden emission line. The grey arrows represent the upper limits. The cyan dots are the uncertain measures, in fact their errorbars are very long due to the large error brought by the sky subtraction. The blue dots are the acceptable results. As it is possible to see only for a few stars lines are detected and even less stars have a "good" measurements

of the integrated flux. Summary plots of the other lines are in the dedicated appendix C.

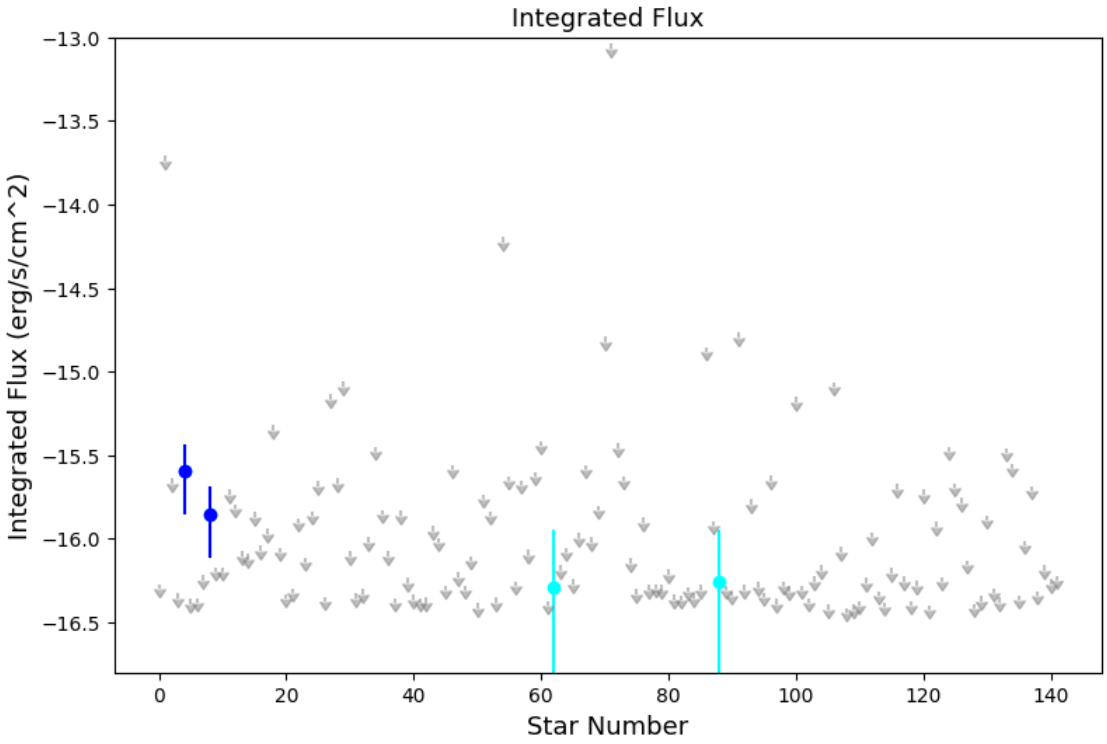

Figure 4.7: *Integrated flux results of oxygen forbidden line at 6300Å for each star of the catalogue. Blue dots are the so-called good measures, cyan dots are the value for which a large error there is and grey arrows indicates upper limits, because lines are not detected.*

Chapter 5

Conclusions and perspectives

This chapter is dedicated to the conclusions and the perspectives of this work. In the section 5.1 a summary of the work is given. The section 5.2 is centered on the future goals and needs of the photoevaporation effect studies.

5.1 Conclusions

Following the process described in the previous chapter, the values of the integrated line flux for the oxygen line at 6300$\mathring{A}$ are found. These can now be compared with the models which describe the theoretical results of the [OI] line expected if the disc is affected by external photoevaporation. The models are taken from the work done by Ballabio et al., 2023. These theoretical predictions are shown in the figure 5.1: the dotted red line is the model for a disc with a radius of 20AU, the dashed one refers to the models for 50AU disc wide and the solid line describes the model for a disc 100AU large. Before discussing about the comparison of our results with the model it is important to specify that line fluxes must be dereddened. This is because the observation is affected by interstellar extinction and this causes the reddening of our results. So the "intrinsic" values of F are expected to be larger than the "observed" ones. To perform this task a extinction law must be used, in this work we use the extinction law as parametrized by Cardelli et al., 1989, using Rv=4.4, which is appropriate for the Carina region. We also use the average extinction towards the cluster of Av=2.4, as determined by Itrich et al., 2023. In practice, a term, called extinction factor, must be added to the extracted fluxes in order to get the intrinsic ones. This factor is a function of the wavelength, in fact it must be computed for the wavelength of the considered line. Finally the corrected results are found and they are shown in the figure 5.1. The blue and cyan dots are located close to the predictions for large discs (i.e. 100AU). These points are those in which the line is detected (cyan) and the F has been determined with good accuracy (blue). The fact that they follow the model of large disc implies that these four stars are still surrounded by

a large disc (undergoing external photoevaporation). The stars with upper limits to the [OI] emission have already lost their outer disc to the FUV photoevaporation process. While some of the upper limits (marked as grey arrows) are still consistent with large discs, most of them are suggesting that those stars have a smaller disc (or no disc at all). This means that those PPDs have already experienced external photoevaporation and so they are reduced in size or disappeared.

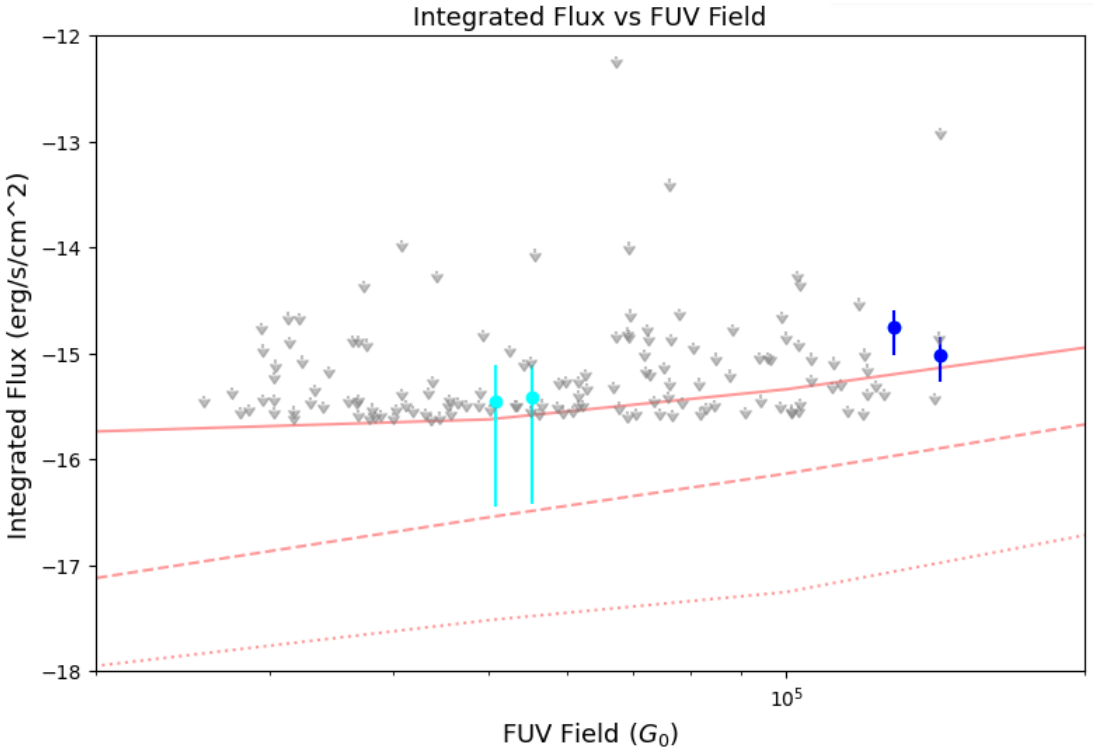

Figure 5.1: *Integrated flux of oxygen forbidden line at 6300Å as a funcion of FUV field in G_0 unit. Blue dots are the so-called good measures, cyan dots are the values for which a large sky emission there is and grey arrows indicates upper limits. The red dotted line represents the model of emission due to external photoevaporation for a disc 20AU wide. The red dashed line is the model for a disc 50AU large. The solid red line is the model for 100AU wide disc.*

Another useful comparison is to add to the previous plot the oxygen line integrated fluxes taken from the work of Natta et al., 2014. In this paper the measured lines are produced in the σOrionis cluster, which is located in the Orion star forming region and its distance from the solar system is of 360 pc. To compare properly these results with the Tr14 ones, it is necessary to scale the integrated fluxes by a factor of $(360pc/2350pc)^2$. Literature results are shown as green dots in the figure 5.2. The average ambient FUV in the σOri cluster is much smaller than in Tr14 (and dominated by the star σOri A itself, of spectral type O9.5V). External photoevaporation only affect the stars closest to σOri A, as shown in Fig.5.2 by the two rightmost green dots. The remaining green

dots are too far from σOri to be affected by significant external photoevaporation. The oxygen emission lines in these sources are emitted by a different process (e.g. internal photoevaporation). The plots that show the F as a function of the FUV field are in the dedicated appendix C. The comparison with the models is done only for the forbidden oxygen line.

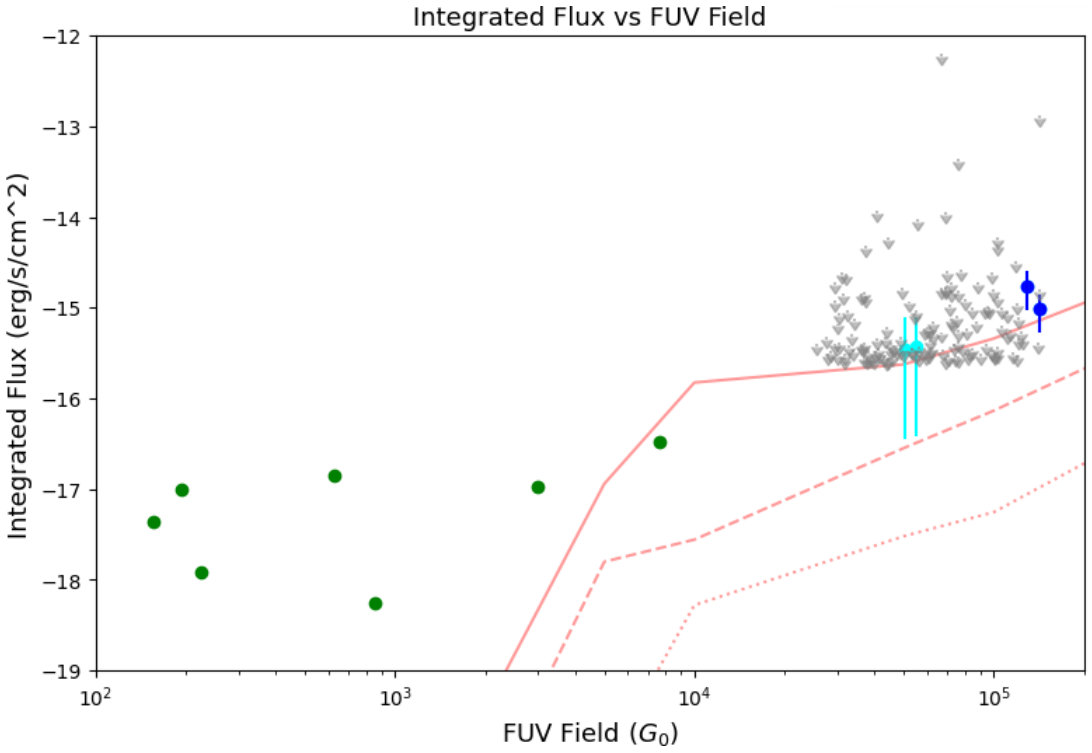

Figure 5.2: *Integrated flux of oxygen forbidden line at 6300Å as a funcion of FUV field in G_0 unit. Blue dots are the so-called good measures, cyan dots are the values for which a large sky emission there is and grey arrows indicates upper limits. Green dots are the data of the oxygen line measured in σ Orionis cluster. The red dotted line represents the model of emission due to external photoevaporation for a disc 20AU wide. The red dashed line is the model for a disc 50AU large. The solid red line is the model referred to 100AU wide disc.*

It is possible to give a physical analysis of the integrated fluxes also with the comparison of other quantities (e.g. mass of the star or the effective temperature, etc.). But, for the lack of the detection and acceptable results no physical analysis is given. These plots are shown in appendix C not only for the [OI] line, but also for the other studied lines. Finally, as summary it is possible to confirm that the careful extraction of the spectra and the detailed analysis of the sky emission and the associated noise have an important role in this work. For some lines, for examples [OI]6300 or HeI5876, the accurate procedure of extraction, sky subtraction and flux calculation is capable to produce some accurate values and it is surely a great step toward a major capability to

study PPDs with MUSE, but it is also true that the faintest lines (e.g. HeI6678) remain undetectable due to the presence of the background and so it is still a problem studying these lines. So we are limited by the background subtraction.

5.2 Perspectives

This work is the first step of the scientific research about the study of discs dispersal in high FUV environments with MUSE. The next step is to apply this method to all the pointings which form the observations of Trumpler 14 and extend the study to Tr16, another of the clusters observed with MUSE. This analysis focused only on one line of the stars spectra ([OI]6300), there is the need to compare the results with models of the other lines, these models are currently under development. Then it is important to enlarge the research to different clusters in order to have different views of the discs dispersion phenomena, in fact it is useful to study clusters which are in different environments and have different ages, in order to derive the timescale for full disc removal by external photoevaporation. The future research in this field will surely face the same problems of this work, which are related to the variable and high sky emission, indeed all the young clusters are found in the parental cloud and so the sky always affects the observations. An improvement to this method could be to create a more sophisticated algorithm which calculates AC changing the apertures in each slice of the data cube, this could be implemented taking care of the fact that stars PSFs are changing with wavelength and so it is useful to select the proper apertures to do photometry as a function of wavelength as well. Surely, the major improvement will arrive by the developing of new instruments which will guarantee a better spectral resolution while performing integral field spectroscopy in order to better separate the broader spectral lines associated to the disc-star system, from the narrow nebular emission lines. Finally, another improvement will come from higher angular resolution (e.g. with adaptive optics modes of MUSE), which would reduce the sky contribution for each star, at the price of a smaller field of view. These advancements could allow us to obtain more accurate measurements of the emission lines from the disc-star system and thus have a better understanding of the discs evolution.

Appendix A

This appendix is dedicated to present the other line studied. For shortness only the emission lines of the star with ID=4 are reported here. The integrated flux estimation is made for each line of each star following the description given in the fourth chapter of this thesis.

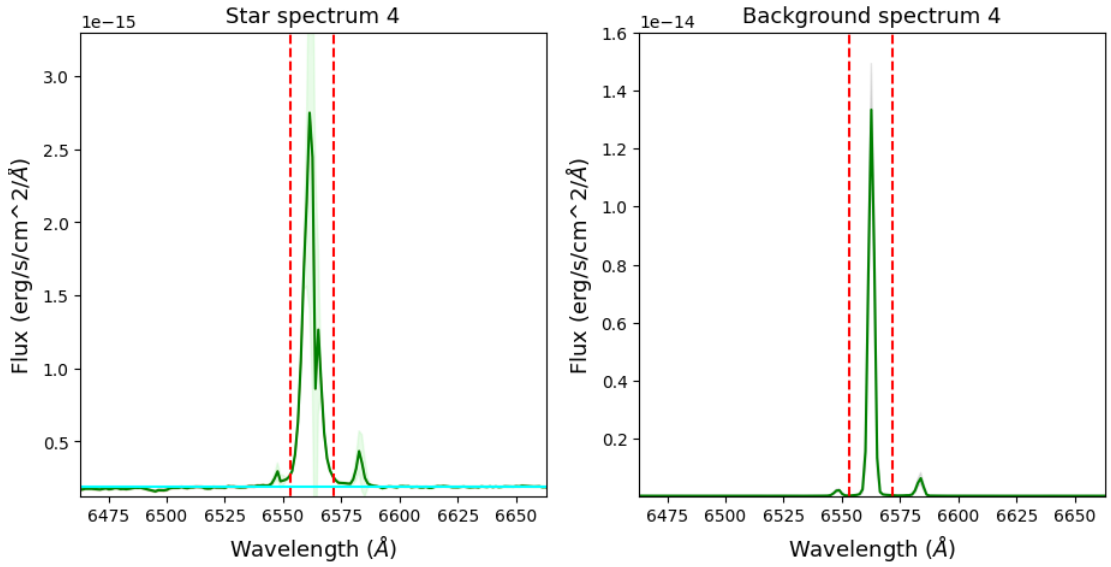

Figure A.1: *Hydrogen emission line Hα at 6563Å of star 4. Left panel: spectrum is the green line, cyan line is the continuum, red vertical line are the integration extremes, red area is the RMS and light green area is the sky noise. The right panel shows the sky spectrum in green and the grey area is the sky noise.*

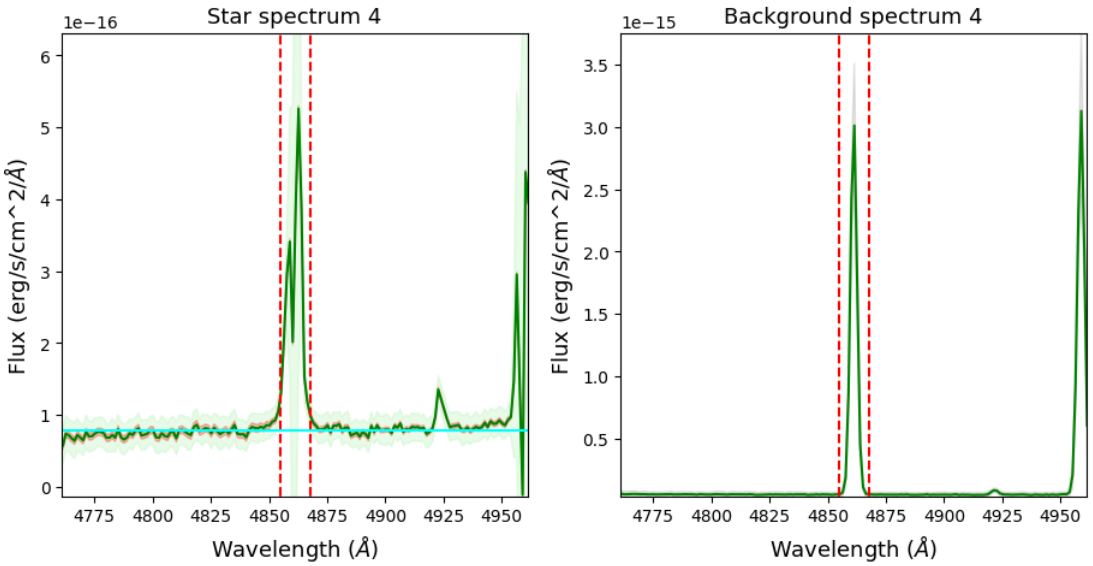

Figure A.2: *Hydrogen emission line Hβ at 4861Å of star 4. Left panel: spectrum is the green line, cyan line is the continuum, red vertical line are the integration extremes, red area is the RMS and light green area is the sky noise. The right panel shows the sky spectrum in green and the grey area is the sky noise.*

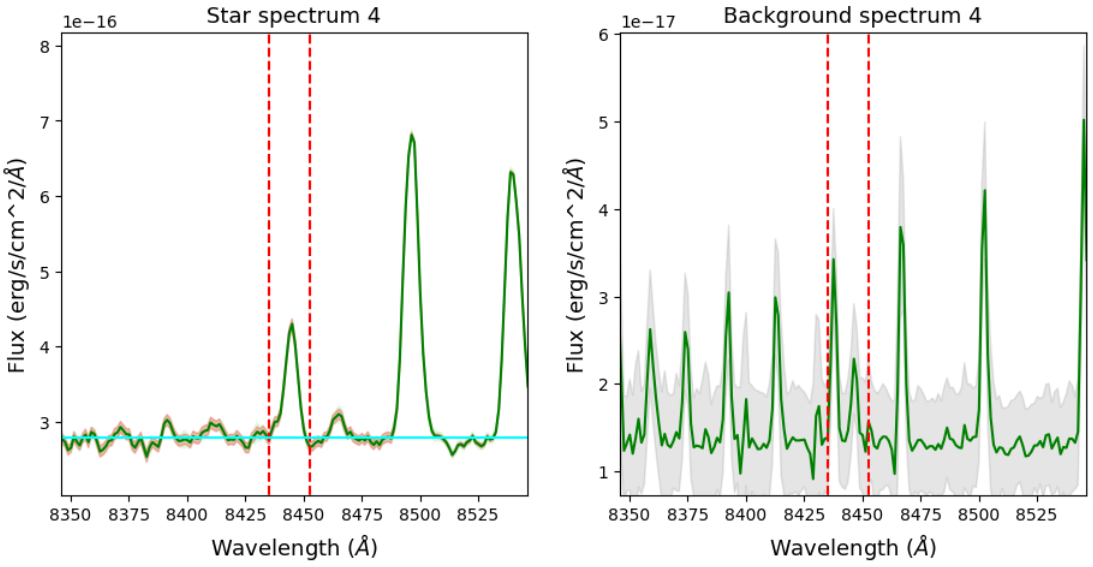

Figure A.3: *Oxygen emission line at 8446Å of star 4. Left panel: spectrum is the green line, cyan line is the continuum, red vertical line are the integration extremes, red area is the RMS and light green area is the sky noise. The right panel shows the sky spectrum in green and the grey area is the sky noise.*

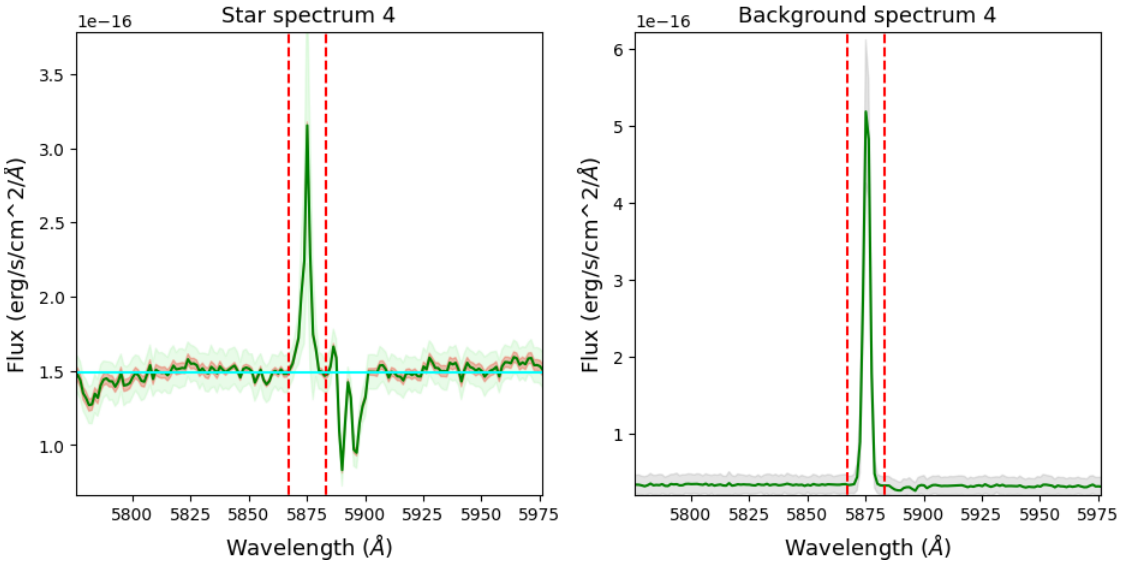

Figure A.4: *Helium emission line at 5876Å of star 4. Left panel: spectrum is the green line, cyan line is the continuum, red vertical line are the integration extremes, red area is the RMS and light green area is the sky noise. The right panel shows the sky spectrum in green and the grey area is the sky noise.*

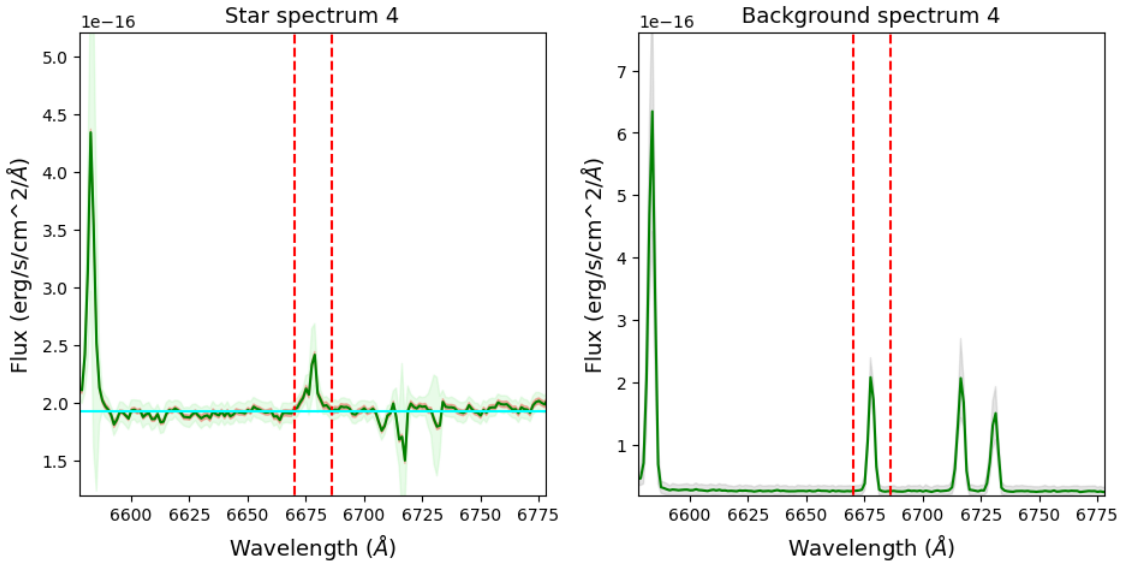

Figure A.5: *Helium emission line at 6678Å of star 4. Left panel: spectrum is the green line, cyan line is the continuum, red vertical line are the integration extremes, red area is the RMS and light green area is the sky noise. The right panel shows the sky spectrum in green and the grey area is the sky noise.*

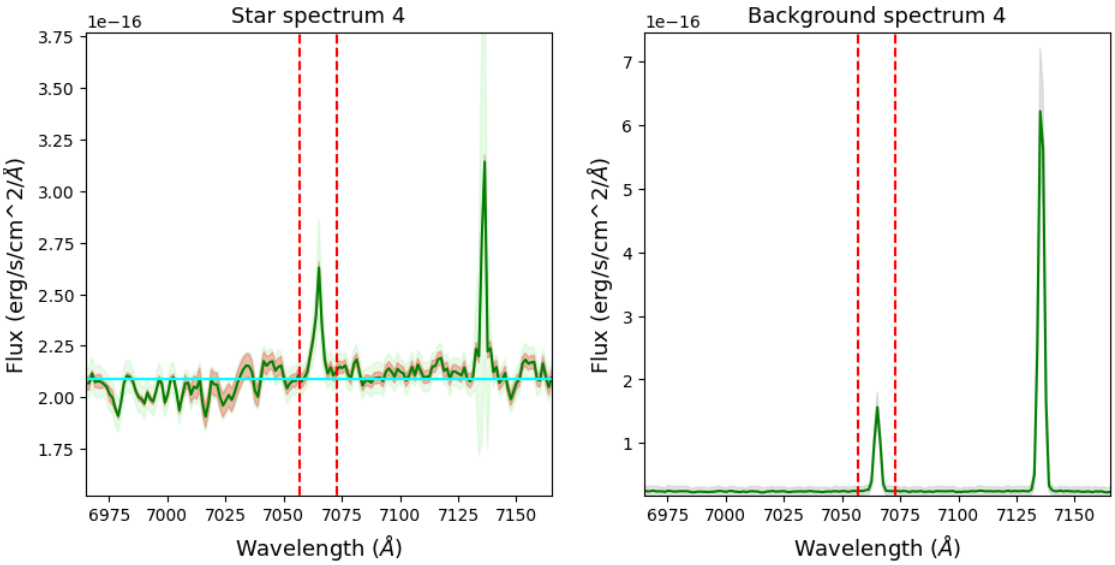

Figure A.6: *Helium emission line at 7065Å of star 4. Left panel: spectrum is the green line, cyan line is the continuum, red vertical line are the integration extremes, red area is the RMS and light green area is the sky noise. The right panel shows the sky spectrum in green and the grey area is the sky noise.*

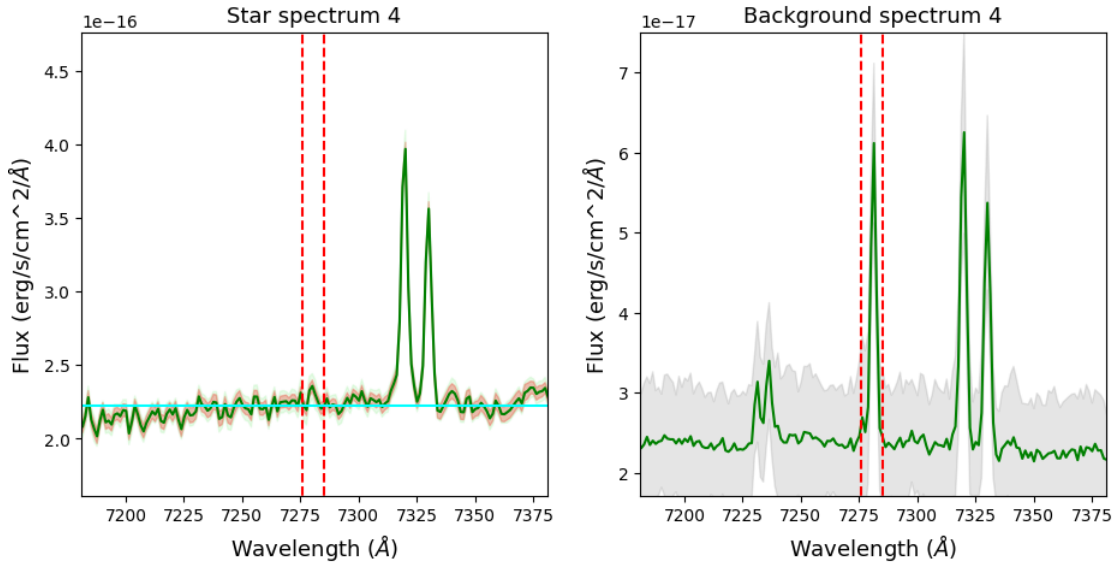

Figure A.7: *Helium emission line at 7281Å of star 4. Left panel: spectrum is the green line, cyan line is the continuum, red vertical line are the integration extremes, red area is the RMS and light green area is the sky noise. The right panel shows the sky spectrum in green and the grey area is the sky noise.*

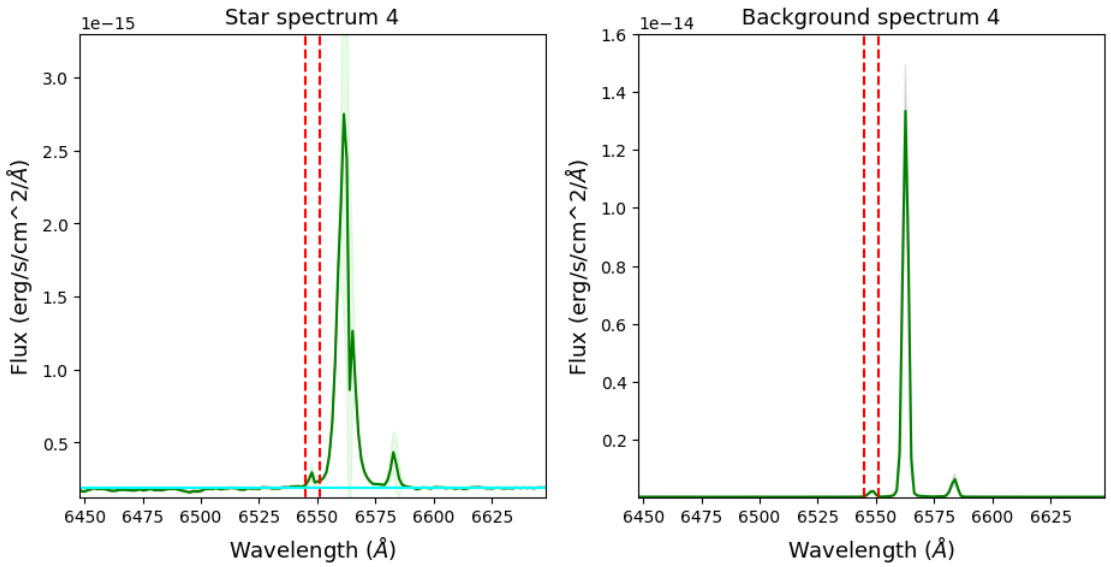

Figure A.8: *Forbidden nitrogen emission line at 6548Å of star 4. Left panel: spectrum is the green line, cyan line is the continuum, red vertical line are the integration extremes, red area is the RMS and light green area is the sky noise. The right panel shows the sky spectrum in green and the grey area is the sky noise.*

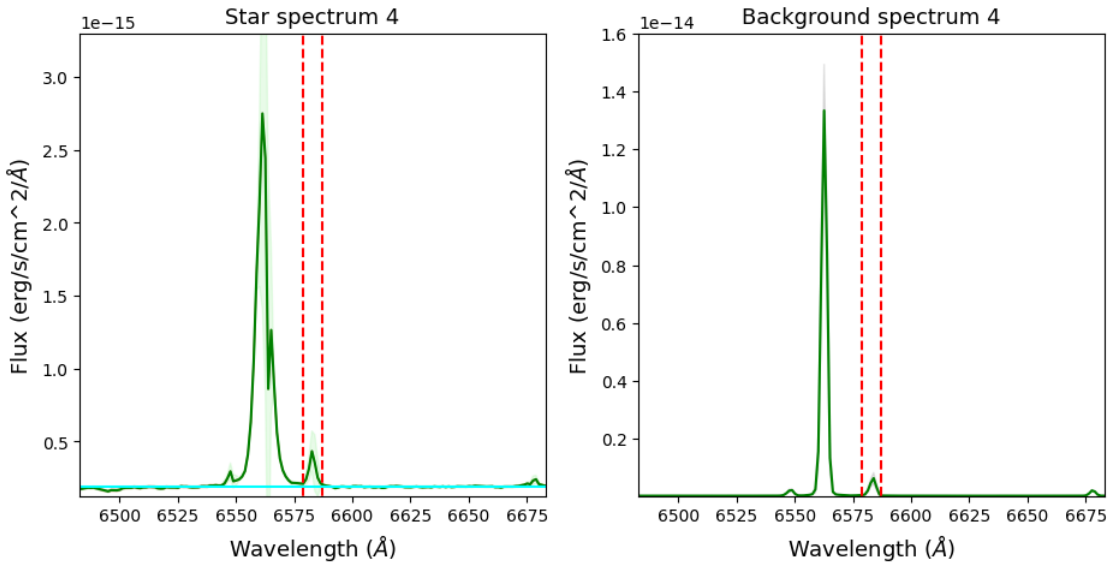

Figure A.9: *Forbidden nitrogen emission line at 6583Å of star 4. Left panel: spectrum is the green line, cyan line is the continuum, red vertical line are the integration extremes, red area is the RMS and light green area is the sky noise. The right panel shows the sky spectrum in green and the grey area is the sky noise.*

Appendix B

Tables of the results are shown in this appendix. In order to not be repetitive, tables are presented without the caption. The caption is the same of the table 4.2. To distinguish the lines results, each table is anticipated by a title, which contains the name of the line and its wavelength.

Hα 6563$\mathring{A}$

Star ID	*f(peak)* erg/Å/s/cm^2	Line peak RMS erg/Å/s/cm^2	F erg/s/cm^2	ΔF_{RMS} erg/s/cm^2	ΔF_{sky} erg/s/cm^2	Upper limit	Good flux
0.0	3.0e-16	1.1e-18	8.7e-16	1.9e-16	3.1e-15	False	False
1.0	5.8e-16	1.9e-16	3.9e-14	1.3e-14	4.6e-15	True	False
2.0	1.4e-17	4.7e-18	7.0e-16	2.3e-16	5.1e-15	True	False
3.0	2.8e-18	9.3e-19	1.1e-15	3.5e-16	3.4e-15	True	False
4.0	2.6e-15	3.9e-18	1.6e-14	6.4e-16	7.4e-15	False	True
5.0	5.2e-16	9.6e-19	9.5e-16	3.0e-16	5.4e-15	False	False
6.0	1.1e-15	9.8e-19	4.0e-15	2.8e-16	4.6e-15	False	False
7.0	2.5e-15	1.1e-18	4.9e-15	5.2e-16	4.0e-15	False	False
8.0	2.4e-15	9.8e-19	6.3e-15	6.4e-16	4.0e-15	False	False
9.0	4.4e-18	1.5e-18	1.1e-15	3.6e-16	5.4e-15	True	False
10.0	6.9e-16	1.6e-18	2.4e-15	1.4e-16	6.1e-15	False	False
11.0	7.1e-18	2.4e-18	1.1e-15	3.8e-16	4.4e-15	True	False
12.0	2.4e-16	2.9e-18	3.7e-16	1.1e-16	4.3e-15	False	False
13.0	9.4e-16	1.2e-18	2.9e-15	1.8e-16	5.2e-15	False	False
14.0	3.1e-18	1.0e-18	3.4e-15	1.1e-15	5.6e-15	True	False
15.0	7.0e-18	2.3e-18	4.1e-16	1.4e-16	4.1e-15	True	False
16.0	6.7e-16	1.4e-18	9.2e-16	2.0e-16	5.0e-15	False	False
17.0	2.7e-15	1.8e-18	6.1e-15	9.0e-16	3.8e-15	False	False
18.0	5.9e-16	4.7e-18	2.4e-15	4.9e-16	4.5e-15	False	False
19.0	1.5e-15	1.3e-18	4.7e-15	3.9e-16	4.5e-15	False	False
20.0	1.1e-15	8.8e-19	3.7e-15	2.0e-16	3.8e-15	False	False
21.0	2.6e-18	8.6e-19	1.1e-15	3.5e-16	4.3e-15	True	False
22.0	1.2e-15	1.8e-18	2.7e-15	2.4e-16	4.0e-15	False	False
23.0	1.9e-15	1.1e-18	4.0e-15	1.9e-16	4.1e-15	False	False
24.0	5.0e-18	1.7e-18	7.1e-16	2.4e-16	5.0e-15	True	False
25.0	1.4e-15	2.5e-18	6.1e-15	8.9e-16	3.0e-15	False	True
26.0	3.0e-18	9.9e-19	2.6e-16	8.8e-17	5.4e-15	True	False
27.0	2.4e-15	1.1e-17	9.7e-15	7.1e-16	4.8e-15	False	True
28.0	8.7e-18	2.9e-18	9.8e-16	3.3e-16	3.9e-15	True	False
29.0	3.5e-17	1.2e-17	1.9e-15	6.3e-16	5.8e-15	True	False
30.0	4.3e-18	1.4e-18	1.3e-15	4.4e-16	5.2e-15	True	False
31.0	1.5e-15	1.3e-18	3.8e-15	3.6e-16	6.4e-15	False	False

32.0	3.1e-18	1.0e-18	1.9e-15	6.2e-16	4.8e-15	True	False
33.0	7.4e-16	1.5e-18	2.0e-15	1.6e-16	4.1e-15	False	False
34.0	1.2e-15	4.7e-18	4.1e-15	3.8e-16	6.3e-15	False	False
35.0	6.9e-18	2.3e-18	8.1e-16	2.7e-16	6.0e-15	True	False
36.0	4.7e-18	1.6e-18	2.4e-15	7.8e-16	5.8e-15	True	False
37.0	3.0e-18	9.9e-19	1.8e-15	6.1e-16	4.2e-15	True	False
38.0	6.6e-18	2.2e-18	7.9e-16	2.6e-16	5.6e-15	True	False
39.0	4.2e-18	1.4e-18	8.2e-16	2.7e-16	4.9e-15	True	False
40.0	1.8e-15	1.0e-18	4.8e-15	6.8e-16	4.4e-15	False	False
41.0	2.9e-18	9.6e-19	2.0e-15	6.6e-16	6.1e-15	True	False
42.0	2.9e-18	9.8e-19	1.0e-15	3.3e-16	4.2e-15	True	False
43.0	4.2e-18	1.4e-18	2.2e-15	7.2e-16	7.5e-15	True	False
44.0	8.9e-16	1.3e-18	2.4e-15	5.5e-16	3.9e-15	False	False
45.0	2.1e-15	9.8e-19	5.2e-15	1.1e-15	5.6e-15	False	False
46.0	1.3e-17	4.2e-18	8.7e-16	2.9e-16	3.5e-15	True	False
47.0	3.5e-18	1.2e-18	9.1e-16	3.0e-16	5.7e-15	True	False
48.0	1.7e-15	9.0e-19	3.8e-15	3.4e-16	3.4e-15	False	False
49.0	4.8e-18	1.6e-18	7.6e-16	2.5e-16	1.2e-14	True	False
50.0	3.4e-18	1.1e-18	9.6e-16	3.2e-16	9.8e-15	True	False
51.0	7.4e-18	2.5e-18	1.3e-15	4.4e-16	3.6e-15	True	False
52.0	1.3e-15	1.6e-18	1.9e-15	6.1e-16	3.4e-15	False	False
53.0	3.0e-18	1.0e-18	5.3e-16	1.8e-16	3.4e-15	True	False
54.0	2.6e-16	8.6e-17	1.9e-14	6.3e-15	4.1e-15	True	False
55.0	9.1e-18	3.0e-18	1.9e-15	6.2e-16	9.5e-15	True	False
56.0	4.1e-18	1.4e-18	1.4e-15	4.8e-16	4.7e-15	True	False
57.0	3.8e-16	3.3e-18	7.8e-16	2.5e-16	3.9e-15	False	False
58.0	3.3e-15	1.3e-18	1.0e-14	4.2e-16	8.1e-15	False	False
59.0	1.3e-15	2.7e-18	4.3e-15	5.5e-16	6.7e-15	False	False
60.0	5.4e-16	5.6e-18	2.9e-15	6.5e-16	4.0e-15	False	False
61.0	1.2e-15	9.9e-19	3.9e-15	2.6e-16	4.4e-15	False	False
62.0	7.5e-16	1.2e-18	1.4e-15	1.6e-16	4.9e-15	False	False
63.0	3.5e-18	1.2e-18	2.3e-15	7.8e-16	7.3e-15	True	False
64.0	3.6e-15	1.2e-18	1.2e-14	1.0e-15	6.3e-15	False	False
65.0	7.2e-16	1.4e-18	1.5e-15	1.9e-16	6.5e-15	False	False
66.0	4.1e-18	1.4e-18	6.5e-16	2.2e-16	8.4e-15	True	False
67.0	3.6e-16	3.3e-18	6.7e-16	1.5e-16	7.1e-15	False	False
68.0	3.7e-18	1.2e-18	2.1e-15	7.1e-16	6.7e-15	True	False
69.0	6.4e-16	1.4e-18	1.2e-15	3.7e-16	5.7e-15	False	False
70.0	7.1e-17	2.4e-17	3.3e-15	1.1e-15	6.6e-15	True	False
71.0	9.5e-16	3.2e-16	1.0e-13	3.4e-14	7.8e-15	True	False
72.0	1.3e-17	4.4e-18	1.6e-15	5.3e-16	7.7e-15	True	False
73.0	8.1e-18	2.7e-18	7.2e-16	2.4e-16	5.1e-15	True	False
74.0	4.5e-18	1.5e-18	2.6e-15	8.6e-16	6.0e-15	True	False
75.0	3.3e-18	1.1e-18	9.7e-16	3.2e-16	4.8e-15	True	False
76.0	1.4e-15	2.0e-18	2.9e-15	2.5e-16	4.4e-15	False	False
77.0	2.5e-18	8.5e-19	8.9e-16	3.0e-16	4.1e-15	True	False
78.0	2.8e-18	9.3e-19	2.3e-15	7.8e-16	5.1e-15	True	False
79.0	1.0e-15	1.0e-18	3.1e-15	1.2e-16	5.0e-15	False	False
80.0	4.4e-18	1.5e-18	1.1e-15	3.7e-16	4.7e-15	True	False
81.0	3.2e-18	1.1e-18	3.5e-16	1.2e-16	5.7e-15	True	False
82.0	2.8e-18	9.2e-19	7.9e-16	2.6e-16	4.2e-15	True	False
83.0	3.3e-18	1.1e-18	9.3e-16	3.1e-16	1.9e-15	True	False
84.0	1.3e-15	1.1e-18	2.4e-15	6.3e-16	4.1e-15	False	False
85.0	2.0e-15	6.5e-19	5.8e-15	5.2e-16	5.1e-15	False	False
86.0	8.0e-16	1.7e-17	2.2e-15	6.1e-16	2.0e-15	False	False
87.0	4.0e-18	1.3e-18	1.7e-15	5.8e-16	2.3e-15	True	False
88.0	3.3e-18	1.1e-18	1.0e-15	3.4e-16	4.2e-15	True	False
89.0	3.1e-18	1.0e-18	1.1e-15	3.5e-16	3.2e-15	True	False
90.0	1.3e-15	1.1e-18	1.4e-15	4.5e-16	4.0e-15	False	False
91.0	7.4e-17	2.5e-17	4.2e-15	1.4e-15	3.4e-15	True	False
92.0	9.2e-16	1.2e-18	2.0e-15	1.8e-16	2.5e-15	False	False
93.0	6.9e-16	2.2e-18	4.6e-15	4.6e-16	2.5e-15	False	False

94.0	3.4e-18	1.1e-18	1.7e-15	5.6e-16	6.5e-15	True	False
95.0	6.7e-16	9.6e-19	2.6e-15	2.2e-16	2.4e-15	False	False
96.0	1.1e-17	3.8e-18	5.7e-16	1.9e-16	3.4e-15	True	False
97.0	2.9e-18	9.5e-19	1.2e-15	3.9e-16	1.9e-15	True	False
98.0	2.9e-18	9.5e-19	3.2e-15	1.1e-15	6.2e-15	True	False
99.0	5.3e-16	9.5e-19	1.3e-15	2.5e-16	1.4e-15	False	False
100.0	3.0e-17	1.0e-17	2.1e-15	6.9e-16	7.1e-15	True	False
101.0	2.9e-18	9.6e-19	1.4e-15	4.7e-16	6.3e-15	True	False
102.0	2.6e-18	8.8e-19	8.1e-16	2.7e-16	3.0e-15	True	False
103.0	2.6e-16	1.3e-18	2.5e-16	5.4e-17	2.9e-15	False	False
104.0	3.3e-18	1.1e-18	5.1e-16	1.7e-16	1.6e-15	True	False
105.0	2.9e-18	9.7e-19	1.6e-15	5.3e-16	2.1e-15	True	False
106.0	6.2e-17	2.1e-17	2.8e-15	9.3e-16	2.7e-15	True	False
107.0	1.7e-15	1.4e-18	5.5e-15	4.4e-16	3.7e-15	False	False
108.0	8.8e-16	9.2e-19	1.7e-15	1.1e-16	3.5e-15	False	False
109.0	1.0e-15	8.7e-19	3.3e-15	9.4e-17	6.6e-15	False	False
110.0	1.4e-15	1.1e-18	4.8e-15	1.8e-16	6.1e-15	False	False
111.0	3.2e-18	1.1e-18	4.3e-16	1.4e-16	6.1e-15	True	False
112.0	2.5e-15	1.4e-18	8.4e-15	9.7e-16	8.3e-15	False	False
113.0	3.4e-18	1.1e-18	7.2e-16	2.4e-16	5.4e-15	True	False
114.0	1.1e-15	8.8e-19	2.1e-15	6.2e-16	2.8e-15	False	False
115.0	3.4e-18	1.1e-18	3.7e-16	1.2e-16	2.7e-15	True	False
116.0	9.2e-18	3.1e-18	5.4e-16	1.8e-16	5.6e-15	True	False
117.0	2.8e-18	9.2e-19	1.5e-15	5.1e-16	4.3e-15	True	False
118.0	2.9e-18	9.7e-19	7.5e-16	2.5e-16	2.9e-15	True	False
119.0	2.9e-15	9.6e-19	5.4e-15	4.4e-16	9.8e-15	False	False
120.0	6.7e-18	2.2e-18	3.7e-16	1.2e-16	2.5e-15	True	False
121.0	5.6e-16	8.5e-19	1.2e-15	1.7e-16	2.2e-15	False	False
122.0	5.5e-15	1.1e-18	1.6e-14	1.7e-15	6.9e-15	False	True
123.0	1.3e-15	1.2e-18	3.5e-15	6.0e-16	7.1e-15	False	False
124.0	1.4e-17	4.8e-18	1.9e-15	6.3e-16	9.4e-15	True	False
125.0	5.1e-16	2.2e-18	1.4e-15	1.3e-16	3.1e-15	False	False
126.0	3.7e-15	2.5e-18	1.1e-14	7.5e-16	6.9e-15	False	False
127.0	3.0e-18	1.0e-18	2.0e-15	6.6e-16	3.6e-15	True	False
128.0	8.5e-16	9.2e-19	2.6e-15	3.0e-16	2.9e-15	False	False
129.0	2.8e-18	9.4e-19	1.7e-15	5.6e-16	4.7e-15	True	False
130.0	4.8e-18	1.6e-18	1.7e-15	5.6e-16	2.5e-15	True	False
131.0	3.5e-18	1.2e-18	4.2e-16	1.4e-16	3.3e-15	True	False
132.0	3.0e-18	9.9e-19	1.4e-15	4.8e-16	7.7e-15	True	False
133.0	1.6e-17	5.3e-18	1.0e-15	3.5e-16	2.8e-15	True	False
134.0	1.1e-15	4.4e-18	3.8e-15	5.5e-16	4.5e-15	False	False
135.0	2.6e-18	8.7e-19	1.6e-15	5.4e-16	4.9e-15	True	False
136.0	4.6e-18	1.5e-18	1.1e-15	3.7e-16	2.6e-15	True	False
137.0	1.1e-17	3.8e-18	1.0e-15	3.5e-16	2.2e-15	True	False
138.0	2.1e-15	8.5e-19	5.5e-15	4.9e-16	4.3e-15	False	False
139.0	1.4e-15	1.3e-18	4.4e-15	3.6e-16	3.5e-15	False	False
140.0	1.7e-15	6.4e-19	4.6e-15	3.5e-16	7.3e-15	False	False
141.0	2.2e-15	1.2e-18	5.6e-15	1.6e-15	4.7e-15	False	False

Hβ 4861$\mathring{A}$

Star ID	*f(peak)* erg/Å/s/cm^2	Line peak RMS erg/Å/s/cm^2	F erg/s/cm^2	ΔF_{RMS} erg/s/cm^2	ΔF_{sky} erg/s/cm^2	Upper limit	Good flux
0.0	8.6e-18	2.9e-18	7.1e-16	2.4e-16	1.0e-15	True	False
1.0	2.0e-15	6.6e-16	8.1e-14	2.7e-14	1.4e-15	True	False
2.0	3.0e-17	1.0e-17	2.4e-15	8.0e-16	1.4e-15	True	False
3.0	7.3e-18	2.4e-18	6.1e-16	2.0e-16	9.5e-16	True	False
4.0	4.5e-16	4.4e-18	2.5e-15	5.1e-16	2.2e-15	False	False
5.0	7.8e-18	2.6e-18	6.0e-16	2.0e-16	1.2e-15	True	False
6.0	7.3e-18	2.4e-18	1.5e-15	5.0e-16	1.1e-15	True	False
7.0	8.7e-18	2.9e-18	2.1e-15	6.9e-16	1.1e-15	True	False
8.0	8.0e-18	2.7e-18	2.2e-15	7.3e-16	1.0e-15	True	False
9.0	1.0e-17	3.4e-18	1.1e-15	3.5e-16	1.7e-15	True	False
10.0	8.3e-18	2.8e-18	1.5e-15	5.1e-16	1.6e-15	True	False
11.0	7.7e-18	2.6e-18	8.4e-16	2.8e-16	1.1e-15	True	False
12.0	6.2e-18	2.1e-18	3.7e-16	1.2e-16	1.2e-15	True	False
13.0	7.9e-18	2.6e-18	7.9e-16	2.6e-16	1.2e-15	True	False
14.0	7.8e-18	2.6e-18	3.4e-15	1.1e-15	1.5e-15	True	False
15.0	8.6e-18	2.9e-18	1.5e-15	5.1e-16	1.0e-15	True	False
16.0	6.0e-18	2.0e-18	2.5e-16	8.5e-17	1.2e-15	True	False
17.0	7.3e-18	2.4e-18	2.5e-15	8.3e-16	1.0e-15	True	False
18.0	1.2e-17	3.9e-18	5.8e-16	1.9e-16	1.2e-15	True	False
19.0	8.8e-18	2.9e-18	7.9e-16	2.6e-16	1.3e-15	True	False
20.0	6.5e-18	2.2e-18	1.5e-15	4.9e-16	1.1e-15	True	False
21.0	7.0e-18	2.3e-18	1.3e-15	4.4e-16	1.0e-15	True	False
22.0	7.8e-18	2.6e-18	1.8e-15	6.0e-16	1.2e-15	True	False
23.0	8.1e-18	2.7e-18	3.9e-15	1.3e-15	1.2e-15	True	False
24.0	8.2e-18	2.7e-18	1.8e-15	6.0e-16	1.3e-15	True	False
25.0	7.4e-18	2.5e-18	1.7e-15	5.8e-16	7.9e-16	True	False
26.0	7.9e-18	2.6e-18	8.9e-16	3.0e-16	1.5e-15	True	False
27.0	2.8e-17	9.2e-18	2.8e-15	9.4e-16	1.2e-15	True	False
28.0	9.4e-18	3.1e-18	1.9e-15	6.5e-16	1.0e-15	True	False
29.0	4.4e-17	1.5e-17	1.5e-15	5.0e-16	1.5e-15	True	False
30.0	8.4e-18	2.8e-18	1.2e-15	4.1e-16	1.3e-15	True	False
31.0	5.7e-18	1.9e-18	1.7e-15	5.7e-16	1.6e-15	True	False
32.0	7.0e-18	2.3e-18	1.8e-15	5.9e-16	1.3e-15	True	False
33.0	6.0e-18	2.0e-18	1.4e-15	4.8e-16	1.0e-15	True	False
34.0	2.1e-16	3.9e-18	7.3e-16	1.6e-16	1.7e-15	False	False
35.0	1.2e-17	4.1e-18	1.3e-15	4.4e-16	1.6e-15	True	False
36.0	8.0e-18	2.7e-18	3.3e-15	1.1e-15	1.5e-15	True	False
37.0	8.3e-18	2.8e-18	1.7e-15	5.6e-16	1.2e-15	True	False
38.0	7.6e-18	2.5e-18	6.4e-16	2.1e-16	1.5e-15	True	False
39.0	6.5e-18	2.2e-18	1.1e-15	3.6e-16	1.3e-15	True	False
40.0	6.8e-18	2.3e-18	1.6e-15	5.3e-16	1.1e-15	True	False
41.0	6.8e-18	2.3e-18	2.3e-15	7.6e-16	1.4e-15	True	False
42.0	7.6e-18	2.5e-18	6.6e-16	2.2e-16	1.2e-15	True	False
43.0	5.0e-18	1.7e-18	8.4e-16	2.8e-16	1.8e-15	True	False
44.0	8.9e-18	3.0e-18	1.6e-15	5.2e-16	1.1e-15	True	False
45.0	7.9e-18	2.6e-18	2.9e-15	9.8e-16	1.3e-15	True	False
46.0	1.2e-17	4.0e-18	1.2e-15	3.9e-16	9.3e-16	True	False
47.0	6.6e-18	2.2e-18	1.1e-15	3.8e-16	1.4e-15	True	False
48.0	6.8e-18	2.3e-18	2.0e-15	6.6e-16	9.2e-16	True	False
49.0	4.9e-18	1.6e-18	1.9e-15	6.4e-16	2.6e-15	True	False
50.0	7.9e-18	2.6e-18	1.3e-15	4.2e-16	2.3e-15	True	False
51.0	1.0e-17	3.3e-18	1.6e-15	5.3e-16	1.0e-15	True	False
52.0	8.0e-18	2.7e-18	7.3e-16	2.4e-16	9.0e-16	True	False
53.0	5.8e-18	1.9e-18	8.2e-16	2.7e-16	9.7e-16	True	False
54.0	6.8e-16	2.3e-16	3.9e-14	1.3e-14	1.1e-15	True	False
55.0	1.3e-17	4.3e-18	1.3e-15	4.4e-16	2.2e-15	True	False

56.0	7.7e-18	2.6e-18	9.8e-16	3.3e-16	1.3e-15	True	False
57.0	1.1e-17	3.7e-18	1.3e-15	4.3e-16	1.0e-15	True	False
58.0	8.0e-18	2.7e-18	4.1e-15	1.4e-15	1.9e-15	True	False
59.0	7.1e-18	2.4e-18	1.6e-15	5.2e-16	1.6e-15	True	False
60.0	1.2e-17	4.1e-18	9.2e-16	3.1e-16	1.1e-15	True	False
61.0	6.8e-18	2.3e-18	1.2e-15	4.1e-16	1.1e-15	True	False
62.0	7.9e-18	2.6e-18	8.0e-16	2.7e-16	1.2e-15	True	False
63.0	8.3e-18	2.8e-18	8.5e-16	2.8e-16	1.7e-15	True	False
64.0	6.9e-18	2.3e-18	5.5e-15	1.8e-15	1.6e-15	True	False
65.0	6.5e-18	2.2e-18	1.3e-15	4.2e-16	1.6e-15	True	False
66.0	6.3e-18	2.1e-18	7.7e-16	2.6e-16	1.8e-15	True	False
67.0	8.8e-18	2.9e-18	4.1e-16	1.4e-16	1.4e-15	True	False
68.0	5.8e-18	1.9e-18	2.6e-15	8.6e-16	1.5e-15	True	False
69.0	7.6e-18	2.5e-18	6.7e-16	2.2e-16	1.4e-15	True	False
70.0	5.9e-17	2.0e-17	1.7e-15	5.8e-16	1.8e-15	True	False
71.0	2.1e-15	7.0e-16	1.0e-13	3.4e-14	2.3e-15	True	False
72.0	9.5e-18	3.2e-18	4.4e-16	1.5e-16	2.0e-15	True	False
73.0	9.4e-18	3.1e-18	4.2e-16	1.4e-16	1.1e-15	True	False
74.0	8.7e-18	2.9e-18	1.0e-15	3.4e-16	1.6e-15	True	False
75.0	6.2e-18	2.1e-18	2.5e-16	8.3e-17	1.2e-15	True	False
76.0	6.4e-18	2.1e-18	1.3e-15	4.3e-16	1.2e-15	True	False
77.0	7.8e-18	2.6e-18	2.6e-15	8.5e-16	1.1e-15	True	False
78.0	7.4e-18	2.5e-18	1.4e-15	4.6e-16	1.4e-15	True	False
79.0	7.3e-18	2.4e-18	1.7e-15	5.7e-16	1.4e-15	True	False
80.0	1.3e-17	4.2e-18	1.9e-15	6.3e-16	1.2e-15	True	False
81.0	6.0e-18	2.0e-18	7.5e-16	2.5e-16	1.3e-15	True	False
82.0	6.6e-18	2.2e-18	1.7e-15	5.8e-16	1.1e-15	True	False
83.0	6.6e-18	2.2e-18	7.8e-16	2.6e-16	5.7e-16	True	False
84.0	7.8e-18	2.6e-18	8.9e-16	3.0e-16	9.7e-16	True	False
85.0	5.8e-18	1.9e-18	1.8e-15	6.0e-16	1.1e-15	True	False
86.0	1.9e-17	6.3e-18	1.4e-15	4.7e-16	6.0e-16	True	False
87.0	7.3e-18	2.4e-18	1.1e-15	3.7e-16	6.1e-16	True	False
88.0	5.9e-18	2.0e-18	8.5e-16	2.8e-16	1.2e-15	True	False
89.0	5.6e-18	1.9e-18	2.7e-16	9.1e-17	7.7e-16	True	False
90.0	6.6e-18	2.2e-18	6.6e-16	2.2e-16	1.0e-15	True	False
91.0	8.6e-17	2.9e-17	2.7e-15	9.1e-16	9.1e-16	True	False
92.0	6.8e-18	2.3e-18	9.2e-16	3.1e-16	5.8e-16	True	False
93.0	1.9e-16	3.0e-18	7.1e-16	1.4e-16	7.0e-16	False	False
94.0	6.9e-18	2.3e-18	1.2e-15	4.0e-16	1.5e-15	True	False
95.0	6.8e-18	2.3e-18	6.5e-16	2.2e-16	6.9e-16	True	False
96.0	1.3e-17	4.3e-18	1.0e-15	3.4e-16	8.3e-16	True	False
97.0	5.8e-18	1.9e-18	8.5e-16	2.8e-16	5.6e-16	True	False
98.0	7.9e-18	2.6e-18	2.2e-15	7.3e-16	1.4e-15	True	False
99.0	7.4e-18	2.5e-18	4.3e-16	1.4e-16	3.9e-16	True	False
100.0	5.7e-17	1.9e-17	2.5e-15	8.2e-16	1.4e-15	True	False
101.0	7.5e-18	2.5e-18	7.1e-16	2.4e-16	1.4e-15	True	False
102.0	4.1e-18	1.4e-18	1.1e-15	3.7e-16	5.9e-16	True	False
103.0	6.9e-18	2.3e-18	2.9e-16	9.8e-17	6.9e-16	True	False
104.0	5.9e-18	2.0e-18	3.0e-16	1.0e-16	4.1e-16	True	False
105.0	5.6e-18	1.9e-18	6.9e-16	2.3e-16	5.7e-16	True	False
106.0	6.7e-17	2.2e-17	3.2e-15	1.1e-15	6.9e-16	True	False
107.0	7.1e-18	2.4e-18	2.3e-15	7.6e-16	9.3e-16	True	False
108.0	7.0e-18	2.3e-18	6.1e-16	2.0e-16	8.3e-16	True	False
109.0	5.8e-18	1.9e-18	9.4e-16	3.1e-16	1.5e-15	True	False
110.0	7.3e-18	2.4e-18	1.3e-15	4.4e-16	1.4e-15	True	False
111.0	6.3e-18	2.1e-18	2.2e-15	7.4e-16	1.4e-15	True	False
112.0	6.1e-18	2.0e-18	2.9e-15	9.6e-16	1.6e-15	True	False
113.0	6.7e-18	2.2e-18	5.0e-16	1.7e-16	1.2e-15	True	False
114.0	5.6e-18	1.9e-18	8.8e-16	2.9e-16	7.1e-16	True	False
115.0	6.6e-18	2.2e-18	1.5e-15	5.0e-16	6.5e-16	True	False
116.0	9.9e-18	3.3e-18	1.4e-15	4.7e-16	1.2e-15	True	False
117.0	6.7e-18	2.2e-18	2.1e-15	7.0e-16	9.6e-16	True	False

118.0	7.0e-18	2.3e-18	1.2e-15	3.9e-16	6.2e-16	True	False
119.0	7.9e-18	2.6e-18	2.7e-15	8.9e-16	1.9e-15	True	False
120.0	8.1e-18	2.7e-18	6.9e-16	2.3e-16	6.4e-16	True	False
121.0	6.3e-18	2.1e-18	3.4e-16	1.1e-16	6.3e-16	True	False
122.0	8.1e-18	2.7e-18	5.1e-15	1.7e-15	1.5e-15	True	False
123.0	7.1e-18	2.4e-18	2.0e-15	6.5e-16	1.4e-15	True	False
124.0	1.3e-17	4.3e-18	2.3e-15	7.8e-16	1.8e-15	True	False
125.0	7.7e-18	2.6e-18	3.9e-16	1.3e-16	6.4e-16	True	False
126.0	6.8e-18	2.3e-18	3.8e-15	1.3e-15	1.3e-15	True	False
127.0	6.1e-18	2.0e-18	1.1e-15	3.8e-16	7.7e-16	True	False
128.0	6.9e-18	2.3e-18	1.0e-15	3.4e-16	7.7e-16	True	False
129.0	6.8e-18	2.3e-18	1.7e-15	5.5e-16	1.1e-15	True	False
130.0	7.8e-18	2.6e-18	7.1e-16	2.4e-16	5.5e-16	True	False
131.0	6.4e-18	2.1e-18	4.2e-16	1.4e-16	7.3e-16	True	False
132.0	6.7e-18	2.2e-18	1.3e-15	4.3e-16	1.7e-15	True	False
133.0	2.1e-17	7.1e-18	5.5e-16	1.8e-16	6.5e-16	True	False
134.0	1.2e-17	4.1e-18	8.2e-16	2.7e-16	1.1e-15	True	False
135.0	7.1e-18	2.4e-18	1.8e-15	6.0e-16	1.1e-15	True	False
136.0	8.0e-18	2.7e-18	1.6e-15	5.5e-16	6.0e-16	True	False
137.0	1.4e-17	4.5e-18	1.6e-15	5.3e-16	6.4e-16	True	False
138.0	7.6e-18	2.5e-18	2.3e-15	7.8e-16	1.1e-15	True	False
139.0	6.6e-18	2.2e-18	2.1e-15	7.1e-16	9.3e-16	True	False
140.0	1.0e-17	3.4e-18	2.1e-15	7.1e-16	1.8e-15	True	False
141.0	4.0e-16	3.0e-18	1.4e-15	3.8e-16	9.7e-16	False	False

[OI] 6300$\mathring{A}$

Star ID	*f(peak)* erg/Å/s/cm^2	Line peak RMS erg/Å/s/cm^2	F erg/s/cm^2	ΔF_{RMS} erg/s/cm^2	ΔF_{sky} erg/s/cm^2	Upper limit	Good flux
0.0	3.2e-18	1.1e-18	5.4e-17	1.8e-17	6.5e-17	True	False
1.0	6.7e-16	2.2e-16	1.9e-14	6.5e-15	3.0e-16	True	False
2.0	1.2e-17	4.0e-18	2.3e-16	7.7e-17	6.6e-17	True	False
3.0	3.3e-18	1.1e-18	4.7e-17	1.6e-17	6.0e-17	True	False
4.0	7.1e-17	4.1e-18	2.5e-16	7.1e-17	1.1e-16	False	True
5.0	3.3e-18	1.1e-18	4.4e-17	1.5e-17	5.5e-17	True	False
6.0	3.2e-18	1.1e-18	4.4e-17	1.5e-17	5.4e-17	True	False
7.0	3.3e-18	1.1e-18	6.1e-17	2.0e-17	6.6e-17	True	False
8.0	4.5e-17	8.8e-19	1.4e-16	2.8e-17	6.3e-17	False	True
9.0	4.5e-18	1.5e-18	6.8e-17	2.3e-17	1.2e-16	True	False
10.0	4.2e-18	1.4e-18	6.7e-17	2.2e-17	1.1e-16	True	False
11.0	9.7e-18	3.2e-18	2.0e-16	6.5e-17	5.7e-17	True	False
12.0	7.8e-18	2.6e-18	1.6e-16	5.3e-17	6.6e-17	True	False
13.0	4.7e-18	1.6e-18	8.4e-17	2.8e-17	6.6e-17	True	False
14.0	4.1e-18	1.4e-18	8.1e-17	2.7e-17	9.8e-17	True	False
15.0	6.1e-18	2.0e-18	1.4e-16	4.8e-17	5.9e-17	True	False
16.0	4.8e-18	1.6e-18	9.1e-17	3.0e-17	5.6e-17	True	False
17.0	5.7e-18	1.9e-18	1.1e-16	3.8e-17	5.8e-17	True	False
18.0	2.7e-17	9.1e-18	4.8e-16	1.6e-16	5.4e-17	True	False
19.0	4.3e-18	1.4e-18	8.8e-17	2.9e-17	6.2e-17	True	False
20.0	3.1e-18	1.0e-18	4.7e-17	1.6e-17	6.3e-17	True	False
21.0	3.5e-18	1.2e-18	5.1e-17	1.7e-17	5.5e-17	True	False
22.0	7.0e-18	2.3e-18	1.3e-16	4.4e-17	6.7e-17	True	False
23.0	4.6e-18	1.5e-18	7.7e-17	2.6e-17	7.1e-17	True	False
24.0	8.0e-18	2.7e-18	1.5e-16	4.9e-17	6.1e-17	True	False
25.0	8.5e-18	2.8e-18	2.2e-16	7.4e-17	5.9e-17	True	False
26.0	3.3e-18	1.1e-18	4.5e-17	1.5e-17	6.1e-17	True	False
27.0	4.2e-17	1.4e-17	7.3e-16	2.4e-16	6.2e-17	True	False
28.0	1.6e-17	5.2e-18	2.3e-16	7.7e-17	5.4e-17	True	False
29.0	5.6e-17	1.9e-17	8.8e-16	2.9e-16	8.2e-17	True	False
30.0	5.0e-18	1.7e-18	8.4e-17	2.8e-17	6.0e-17	True	False
31.0	2.1e-18	7.2e-19	4.7e-17	1.6e-17	1.1e-16	True	False
32.0	3.1e-18	1.0e-18	5.0e-17	1.7e-17	6.1e-17	True	False
33.0	5.4e-18	1.8e-18	1.0e-16	3.4e-17	5.3e-17	True	False
34.0	2.1e-17	7.0e-18	3.6e-16	1.2e-16	8.7e-17	True	False
35.0	9.4e-18	3.1e-18	1.5e-16	5.0e-17	1.4e-16	True	False
36.0	5.0e-18	1.7e-18	8.4e-17	2.8e-17	6.3e-17	True	False
37.0	3.0e-18	1.0e-18	4.4e-17	1.5e-17	5.6e-17	True	False
38.0	8.9e-18	3.0e-18	1.5e-16	4.9e-17	6.9e-17	True	False
39.0	4.2e-18	1.4e-18	5.8e-17	1.9e-17	1.1e-16	True	False
40.0	3.1e-18	1.0e-18	4.6e-17	1.5e-17	5.5e-17	True	False
41.0	2.8e-18	9.3e-19	4.4e-17	1.5e-17	6.0e-17	True	False
42.0	3.3e-18	1.1e-18	4.5e-17	1.5e-17	6.1e-17	True	False
43.0	6.5e-18	2.2e-18	1.2e-16	4.0e-17	6.6e-17	True	False
44.0	5.4e-18	1.8e-18	1.0e-16	3.4e-17	6.2e-17	True	False
45.0	3.2e-18	1.1e-18	5.2e-17	1.7e-17	5.4e-17	True	False
46.0	1.7e-17	5.8e-18	2.8e-16	9.2e-17	7.3e-17	True	False
47.0	3.1e-18	1.0e-18	6.3e-17	2.1e-17	9.7e-17	True	False
48.0	3.2e-18	1.1e-18	5.2e-17	1.7e-17	5.3e-17	True	False
49.0	5.2e-18	1.7e-18	7.8e-17	2.6e-17	5.9e-17	True	False
50.0	3.4e-18	1.1e-18	4.1e-17	1.4e-17	7.3e-17	True	False
51.0	8.5e-18	2.8e-18	1.8e-16	6.1e-17	1.4e-16	True	False
52.0	6.4e-18	2.1e-18	1.5e-16	4.9e-17	6.7e-17	True	False
53.0	3.0e-18	9.9e-19	4.5e-17	1.5e-17	5.3e-17	True	False
54.0	1.3e-16	4.5e-17	6.4e-15	2.1e-15	1.3e-16	True	False
55.0	1.6e-17	5.3e-18	2.4e-16	7.9e-17	5.8e-17	True	False

56.0	3.6e-18	1.2e-18	5.6e-17	1.9e-17	1.3e-16	True	False
57.0	1.1e-17	3.8e-18	2.2e-16	7.4e-17	6.9e-17	True	False
58.0	4.7e-18	1.6e-18	8.6e-17	2.9e-17	5.6e-17	True	False
59.0	1.4e-17	4.5e-18	2.5e-16	8.4e-17	7.0e-17	True	False
60.0	2.4e-17	8.0e-18	3.8e-16	1.3e-16	5.9e-17	True	False
61.0	3.0e-18	1.0e-18	4.2e-17	1.4e-17	6.2e-17	True	False
62.0	2.0e-17	1.2e-18	5.1e-17	1.4e-17	6.2e-17	False	False
63.0	4.6e-18	1.5e-18	6.9e-17	2.3e-17	7.5e-17	True	False
64.0	3.7e-18	1.2e-18	8.8e-17	2.9e-17	5.7e-17	True	False
65.0	3.9e-18	1.3e-18	5.7e-17	1.9e-17	7.7e-17	True	False
66.0	5.4e-18	1.8e-18	1.1e-16	3.6e-17	1.3e-16	True	False
67.0	1.4e-17	4.8e-18	2.8e-16	9.2e-17	8.1e-17	True	False
68.0	5.1e-18	1.7e-18	1.0e-16	3.4e-17	5.7e-17	True	False
69.0	7.0e-18	2.3e-18	1.6e-16	5.2e-17	6.6e-17	True	False
70.0	9.2e-17	3.1e-17	1.6e-15	5.4e-16	6.5e-17	True	False
71.0	5.5e-15	1.8e-15	9.2e-14	3.1e-14	5.6e-16	True	False
72.0	1.8e-17	5.9e-18	3.7e-16	1.2e-16	6.7e-17	True	False
73.0	1.2e-17	4.0e-18	2.4e-16	7.9e-17	6.7e-17	True	False
74.0	4.0e-18	1.3e-18	7.6e-17	2.5e-17	1.2e-16	True	False
75.0	3.3e-18	1.1e-18	5.0e-17	1.7e-17	6.9e-17	True	False
76.0	8.0e-18	2.7e-18	1.3e-16	4.5e-17	5.5e-17	True	False
77.0	2.3e-18	7.5e-19	5.3e-17	1.8e-17	5.9e-17	True	False
78.0	3.3e-18	1.1e-18	5.3e-17	1.8e-17	5.9e-17	True	False
79.0	3.6e-18	1.2e-18	5.3e-17	1.8e-17	7.7e-17	True	False
80.0	4.5e-18	1.5e-18	6.6e-17	2.2e-17	6.7e-17	True	False
81.0	3.6e-18	1.2e-18	4.6e-17	1.5e-17	6.1e-17	True	False
82.0	3.1e-18	1.0e-18	4.6e-17	1.5e-17	5.4e-17	True	False
83.0	2.9e-18	9.8e-19	5.2e-17	1.7e-17	7.1e-17	True	False
84.0	3.4e-18	1.1e-18	4.7e-17	1.6e-17	8.2e-17	True	False
85.0	3.2e-18	1.1e-18	5.3e-17	1.8e-17	5.6e-17	True	False
86.0	6.7e-17	2.2e-17	1.4e-15	4.6e-16	6.3e-17	True	False
87.0	7.9e-18	2.6e-18	1.3e-16	4.3e-17	8.2e-17	True	False
88.0	2.1e-17	9.8e-19	5.5e-17	1.3e-17	5.8e-17	False	False
89.0	3.1e-18	1.0e-18	5.2e-17	1.7e-17	7.5e-17	True	False
90.0	3.1e-18	1.0e-18	4.8e-17	1.6e-17	7.1e-17	True	False
91.0	1.1e-16	3.7e-17	1.7e-15	5.7e-16	6.4e-17	True	False
92.0	3.6e-18	1.2e-18	5.3e-17	1.8e-17	5.2e-17	True	False
93.0	1.0e-17	3.4e-18	1.7e-16	5.7e-17	5.3e-17	True	False
94.0	3.5e-18	1.2e-18	5.5e-17	1.8e-17	5.7e-17	True	False
95.0	3.0e-18	1.0e-18	4.8e-17	1.6e-17	6.7e-17	True	False
96.0	1.5e-17	5.1e-18	2.4e-16	8.0e-17	5.0e-17	True	False
97.0	3.0e-18	9.9e-19	4.4e-17	1.5e-17	5.3e-17	True	False
98.0	2.9e-18	9.6e-19	5.6e-17	1.9e-17	6.1e-17	True	False
99.0	3.7e-18	1.2e-18	5.2e-17	1.7e-17	5.1e-17	True	False
100.0	4.3e-17	1.4e-17	7.0e-16	2.3e-16	5.1e-17	True	False
101.0	3.0e-18	1.0e-18	5.3e-17	1.8e-17	5.0e-17	True	False
102.0	3.5e-18	1.2e-18	4.4e-17	1.5e-17	5.0e-17	True	False
103.0	3.8e-18	1.3e-18	6.0e-17	2.0e-17	5.7e-17	True	False
104.0	4.6e-18	1.5e-18	6.9e-17	2.3e-17	5.0e-17	True	False
105.0	3.0e-18	9.9e-19	4.1e-17	1.4e-17	5.7e-17	True	False
106.0	5.1e-17	1.7e-17	8.6e-16	2.9e-16	5.5e-17	True	False
107.0	4.8e-18	1.6e-18	8.9e-17	3.0e-17	5.4e-17	True	False
108.0	2.8e-18	9.3e-19	3.9e-17	1.3e-17	5.1e-17	True	False
109.0	3.1e-18	1.0e-18	4.0e-17	1.3e-17	5.3e-17	True	False
110.0	2.6e-18	8.6e-19	4.2e-17	1.4e-17	4.9e-17	True	False
111.0	3.1e-18	1.0e-18	5.8e-17	1.9e-17	5.6e-17	True	False
112.0	4.9e-18	1.6e-18	1.1e-16	3.6e-17	5.7e-17	True	False
113.0	3.1e-18	1.0e-18	4.9e-17	1.6e-17	5.6e-17	True	False
114.0	3.0e-18	9.9e-19	4.2e-17	1.4e-17	5.4e-17	True	False
115.0	3.8e-18	1.3e-18	6.7e-17	2.2e-17	5.3e-17	True	False
116.0	1.3e-17	4.2e-18	2.1e-16	7.1e-17	5.1e-17	True	False
117.0	3.6e-18	1.2e-18	5.9e-17	2.0e-17	5.2e-17	True	False

118.0	2.6e-18	8.6e-19	4.3e-17	1.4e-17	5.5e-17	True	False
119.0	2.7e-18	8.9e-19	5.6e-17	1.9e-17	5.8e-17	True	False
120.0	1.2e-17	3.8e-18	2.0e-16	6.6e-17	4.9e-17	True	False
121.0	3.1e-18	1.0e-18	4.0e-17	1.3e-17	5.4e-17	True	False
122.0	3.9e-18	1.3e-18	1.3e-16	4.2e-17	6.1e-17	True	False
123.0	2.9e-18	9.5e-19	5.9e-17	2.0e-17	7.5e-17	True	False
124.0	2.3e-17	7.8e-18	3.5e-16	1.2e-16	5.7e-17	True	False
125.0	1.0e-17	3.5e-18	2.1e-16	7.1e-17	4.7e-17	True	False
126.0	7.0e-18	2.3e-18	1.7e-16	5.8e-17	5.7e-17	True	False
127.0	3.5e-18	1.2e-18	7.4e-17	2.5e-17	5.6e-17	True	False
128.0	3.2e-18	1.1e-18	4.1e-17	1.4e-17	5.0e-17	True	False
129.0	3.5e-18	1.2e-18	4.5e-17	1.5e-17	6.0e-17	True	False
130.0	8.7e-18	2.9e-18	1.4e-16	4.6e-17	5.4e-17	True	False
131.0	3.7e-18	1.2e-18	5.1e-17	1.7e-17	4.8e-17	True	False
132.0	2.7e-18	9.1e-19	4.5e-17	1.5e-17	5.8e-17	True	False
133.0	2.3e-17	7.5e-18	3.5e-16	1.2e-16	5.0e-17	True	False
134.0	1.4e-17	4.8e-18	2.8e-16	9.4e-17	5.1e-17	True	False
135.0	3.1e-18	1.0e-18	4.6e-17	1.5e-17	5.1e-17	True	False
136.0	4.8e-18	1.6e-18	9.7e-17	3.2e-17	5.0e-17	True	False
137.0	1.4e-17	4.7e-18	2.1e-16	6.9e-17	5.7e-17	True	False
138.0	2.9e-18	9.6e-19	4.8e-17	1.6e-17	7.0e-17	True	False
139.0	4.5e-18	1.5e-18	7.0e-17	2.3e-17	6.1e-17	True	False
140.0	2.8e-18	9.2e-19	5.7e-17	1.9e-17	6.1e-17	True	False
141.0	4.0e-18	1.3e-18	6.0e-17	2.0e-17	6.1e-17	True	False

OI 8446$\mathring{A}$

Star ID	*f(peak)* erg/Å/s/cm^2	Line peak RMS erg/Å/s/cm^2	F erg/s/cm^2	ΔF_{RMS} erg/s/cm^2	ΔF_{sky} erg/s/cm^2	Upper limit	Good flux
0.0	2.3e-18	7.5e-19	8.1e-17	2.7e-17	7.5e-17	True	False
1.0	3.6e-16	1.2e-16	1.3e-14	4.5e-15	2.5e-16	True	False
2.0	9.7e-18	3.2e-18	1.0e-15	3.3e-16	8.0e-17	True	False
3.0	3.2e-18	1.1e-18	1.1e-16	3.5e-17	7.3e-17	True	False
4.0	1.9e-17	6.5e-18	5.1e-15	1.7e-15	1.2e-16	True	False
5.0	2.6e-18	8.8e-19	8.9e-17	3.0e-17	7.1e-17	True	False
6.0	2.6e-18	8.7e-19	7.8e-17	2.6e-17	6.2e-17	True	False
7.0	4.2e-18	1.4e-18	1.4e-16	4.5e-17	7.4e-17	True	False
8.0	2.1e-18	7.1e-19	1.5e-16	4.9e-17	6.8e-17	True	False
9.0	5.3e-18	1.8e-18	2.0e-16	6.8e-17	1.4e-16	True	False
10.0	4.2e-18	1.4e-18	1.6e-16	5.3e-17	1.2e-16	True	False
11.0	6.0e-18	2.0e-18	3.0e-16	1.0e-16	7.3e-17	True	False
12.0	1.3e-17	4.2e-18	4.7e-16	1.6e-16	8.4e-17	True	False
13.0	6.8e-18	2.3e-18	4.1e-16	1.4e-16	7.6e-17	True	False
14.0	3.1e-18	1.0e-18	1.6e-16	5.3e-17	9.8e-17	True	False
15.0	8.6e-18	2.9e-18	2.9e-16	9.8e-17	6.7e-17	True	False
16.0	4.9e-18	1.6e-18	1.8e-16	5.9e-17	7.7e-17	True	False
17.0	6.9e-18	2.3e-18	2.2e-16	7.5e-17	7.1e-17	True	False
18.0	2.4e-17	8.1e-18	8.6e-16	2.9e-16	6.6e-17	True	False
19.0	5.6e-18	1.9e-18	1.7e-16	5.7e-17	7.3e-17	True	False
20.0	4.0e-18	1.3e-18	1.2e-16	4.0e-17	1.1e-16	True	False
21.0	2.9e-18	9.7e-19	1.4e-16	4.6e-17	6.5e-17	True	False
22.0	6.8e-18	2.3e-18	2.3e-16	7.8e-17	1.3e-16	True	False
23.0	4.8e-18	1.6e-18	1.4e-16	4.6e-17	1.2e-16	True	False
24.0	8.4e-18	2.8e-18	3.7e-16	1.2e-16	7.1e-17	True	False
25.0	7.3e-18	2.4e-18	3.6e-16	1.2e-16	5.8e-17	True	False
26.0	4.7e-18	1.6e-18	1.9e-16	6.5e-17	7.1e-17	True	False
27.0	2.6e-17	8.8e-18	1.7e-15	5.8e-16	7.7e-17	True	False
28.0	9.3e-18	3.1e-18	4.5e-16	1.5e-16	6.1e-17	True	False
29.0	2.7e-17	9.1e-18	2.3e-15	7.7e-16	1.7e-16	True	False
30.0	3.5e-18	1.2e-18	2.2e-16	7.3e-17	7.2e-17	True	False
31.0	6.1e-18	2.0e-18	2.6e-16	8.5e-17	1.8e-16	True	False
32.0	3.3e-18	1.1e-18	1.2e-16	4.1e-17	6.9e-17	True	False
33.0	3.8e-18	1.3e-18	1.4e-16	4.8e-17	6.2e-17	True	False
34.0	1.4e-17	4.7e-18	8.6e-16	2.9e-16	1.4e-16	True	False
35.0	6.1e-18	2.0e-18	3.7e-16	1.2e-16	2.8e-16	True	False
36.0	5.6e-18	1.9e-18	1.9e-16	6.2e-17	8.6e-17	True	False
37.0	2.7e-18	8.9e-19	1.1e-16	3.6e-17	7.0e-17	True	False
38.0	6.1e-18	2.0e-18	3.6e-16	1.2e-16	1.0e-16	True	False
39.0	4.6e-18	1.5e-18	1.5e-16	5.2e-17	2.0e-16	True	False
40.0	2.2e-18	7.4e-19	1.1e-16	3.5e-17	7.0e-17	True	False
41.0	2.8e-18	9.3e-19	1.5e-16	5.0e-17	7.5e-17	True	False
42.0	2.5e-18	8.3e-19	9.6e-17	3.2e-17	8.1e-17	True	False
43.0	5.2e-18	1.7e-18	2.4e-16	7.9e-17	9.3e-17	True	False
44.0	4.7e-18	1.6e-18	2.2e-16	7.3e-17	7.1e-17	True	False
45.0	2.3e-18	7.6e-19	8.1e-17	2.7e-17	6.6e-17	True	False
46.0	8.2e-18	2.7e-18	5.9e-16	2.0e-16	1.0e-16	True	False
47.0	3.9e-18	1.3e-18	1.4e-16	4.6e-17	1.2e-16	True	False
48.0	3.1e-18	1.0e-18	1.1e-16	3.6e-17	6.2e-17	True	False
49.0	7.2e-18	2.4e-18	2.8e-16	9.2e-17	8.9e-17	True	False
50.0	2.5e-18	8.4e-19	1.1e-16	3.7e-17	1.1e-16	True	False
51.0	9.0e-18	3.0e-18	4.5e-16	1.5e-16	2.3e-16	True	False
52.0	9.9e-18	3.3e-18	3.9e-16	1.3e-16	8.3e-17	True	False
53.0	3.0e-18	1.0e-18	1.1e-16	3.6e-17	6.7e-17	True	False
54.0	1.9e-16	6.2e-17	7.0e-15	2.3e-15	1.3e-16	True	False
55.0	1.5e-17	5.1e-18	6.2e-16	2.1e-16	7.3e-17	True	False

56.0	5.8e-18	1.9e-18	2.3e-16	7.5e-17	1.9e-16	True	False
57.0	1.3e-17	4.3e-18	5.0e-16	1.7e-16	8.5e-17	True	False
58.0	5.7e-18	1.9e-18	2.1e-16	7.0e-17	7.0e-17	True	False
59.0	7.8e-18	2.6e-18	4.0e-16	1.3e-16	8.6e-17	True	False
60.0	1.7e-17	5.8e-18	9.5e-16	3.2e-16	6.5e-17	True	False
61.0	3.3e-18	1.1e-18	1.4e-16	4.6e-17	1.0e-16	True	False
62.0	2.7e-18	8.9e-19	7.0e-17	2.3e-17	6.9e-17	True	False
63.0	4.5e-18	1.5e-18	1.5e-16	5.2e-17	7.3e-17	True	False
64.0	4.1e-18	1.4e-18	8.0e-16	2.7e-16	7.0e-17	True	False
65.0	6.0e-18	2.0e-18	2.5e-16	8.3e-17	1.1e-16	True	False
66.0	6.2e-18	2.1e-18	2.3e-16	7.5e-17	2.2e-16	True	False
67.0	1.5e-17	5.1e-18	5.4e-16	1.8e-16	1.2e-16	True	False
68.0	6.3e-18	2.1e-18	2.0e-16	6.5e-17	7.0e-17	True	False
69.0	7.6e-18	2.5e-18	2.6e-16	8.7e-17	9.6e-17	True	False
70.0	5.9e-17	2.0e-17	3.6e-15	1.2e-15	8.4e-17	True	False
71.0	2.8e-15	9.3e-16	1.1e-13	3.7e-14	8.5e-16	True	False
72.0	1.5e-17	5.1e-18	6.4e-16	2.1e-16	9.9e-17	True	False
73.0	7.2e-18	2.4e-18	3.8e-16	1.3e-16	8.4e-17	True	False
74.0	5.9e-18	2.0e-18	2.4e-16	8.1e-17	1.4e-16	True	False
75.0	3.8e-18	1.3e-18	1.3e-16	4.4e-17	7.9e-17	True	False
76.0	1.0e-17	3.3e-18	5.0e-16	1.7e-16	6.7e-17	True	False
77.0	2.9e-18	9.6e-19	1.1e-16	3.7e-17	6.2e-17	True	False
78.0	3.5e-18	1.2e-18	1.2e-16	4.1e-17	6.4e-17	True	False
79.0	1.9e-18	6.2e-19	7.1e-17	2.4e-17	9.3e-17	True	False
80.0	4.1e-18	1.4e-18	1.6e-16	5.3e-17	8.0e-17	True	False
81.0	2.9e-18	9.5e-19	1.1e-16	3.6e-17	6.8e-17	True	False
82.0	2.6e-18	8.5e-19	7.6e-17	2.5e-17	5.6e-17	True	False
83.0	6.7e-18	2.2e-18	3.1e-16	1.0e-16	8.7e-17	True	False
84.0	5.3e-18	1.8e-18	2.2e-16	7.3e-17	8.5e-17	True	False
85.0	2.4e-18	8.0e-19	9.6e-17	3.2e-17	6.2e-17	True	False
86.0	3.0e-17	9.8e-18	1.8e-15	5.8e-16	8.6e-17	True	False
87.0	7.0e-18	2.3e-18	2.9e-16	9.7e-17	9.8e-17	True	False
88.0	2.6e-18	8.7e-19	5.8e-16	1.9e-16	8.0e-17	True	False
89.0	3.4e-18	1.1e-18	1.5e-16	5.1e-17	9.3e-17	True	False
90.0	3.6e-18	1.2e-18	1.4e-16	4.6e-17	8.9e-17	True	False
91.0	7.1e-17	2.4e-17	4.5e-15	1.5e-15	8.0e-17	True	False
92.0	4.0e-18	1.3e-18	1.4e-16	4.5e-17	5.8e-17	True	False
93.0	6.3e-18	2.1e-18	3.2e-15	1.1e-15	5.8e-17	True	False
94.0	3.2e-18	1.1e-18	1.0e-16	3.3e-17	5.9e-17	True	False
95.0	2.6e-18	8.7e-19	8.7e-17	2.9e-17	7.6e-17	True	False
96.0	1.1e-17	3.6e-18	5.9e-16	2.0e-16	5.6e-17	True	False
97.0	2.1e-18	7.1e-19	7.0e-17	2.3e-17	6.6e-17	True	False
98.0	2.9e-18	9.5e-19	1.1e-16	3.7e-17	8.3e-17	True	False
99.0	3.6e-18	1.2e-18	2.6e-16	8.8e-17	5.8e-17	True	False
100.0	2.6e-17	8.5e-18	2.5e-15	8.4e-16	7.1e-17	True	False
101.0	2.7e-18	8.9e-19	8.4e-17	2.8e-17	6.0e-17	True	False
102.0	2.3e-18	7.5e-19	7.1e-17	2.4e-17	5.9e-17	True	False
103.0	3.7e-18	1.2e-18	1.3e-16	4.2e-17	6.5e-17	True	False
104.0	5.6e-18	1.9e-18	2.0e-16	6.8e-17	6.0e-17	True	False
105.0	2.3e-18	7.6e-19	9.8e-17	3.3e-17	7.4e-17	True	False
106.0	2.9e-17	9.6e-18	4.6e-15	1.5e-15	6.5e-17	True	False
107.0	4.8e-18	1.6e-18	1.5e-16	5.1e-17	5.8e-17	True	False
108.0	2.4e-18	7.8e-19	8.1e-17	2.7e-17	5.5e-17	True	False
109.0	2.6e-18	8.8e-19	8.3e-17	2.8e-17	6.8e-17	True	False
110.0	2.6e-18	8.7e-19	8.7e-17	2.9e-17	6.3e-17	True	False
111.0	4.4e-18	1.5e-18	1.4e-16	4.8e-17	6.7e-17	True	False
112.0	5.1e-18	1.7e-18	2.3e-16	7.6e-17	7.0e-17	True	False
113.0	4.0e-18	1.3e-18	2.0e-16	6.5e-17	7.7e-17	True	False
114.0	2.2e-18	7.2e-19	7.0e-17	2.3e-17	6.9e-17	True	False
115.0	4.2e-18	1.4e-18	1.4e-16	4.7e-17	5.7e-17	True	False
116.0	7.1e-18	2.4e-18	5.6e-16	1.9e-16	6.2e-17	True	False
117.0	3.6e-18	1.2e-18	1.3e-16	4.4e-17	7.6e-17	True	False

118.0	2.3e-18	7.6e-19	9.3e-17	3.1e-17	6.4e-17	True	False
119.0	2.1e-18	7.1e-19	8.8e-17	2.9e-17	7.9e-17	True	False
120.0	6.4e-18	2.1e-18	3.9e-16	1.3e-16	5.5e-17	True	False
121.0	2.3e-18	7.7e-19	1.1e-16	3.6e-17	6.0e-17	True	False
122.0	4.8e-18	1.6e-18	2.1e-16	7.0e-17	7.3e-17	True	False
123.0	3.5e-18	1.2e-18	1.1e-16	3.6e-17	9.8e-17	True	False
124.0	1.1e-17	3.6e-18	9.0e-16	3.0e-16	7.7e-17	True	False
125.0	5.8e-18	1.9e-18	3.4e-16	1.1e-16	5.8e-17	True	False
126.0	5.9e-18	2.0e-18	2.5e-16	8.2e-17	7.1e-17	True	False
127.0	4.3e-18	1.4e-18	1.5e-16	5.0e-17	5.8e-17	True	False
128.0	3.1e-18	1.0e-18	1.4e-16	4.8e-17	5.8e-17	True	False
129.0	5.0e-18	1.7e-18	2.2e-16	7.3e-17	6.1e-17	True	False
130.0	5.6e-18	1.9e-18	2.4e-16	7.8e-17	5.9e-17	True	False
131.0	2.5e-18	8.5e-19	8.9e-17	3.0e-17	5.4e-17	True	False
132.0	2.5e-18	8.2e-19	1.0e-16	3.3e-17	6.5e-17	True	False
133.0	1.4e-17	4.8e-18	9.4e-16	3.1e-16	5.5e-17	True	False
134.0	1.2e-17	4.0e-18	6.4e-16	2.1e-16	6.3e-17	True	False
135.0	2.9e-18	9.5e-19	1.3e-16	4.4e-17	5.8e-17	True	False
136.0	6.3e-18	2.1e-18	2.1e-16	7.0e-17	5.6e-17	True	False
137.0	8.0e-18	2.7e-18	9.0e-16	3.0e-16	5.7e-17	True	False
138.0	2.5e-18	8.4e-19	7.7e-17	2.6e-17	7.6e-17	True	False
139.0	4.4e-18	1.5e-18	7.1e-16	2.4e-16	6.9e-17	True	False
140.0	2.4e-18	7.9e-19	9.1e-17	3.0e-17	6.6e-17	True	False
141.0	2.3e-18	7.8e-19	1.3e-16	4.5e-17	6.6e-17	True	False

HeI 5876$\mathring{A}$

Star ID	*f(peak)* erg/Å/s/cm^2	Line peak RMS erg/Å/s/cm^2	F erg/s/cm^2	ΔF_{RMS} erg/s/cm^2	ΔF_{sky} erg/s/cm^2	Upper limit	Good flux
0.0	4.1e-18	1.4e-18	9.0e-17	3.0e-17	2.7e-16	True	False
1.0	4.5e-17	1.5e-17	8.0e-14	2.7e-14	6.6e-16	True	False
2.0	1.4e-17	4.8e-18	1.0e-15	3.4e-16	3.2e-16	True	False
3.0	3.6e-18	1.2e-18	9.5e-17	3.2e-17	2.5e-16	True	False
4.0	1.0e-17	3.5e-18	6.0e-16	2.0e-16	5.4e-16	True	False
5.0	4.2e-18	1.4e-18	9.3e-17	3.1e-17	3.0e-16	True	False
6.0	4.3e-17	1.3e-18	1.8e-16	2.7e-17	2.8e-16	False	False
7.0	8.6e-17	1.2e-18	1.8e-16	3.0e-17	2.6e-16	False	False
8.0	6.9e-17	1.4e-18	2.6e-16	3.1e-17	2.6e-16	False	False
9.0	5.2e-18	1.7e-18	1.6e-16	5.5e-17	4.5e-16	True	False
10.0	4.1e-18	1.4e-18	1.4e-16	4.7e-17	4.5e-16	True	False
11.0	6.6e-18	2.2e-18	3.3e-16	1.1e-16	2.7e-16	True	False
12.0	6.3e-18	2.1e-18	1.9e-16	6.4e-17	2.9e-16	True	False
13.0	6.4e-17	1.4e-18	1.2e-16	3.1e-17	3.1e-16	False	False
14.0	4.5e-18	1.5e-18	1.6e-16	5.5e-17	3.9e-16	True	False
15.0	6.2e-18	2.1e-18	1.8e-16	6.1e-17	2.5e-16	True	False
16.0	3.9e-18	1.3e-18	1.2e-16	4.0e-17	3.0e-16	True	False
17.0	8.7e-17	1.7e-18	2.4e-16	5.1e-17	2.6e-16	False	False
18.0	1.7e-17	5.6e-18	1.1e-15	3.7e-16	3.0e-16	True	False
19.0	4.0e-18	1.3e-18	1.4e-16	4.6e-17	3.1e-16	True	False
20.0	3.6e-18	1.2e-18	8.9e-17	3.0e-17	3.2e-16	True	False
21.0	3.7e-18	1.2e-18	8.0e-17	2.7e-17	2.6e-16	True	False
22.0	3.6e-18	1.2e-18	1.5e-16	5.1e-17	3.0e-16	True	False
23.0	4.9e-18	1.6e-18	1.1e-16	3.6e-17	2.9e-16	True	False
24.0	5.4e-18	1.8e-18	1.6e-16	5.2e-17	3.1e-16	True	False
25.0	6.6e-18	2.2e-18	3.1e-16	1.0e-16	2.2e-16	True	False
26.0	4.1e-18	1.4e-18	1.0e-16	3.3e-17	3.3e-16	True	False
27.0	3.4e-17	1.1e-17	2.6e-15	8.8e-16	2.8e-16	True	False
28.0	9.0e-18	3.0e-18	5.9e-16	2.0e-16	2.4e-16	True	False
29.0	4.2e-17	1.4e-17	3.1e-15	1.0e-15	3.6e-16	True	False
30.0	4.7e-18	1.6e-18	2.8e-16	9.2e-17	3.3e-16	True	False
31.0	3.2e-17	1.7e-18	1.1e-16	3.6e-17	4.4e-16	False	False
32.0	3.5e-18	1.2e-18	8.0e-17	2.7e-17	3.1e-16	True	False
33.0	4.8e-18	1.6e-18	1.4e-16	4.5e-17	2.6e-16	True	False
34.0	1.5e-17	5.1e-18	1.1e-15	3.6e-16	4.2e-16	True	False
35.0	7.6e-18	2.5e-18	4.9e-16	1.6e-16	5.0e-16	True	False
36.0	4.1e-18	1.4e-18	1.4e-16	4.8e-17	3.6e-16	True	False
37.0	3.4e-18	1.1e-18	9.4e-17	3.1e-17	2.9e-16	True	False
38.0	7.5e-18	2.5e-18	5.1e-16	1.7e-16	3.6e-16	True	False
39.0	3.7e-18	1.2e-18	9.9e-17	3.3e-17	3.7e-16	True	False
40.0	4.8e-17	1.0e-18	2.0e-16	2.9e-17	2.8e-16	False	False
41.0	3.5e-18	1.2e-18	8.0e-17	2.7e-17	3.4e-16	True	False
42.0	3.2e-18	1.1e-18	8.3e-17	2.8e-17	2.9e-16	True	False
43.0	5.8e-18	1.9e-18	1.9e-16	6.5e-17	4.3e-16	True	False
44.0	5.2e-18	1.7e-18	2.0e-16	6.6e-17	2.5e-16	True	False
45.0	1.2e-16	1.1e-18	2.2e-16	2.7e-17	3.2e-16	False	False
46.0	9.2e-18	3.1e-18	7.6e-16	2.5e-16	2.9e-16	True	False
47.0	2.6e-18	8.8e-19	9.7e-17	3.2e-17	3.9e-16	True	False
48.0	7.9e-17	1.3e-18	1.8e-16	2.9e-17	2.4e-16	False	False
49.0	4.3e-18	1.4e-18	1.1e-16	3.8e-17	5.8e-16	True	False
50.0	3.6e-18	1.2e-18	8.3e-17	2.8e-17	5.2e-16	True	False
51.0	7.3e-18	2.4e-18	2.3e-16	7.6e-17	3.4e-16	True	False
52.0	6.2e-18	2.1e-18	2.1e-16	7.0e-17	2.2e-16	True	False
53.0	3.7e-18	1.2e-18	8.9e-17	3.0e-17	2.5e-16	True	False
54.0	1.7e-16	5.6e-17	3.2e-14	1.1e-14	3.7e-16	True	False
55.0	1.1e-17	3.6e-18	7.0e-16	2.3e-16	4.6e-16	True	False

56.0	3.8e-18	1.3e-18	1.1e-16	3.5e-17	3.6e-16	True	False
57.0	1.3e-17	4.3e-18	7.0e-16	2.3e-16	2.7e-16	True	False
58.0	1.2e-16	1.2e-18	3.9e-16	3.6e-17	4.4e-16	False	False
59.0	7.8e-18	2.6e-18	4.8e-16	1.6e-16	3.7e-16	True	False
60.0	1.6e-17	5.4e-18	1.2e-15	3.9e-16	2.6e-16	True	False
61.0	6.7e-17	1.3e-18	1.8e-16	3.1e-17	2.7e-16	False	False
62.0	3.7e-18	1.2e-18	7.9e-17	2.6e-17	3.0e-16	True	False
63.0	4.9e-18	1.6e-18	1.3e-16	4.4e-17	3.8e-16	True	False
64.0	1.7e-16	1.5e-18	4.5e-16	3.3e-17	3.6e-16	False	False
65.0	4.2e-18	1.4e-18	1.0e-16	3.4e-17	3.9e-16	True	False
66.0	4.6e-18	1.5e-18	1.2e-16	4.0e-17	5.1e-16	True	False
67.0	9.7e-18	3.2e-18	5.1e-16	1.7e-16	3.8e-16	True	False
68.0	4.3e-18	1.4e-18	1.6e-16	5.3e-17	3.3e-16	True	False
69.0	6.0e-18	2.0e-18	2.1e-16	6.8e-17	3.5e-16	True	False
70.0	5.1e-17	1.7e-17	5.2e-15	1.7e-15	4.0e-16	True	False
71.0	2.2e-15	7.5e-16	9.2e-14	3.1e-14	1.3e-15	True	False
72.0	1.2e-17	4.0e-18	6.8e-16	2.3e-16	4.7e-16	True	False
73.0	6.6e-18	2.2e-18	4.9e-16	1.6e-16	3.2e-16	True	False
74.0	4.5e-18	1.5e-18	1.5e-16	5.0e-17	4.1e-16	True	False
75.0	3.6e-18	1.2e-18	1.0e-16	3.5e-17	3.1e-16	True	False
76.0	7.4e-17	1.8e-18	1.7e-16	5.6e-17	2.8e-16	False	False
77.0	2.7e-18	9.0e-19	8.0e-17	2.7e-17	2.6e-16	True	False
78.0	4.1e-18	1.4e-18	9.0e-17	3.0e-17	3.0e-16	True	False
79.0	6.9e-17	1.2e-18	1.6e-16	3.2e-17	3.6e-16	False	False
80.0	5.6e-18	1.9e-18	1.3e-16	4.4e-17	3.0e-16	True	False
81.0	3.9e-18	1.3e-18	8.4e-17	2.8e-17	3.2e-16	True	False
82.0	4.2e-18	1.4e-18	8.8e-17	2.9e-17	2.5e-16	True	False
83.0	4.1e-18	1.4e-18	8.9e-17	3.0e-17	2.0e-16	True	False
84.0	6.3e-17	1.4e-18	1.3e-16	3.0e-17	2.7e-16	False	False
85.0	8.0e-17	1.1e-18	2.3e-16	2.7e-17	2.9e-16	False	False
86.0	4.3e-17	1.4e-17	2.6e-15	8.6e-16	1.8e-16	True	False
87.0	5.4e-18	1.8e-18	2.7e-16	9.1e-17	2.1e-16	True	False
88.0	3.4e-18	1.1e-18	8.6e-17	2.9e-17	2.6e-16	True	False
89.0	3.6e-18	1.2e-18	9.3e-17	3.1e-17	2.1e-16	True	False
90.0	4.3e-18	1.4e-18	1.2e-16	4.1e-17	3.1e-16	True	False
91.0	9.0e-17	3.0e-17	6.2e-15	2.1e-15	2.6e-16	True	False
92.0	3.6e-18	1.2e-18	8.2e-17	2.7e-17	1.8e-16	True	False
93.0	5.6e-18	1.9e-18	4.1e-16	1.4e-16	1.9e-16	True	False
94.0	3.3e-18	1.1e-18	8.4e-17	2.8e-17	3.2e-16	True	False
95.0	3.4e-17	1.3e-18	1.0e-16	2.9e-17	2.3e-16	False	False
96.0	1.1e-17	3.6e-18	7.8e-16	2.6e-16	2.1e-16	True	False
97.0	2.5e-18	8.4e-19	8.0e-17	2.7e-17	1.7e-16	True	False
98.0	3.7e-18	1.2e-18	8.2e-17	2.7e-17	3.6e-16	True	False
99.0	3.3e-18	1.1e-18	8.1e-17	2.7e-17	1.4e-16	True	False
100.0	4.2e-17	1.4e-17	2.7e-15	9.1e-16	3.7e-16	True	False
101.0	4.1e-18	1.4e-18	8.7e-17	2.9e-17	3.3e-16	True	False
102.0	3.3e-18	1.1e-18	8.3e-17	2.8e-17	1.9e-16	True	False
103.0	3.7e-18	1.2e-18	9.3e-17	3.1e-17	2.1e-16	True	False
104.0	3.8e-18	1.3e-18	1.1e-16	3.6e-17	1.4e-16	True	False
105.0	4.1e-18	1.4e-18	9.2e-17	3.1e-17	1.8e-16	True	False
106.0	5.9e-17	2.0e-17	4.3e-15	1.4e-15	1.9e-16	True	False
107.0	1.1e-16	1.4e-18	2.3e-16	5.0e-17	2.4e-16	False	False
108.0	3.6e-17	1.1e-18	8.5e-17	2.5e-17	2.1e-16	False	False
109.0	3.7e-17	1.2e-18	1.1e-16	2.8e-17	3.3e-16	False	False
110.0	5.7e-17	1.0e-18	2.1e-16	2.7e-17	3.3e-16	False	False
111.0	3.0e-18	9.9e-19	8.5e-17	2.8e-17	3.3e-16	True	False
112.0	1.2e-16	1.6e-18	3.0e-16	4.6e-17	4.1e-16	False	False
113.0	3.5e-18	1.2e-18	1.0e-16	3.3e-17	3.2e-16	True	False
114.0	4.0e-18	1.3e-18	9.1e-17	3.0e-17	1.9e-16	True	False
115.0	2.2e-18	7.4e-19	1.0e-16	3.4e-17	1.8e-16	True	False
116.0	9.5e-18	3.2e-18	6.9e-16	2.3e-16	2.9e-16	True	False
117.0	4.1e-18	1.4e-18	1.1e-16	3.5e-17	2.4e-16	True	False

118.0	3.5e-18	1.2e-18	7.1e-17	2.4e-17	1.7e-16	True	False
119.0	1.4e-16	1.4e-18	2.9e-16	3.3e-17	4.7e-16	False	False
120.0	5.9e-18	2.0e-18	3.8e-16	1.3e-16	1.8e-16	True	False
121.0	4.5e-18	1.5e-18	9.1e-17	3.0e-17	1.8e-16	True	False
122.0	2.3e-16	1.6e-18	5.8e-16	6.1e-17	3.9e-16	False	False
123.0	9.9e-17	1.4e-18	1.4e-16	3.1e-17	4.0e-16	False	False
124.0	1.2e-17	4.0e-18	1.1e-15	3.7e-16	4.4e-16	True	False
125.0	8.0e-18	2.7e-18	4.3e-16	1.4e-16	2.0e-16	True	False
126.0	1.3e-16	1.5e-18	3.8e-16	6.3e-17	3.6e-16	False	False
127.0	4.1e-18	1.4e-18	1.1e-16	3.7e-17	2.2e-16	True	False
128.0	3.2e-17	1.1e-18	8.2e-17	2.7e-17	2.2e-16	False	False
129.0	3.9e-18	1.3e-18	9.1e-17	3.0e-17	2.7e-16	True	False
130.0	5.5e-18	1.8e-18	2.6e-16	8.6e-17	1.8e-16	True	False
131.0	4.2e-18	1.4e-18	9.1e-17	3.0e-17	2.0e-16	True	False
132.0	2.9e-18	9.7e-19	8.7e-17	2.9e-17	3.9e-16	True	False
133.0	1.5e-17	5.1e-18	1.0e-15	3.3e-16	1.8e-16	True	False
134.0	7.5e-18	2.5e-18	9.2e-16	3.1e-16	2.5e-16	True	False
135.0	4.4e-18	1.5e-18	8.8e-17	2.9e-17	2.6e-16	True	False
136.0	4.5e-18	1.5e-18	1.3e-16	4.3e-17	1.7e-16	True	False
137.0	1.1e-17	3.8e-18	7.2e-16	2.4e-16	2.0e-16	True	False
138.0	1.0e-16	1.4e-18	2.5e-16	3.1e-17	2.9e-16	False	False
139.0	6.2e-17	1.7e-18	1.8e-16	4.2e-17	2.4e-16	False	False
140.0	8.3e-17	1.5e-18	2.1e-16	3.3e-17	4.3e-16	False	False
141.0	4.3e-17	1.7e-18	1.7e-16	4.7e-17	2.7e-16	False	False

HeI 6678$\mathring{A}$

Star ID	*f(peak)* erg/Å/s/cm^2	Line peak RMS erg/Å/s/cm^2	F erg/s/cm^2	ΔF_{RMS} erg/s/cm^2	ΔF_{sky} erg/s/cm^2	Upper limit	Good flux
0.0	2.8e-18	9.5e-19	7.6e-16	2.5e-16	1.0e-16	True	False
1.0	5.8e-16	1.9e-16	1.7e-14	5.6e-15	4.4e-16	True	False
2.0	8.4e-18	2.8e-18	5.3e-16	1.8e-16	1.4e-16	True	False
3.0	2.9e-18	9.6e-19	9.5e-16	3.2e-16	1.1e-16	True	False
4.0	7.4e-18	2.5e-18	1.4e-15	4.8e-16	2.2e-16	True	False
5.0	2.7e-18	9.1e-19	7.8e-16	2.6e-16	1.3e-16	True	False
6.0	2.5e-18	8.5e-19	7.2e-16	2.4e-16	1.2e-16	True	False
7.0	3.4e-18	1.1e-18	1.3e-15	4.4e-16	1.2e-16	True	False
8.0	2.5e-18	8.2e-19	1.6e-15	5.4e-16	1.1e-16	True	False
9.0	5.0e-18	1.7e-18	9.9e-16	3.3e-16	2.2e-16	True	False
10.0	5.0e-18	1.7e-18	3.8e-16	1.3e-16	2.2e-16	True	False
11.0	6.9e-18	2.3e-18	9.8e-16	3.3e-16	1.2e-16	True	False
12.0	8.3e-18	2.8e-18	2.9e-16	9.5e-17	1.4e-16	True	False
13.0	3.2e-18	1.1e-18	4.6e-16	1.5e-16	1.4e-16	True	False
14.0	2.9e-18	9.7e-19	3.0e-15	9.9e-16	1.9e-16	True	False
15.0	7.1e-18	2.4e-18	4.3e-16	1.4e-16	1.2e-16	True	False
16.0	3.9e-18	1.3e-18	5.5e-16	1.8e-16	1.3e-16	True	False
17.0	4.0e-18	1.3e-18	2.3e-15	7.7e-16	1.1e-16	True	False
18.0	1.0e-17	3.5e-18	1.2e-15	4.0e-16	1.2e-16	True	False
19.0	3.9e-18	1.3e-18	1.0e-15	3.4e-16	1.2e-16	True	False
20.0	3.0e-18	9.9e-19	5.4e-16	1.8e-16	1.4e-16	True	False
21.0	2.8e-18	9.4e-19	9.0e-16	3.0e-16	1.1e-16	True	False
22.0	4.6e-18	1.5e-18	6.2e-16	2.1e-16	1.5e-16	True	False
23.0	3.8e-18	1.3e-18	5.3e-16	1.8e-16	1.4e-16	True	False
24.0	5.7e-18	1.9e-18	6.0e-16	2.0e-16	1.3e-16	True	False
25.0	6.4e-18	2.1e-18	2.4e-15	7.9e-16	9.6e-17	True	False
26.0	2.9e-18	9.6e-19	2.6e-16	8.7e-17	1.3e-16	True	False
27.0	3.2e-17	1.1e-17	1.4e-15	4.6e-16	1.2e-16	True	False
28.0	7.0e-18	2.3e-18	8.0e-16	2.7e-16	1.0e-16	True	False
29.0	2.5e-17	8.5e-18	1.1e-15	3.7e-16	2.0e-16	True	False
30.0	3.8e-18	1.3e-18	1.2e-15	3.9e-16	1.4e-16	True	False
31.0	3.4e-18	1.1e-18	9.8e-16	3.3e-16	2.4e-16	True	False
32.0	3.3e-18	1.1e-18	1.6e-15	5.4e-16	1.2e-16	True	False
33.0	4.1e-18	1.4e-18	5.2e-16	1.7e-16	1.1e-16	True	False
34.0	1.1e-17	3.7e-18	8.0e-16	2.7e-16	2.0e-16	True	False
35.0	6.1e-18	2.0e-18	7.3e-16	2.4e-16	3.0e-16	True	False
36.0	4.2e-18	1.4e-18	2.0e-15	6.8e-16	1.5e-16	True	False
37.0	2.6e-18	8.6e-19	1.6e-15	5.2e-16	1.1e-16	True	False
38.0	5.1e-18	1.7e-18	6.1e-16	2.0e-16	1.7e-16	True	False
39.0	3.4e-18	1.1e-18	7.7e-16	2.6e-16	2.2e-16	True	False
40.0	3.2e-18	1.1e-18	1.8e-15	5.9e-16	1.2e-16	True	False
41.0	3.0e-18	1.0e-18	1.7e-15	5.6e-16	1.5e-16	True	False
42.0	2.0e-18	6.8e-19	8.7e-16	2.9e-16	1.3e-16	True	False
43.0	4.0e-18	1.3e-18	1.9e-15	6.2e-16	1.8e-16	True	False
44.0	3.6e-18	1.2e-18	1.4e-15	4.7e-16	1.2e-16	True	False
45.0	2.9e-18	9.6e-19	2.8e-15	9.2e-16	1.3e-16	True	False
46.0	8.5e-18	2.8e-18	8.1e-16	2.7e-16	1.4e-16	True	False
47.0	2.8e-18	9.2e-19	7.4e-16	2.5e-16	1.9e-16	True	False
48.0	2.2e-18	7.4e-19	8.7e-16	2.9e-16	1.0e-16	True	False
49.0	3.9e-18	1.3e-18	7.3e-16	2.4e-16	2.4e-16	True	False
50.0	2.8e-18	9.4e-19	8.8e-16	2.9e-16	2.3e-16	True	False
51.0	7.4e-18	2.5e-18	1.2e-15	4.0e-16	2.2e-16	True	False
52.0	6.2e-18	2.1e-18	1.5e-15	5.1e-16	1.1e-16	True	False
53.0	2.4e-18	8.0e-19	4.7e-16	1.6e-16	9.9e-17	True	False
54.0	1.4e-16	4.5e-17	6.6e-15	2.2e-15	2.2e-16	True	False
55.0	8.5e-18	2.8e-18	1.7e-15	5.7e-16	1.8e-16	True	False

56.0	4.2e-18	1.4e-18	1.2e-15	4.1e-16	2.1e-16	True	False
57.0	8.5e-18	2.8e-18	6.3e-16	2.1e-16	1.2e-16	True	False
58.0	3.4e-18	1.1e-18	1.3e-15	4.4e-16	1.8e-16	True	False
59.0	6.7e-18	2.2e-18	1.4e-15	4.7e-16	1.6e-16	True	False
60.0	1.3e-17	4.4e-18	1.5e-15	5.1e-16	1.1e-16	True	False
61.0	3.0e-18	9.9e-19	6.5e-16	2.2e-16	1.2e-16	True	False
62.0	2.4e-18	8.1e-19	5.0e-16	1.7e-16	1.2e-16	True	False
63.0	2.8e-18	9.5e-19	2.1e-15	7.1e-16	1.6e-16	True	False
64.0	3.3e-18	1.1e-18	2.6e-15	8.8e-16	1.6e-16	True	False
65.0	3.9e-18	1.3e-18	5.6e-16	1.9e-16	1.8e-16	True	False
66.0	4.0e-18	1.3e-18	5.6e-16	1.9e-16	2.7e-16	True	False
67.0	8.7e-18	2.9e-18	4.5e-16	1.5e-16	1.8e-16	True	False
68.0	3.9e-18	1.3e-18	1.8e-15	6.0e-16	1.4e-16	True	False
69.0	5.1e-18	1.7e-18	1.1e-15	3.5e-16	1.6e-16	True	False
70.0	5.3e-17	1.8e-17	1.7e-15	5.6e-16	1.6e-16	True	False
71.0	2.8e-15	9.2e-16	6.6e-14	2.2e-14	8.2e-16	True	False
72.0	1.1e-17	3.7e-18	1.3e-15	4.4e-16	2.0e-16	True	False
73.0	6.9e-18	2.3e-18	5.8e-16	1.9e-16	1.5e-16	True	False
74.0	4.4e-18	1.5e-18	2.2e-15	7.4e-16	2.0e-16	True	False
75.0	2.7e-18	9.0e-19	9.5e-16	3.2e-16	1.4e-16	True	False
76.0	5.6e-18	1.9e-18	8.1e-16	2.7e-16	1.2e-16	True	False
77.0	2.6e-18	8.7e-19	1.0e-15	3.4e-16	1.1e-16	True	False
78.0	2.6e-18	8.7e-19	2.0e-15	6.8e-16	1.2e-16	True	False
79.0	2.6e-18	8.6e-19	3.5e-16	1.2e-16	1.6e-16	True	False
80.0	3.2e-18	1.1e-18	9.7e-16	3.2e-16	1.4e-16	True	False
81.0	2.3e-18	7.8e-19	3.9e-16	1.3e-16	1.3e-16	True	False
82.0	2.8e-18	9.4e-19	6.6e-16	2.2e-16	1.1e-16	True	False
83.0	3.0e-18	9.9e-19	8.4e-16	2.8e-16	1.1e-16	True	False
84.0	2.8e-18	9.3e-19	1.7e-15	5.7e-16	1.3e-16	True	False
85.0	2.1e-18	7.1e-19	1.4e-15	4.5e-16	1.2e-16	True	False
86.0	5.7e-17	1.9e-17	2.3e-15	7.6e-16	1.0e-16	True	False
87.0	4.3e-18	1.4e-18	1.5e-15	5.1e-16	1.2e-16	True	False
88.0	2.8e-18	9.3e-19	8.7e-16	2.9e-16	1.2e-16	True	False
89.0	2.9e-18	9.6e-19	1.0e-15	3.5e-16	1.1e-16	True	False
90.0	2.7e-18	9.1e-19	1.1e-15	3.8e-16	1.4e-16	True	False
91.0	7.2e-17	2.4e-17	2.5e-15	8.2e-16	1.1e-16	True	False
92.0	1.9e-18	6.2e-19	4.8e-16	1.6e-16	8.8e-17	True	False
93.0	5.1e-18	1.7e-18	1.1e-15	3.8e-16	8.4e-17	True	False
94.0	2.7e-18	9.1e-19	1.5e-15	5.0e-16	1.4e-16	True	False
95.0	2.1e-18	7.0e-19	5.5e-16	1.8e-16	1.0e-16	True	False
96.0	8.5e-18	2.8e-18	4.4e-16	1.5e-16	9.6e-17	True	False
97.0	2.8e-18	9.3e-19	1.0e-15	3.5e-16	8.1e-17	True	False
98.0	2.3e-18	7.7e-19	2.7e-15	9.1e-16	1.5e-16	True	False
99.0	2.0e-18	6.7e-19	7.0e-16	2.3e-16	7.3e-17	True	False
100.0	1.9e-17	6.2e-18	1.4e-15	4.7e-16	1.5e-16	True	False
101.0	2.5e-18	8.3e-19	1.2e-15	4.1e-16	1.4e-16	True	False
102.0	2.4e-18	8.1e-19	7.2e-16	2.4e-16	8.7e-17	True	False
103.0	3.3e-18	1.1e-18	1.7e-16	5.5e-17	9.6e-17	True	False
104.0	3.6e-18	1.2e-18	4.4e-16	1.5e-16	7.3e-17	True	False
105.0	3.1e-18	1.0e-18	1.4e-15	4.6e-16	9.0e-17	True	False
106.0	1.8e-17	6.1e-18	1.6e-15	5.5e-16	9.5e-17	True	False
107.0	3.7e-18	1.2e-18	1.1e-15	3.8e-16	1.0e-16	True	False
108.0	2.9e-18	9.5e-19	3.0e-16	9.9e-17	1.0e-16	True	False
109.0	2.4e-18	7.9e-19	2.4e-16	8.2e-17	1.5e-16	True	False
110.0	2.7e-18	9.2e-19	4.9e-16	1.6e-16	1.4e-16	True	False
111.0	2.5e-18	8.3e-19	4.7e-16	1.6e-16	1.4e-16	True	False
112.0	3.6e-18	1.2e-18	2.5e-15	8.3e-16	1.7e-16	True	False
113.0	2.9e-18	9.7e-19	6.6e-16	2.2e-16	1.4e-16	True	False
114.0	2.1e-18	7.1e-19	1.7e-15	5.6e-16	9.0e-17	True	False
115.0	3.0e-18	1.0e-18	3.1e-16	1.0e-16	8.2e-17	True	False
116.0	6.0e-18	2.0e-18	5.0e-16	1.7e-16	1.2e-16	True	False
117.0	2.7e-18	9.0e-19	1.3e-15	4.3e-16	1.2e-16	True	False

118.0	2.4e-18	8.2e-19	6.6e-16	2.2e-16	9.1e-17	True	False
119.0	3.2e-18	1.1e-18	1.1e-15	3.7e-16	2.0e-16	True	False
120.0	6.4e-18	2.1e-18	3.5e-16	1.2e-16	8.2e-17	True	False
121.0	2.4e-18	8.1e-19	4.7e-16	1.6e-16	9.1e-17	True	False
122.0	3.2e-18	1.1e-18	4.3e-15	1.4e-15	1.5e-16	True	False
123.0	2.9e-18	9.7e-19	1.5e-15	5.2e-16	1.8e-16	True	False
124.0	9.7e-18	3.2e-18	1.5e-15	4.9e-16	1.9e-16	True	False
125.0	7.3e-18	2.4e-18	4.2e-16	1.4e-16	8.9e-17	True	False
126.0	4.9e-18	1.6e-18	1.9e-15	6.5e-16	1.6e-16	True	False
127.0	2.8e-18	9.3e-19	1.8e-15	5.9e-16	1.1e-16	True	False
128.0	2.5e-18	8.4e-19	7.8e-16	2.6e-16	9.3e-17	True	False
129.0	3.1e-18	1.0e-18	1.5e-15	5.0e-16	1.1e-16	True	False
130.0	4.3e-18	1.4e-18	1.6e-15	5.2e-16	8.5e-17	True	False
131.0	2.8e-18	9.3e-19	3.7e-16	1.2e-16	9.4e-17	True	False
132.0	2.3e-18	7.7e-19	1.3e-15	4.3e-16	1.6e-16	True	False
133.0	1.2e-17	4.0e-18	6.9e-16	2.3e-16	8.0e-17	True	False
134.0	1.0e-17	3.4e-18	1.3e-15	4.3e-16	1.1e-16	True	False
135.0	2.8e-18	9.4e-19	1.4e-15	4.7e-16	1.1e-16	True	False
136.0	3.8e-18	1.3e-18	9.8e-16	3.3e-16	8.5e-17	True	False
137.0	1.1e-17	3.6e-18	9.3e-16	3.1e-16	8.8e-17	True	False
138.0	2.7e-18	8.9e-19	1.2e-15	4.1e-16	1.3e-16	True	False
139.0	3.4e-18	1.1e-18	1.1e-15	3.5e-16	1.0e-16	True	False
140.0	2.2e-18	7.3e-19	9.5e-16	3.2e-16	1.6e-16	True	False
141.0	2.1e-18	7.0e-19	4.1e-15	1.4e-15	1.2e-16	True	False

HeI 7065$\mathring{A}$

Star ID	*f(peak)* erg/Å/s/cm^2	Line peak RMS erg/Å/s/cm^2	F erg/s/cm^2	ΔF_{RMS} erg/s/cm^2	ΔF_{sky} erg/s/cm^2	Upper limit	Good flux
0.0	3.5e-18	1.2e-18	2.3e-16	7.7e-17	8.9e-17	True	False
1.0	4.2e-16	1.4e-16	1.9e-14	6.3e-15	3.7e-16	True	False
2.0	1.3e-17	4.4e-18	4.7e-16	1.6e-16	1.1e-16	True	False
3.0	3.0e-18	9.9e-19	3.0e-16	9.9e-17	8.7e-17	True	False
4.0	9.6e-18	3.2e-18	6.4e-16	2.1e-16	1.8e-16	True	False
5.0	2.6e-18	8.5e-19	1.3e-16	4.5e-17	1.1e-16	True	False
6.0	2.3e-18	7.6e-19	3.3e-16	1.1e-16	9.3e-17	True	False
7.0	3.5e-18	1.2e-18	5.9e-16	2.0e-16	1.0e-16	True	False
8.0	3.1e-18	1.0e-18	9.2e-16	3.1e-16	9.2e-17	True	False
9.0	7.1e-18	2.4e-18	4.2e-16	1.4e-16	1.9e-16	True	False
10.0	6.1e-18	2.0e-18	3.9e-16	1.3e-16	1.9e-16	True	False
11.0	1.1e-17	3.6e-18	4.6e-16	1.5e-16	9.7e-17	True	False
12.0	1.4e-17	4.8e-18	6.3e-16	2.1e-16	1.2e-16	True	False
13.0	7.6e-18	2.5e-18	3.6e-16	1.2e-16	1.2e-16	True	False
14.0	4.3e-18	1.4e-18	1.1e-15	3.6e-16	1.6e-16	True	False
15.0	1.1e-17	3.7e-18	5.0e-16	1.7e-16	9.5e-17	True	False
16.0	7.2e-18	2.4e-18	4.0e-16	1.3e-16	1.1e-16	True	False
17.0	6.3e-18	2.1e-18	9.2e-16	3.1e-16	9.5e-17	True	False
18.0	2.3e-17	7.6e-18	8.7e-16	2.9e-16	9.1e-17	True	False
19.0	6.2e-18	2.1e-18	4.1e-16	1.4e-16	9.8e-17	True	False
20.0	3.5e-18	1.2e-18	3.9e-16	1.3e-16	1.2e-16	True	False
21.0	3.8e-18	1.3e-18	4.6e-16	1.5e-16	9.5e-17	True	False
22.0	9.6e-18	3.2e-18	3.3e-16	1.1e-16	1.3e-16	True	False
23.0	4.5e-18	1.5e-18	2.6e-16	8.5e-17	1.1e-16	True	False
24.0	1.2e-17	3.9e-18	6.1e-16	2.0e-16	1.0e-16	True	False
25.0	1.5e-17	5.0e-18	7.9e-16	2.6e-16	7.6e-17	True	False
26.0	2.1e-18	7.0e-19	3.1e-16	1.0e-16	1.0e-16	True	False
27.0	3.0e-17	1.0e-17	1.5e-15	5.0e-16	9.7e-17	True	False
28.0	1.1e-17	3.8e-18	3.5e-16	1.2e-16	8.5e-17	True	False
29.0	3.8e-17	1.3e-17	1.4e-15	4.6e-16	1.7e-16	True	False
30.0	3.6e-18	1.2e-18	3.1e-16	1.0e-16	1.0e-16	True	False
31.0	3.3e-18	1.1e-18	2.5e-16	8.2e-17	2.2e-16	True	False
32.0	2.9e-18	9.7e-19	4.0e-16	1.3e-16	9.4e-17	True	False
33.0	5.2e-18	1.7e-18	3.6e-16	1.2e-16	9.3e-17	True	False
34.0	1.8e-17	6.0e-18	4.9e-16	1.6e-16	1.6e-16	True	False
35.0	7.0e-18	2.3e-18	3.7e-16	1.2e-16	2.8e-16	True	False
36.0	6.7e-18	2.2e-18	6.2e-16	2.1e-16	1.2e-16	True	False
37.0	2.9e-18	9.8e-19	3.9e-16	1.3e-16	9.1e-17	True	False
38.0	6.4e-18	2.1e-18	3.0e-16	9.9e-17	1.3e-16	True	False
39.0	3.8e-18	1.3e-18	3.6e-16	1.2e-16	2.0e-16	True	False
40.0	2.7e-18	9.1e-19	5.9e-16	2.0e-16	9.2e-17	True	False
41.0	2.5e-18	8.2e-19	6.9e-16	2.3e-16	1.2e-16	True	False
42.0	2.3e-18	7.7e-19	1.3e-16	4.4e-17	1.1e-16	True	False
43.0	7.3e-18	2.4e-18	2.5e-16	8.5e-17	1.4e-16	True	False
44.0	6.1e-18	2.0e-18	2.4e-16	7.9e-17	9.2e-17	True	False
45.0	2.6e-18	8.7e-19	5.9e-16	2.0e-16	1.1e-16	True	False
46.0	1.2e-17	4.1e-18	4.8e-16	1.6e-16	1.2e-16	True	False
47.0	3.4e-18	1.1e-18	3.0e-16	9.9e-17	1.6e-16	True	False
48.0	2.1e-18	6.9e-19	3.8e-16	1.3e-16	8.1e-17	True	False
49.0	8.6e-18	2.9e-18	3.5e-16	1.2e-16	2.0e-16	True	False
50.0	2.4e-18	8.0e-19	2.2e-16	7.4e-17	1.8e-16	True	False
51.0	1.2e-17	4.0e-18	7.4e-16	2.5e-16	2.1e-16	True	False
52.0	1.3e-17	4.2e-18	4.9e-16	1.6e-16	9.5e-17	True	False
53.0	2.7e-18	9.0e-19	3.1e-16	1.0e-16	8.4e-17	True	False
54.0	1.9e-16	6.5e-17	1.0e-14	3.4e-15	1.9e-16	True	False
55.0	1.1e-17	3.7e-18	7.0e-16	2.3e-16	1.5e-16	True	False

56.0	5.0e-18	1.7e-18	5.3e-16	1.8e-16	1.8e-16	True	False
57.0	1.2e-17	3.9e-18	3.8e-16	1.3e-16	1.1e-16	True	False
58.0	6.2e-18	2.1e-18	1.1e-15	3.7e-16	1.5e-16	True	False
59.0	1.1e-17	3.7e-18	5.0e-16	1.7e-16	1.3e-16	True	False
60.0	1.7e-17	5.8e-18	6.8e-16	2.3e-16	9.2e-17	True	False
61.0	4.0e-18	1.3e-18	3.2e-16	1.1e-16	1.0e-16	True	False
62.0	2.1e-18	6.8e-19	2.6e-16	8.8e-17	1.0e-16	True	False
63.0	3.7e-18	1.2e-18	3.8e-16	1.3e-16	1.3e-16	True	False
64.0	4.7e-18	1.6e-18	1.7e-15	5.6e-16	1.2e-16	True	False
65.0	6.7e-18	2.2e-18	3.5e-16	1.2e-16	1.5e-16	True	False
66.0	8.5e-18	2.8e-18	7.8e-16	2.6e-16	2.3e-16	True	False
67.0	1.5e-17	5.0e-18	6.0e-16	2.0e-16	1.5e-16	True	False
68.0	8.2e-18	2.7e-18	3.5e-16	1.2e-16	1.2e-16	True	False
69.0	9.9e-18	3.3e-18	4.2e-16	1.4e-16	1.3e-16	True	False
70.0	6.2e-17	2.1e-17	2.1e-15	6.9e-16	1.4e-16	True	False
71.0	5.3e-15	1.8e-15	9.2e-14	3.1e-14	7.7e-16	True	False
72.0	2.6e-17	8.8e-18	1.0e-15	3.4e-16	1.7e-16	True	False
73.0	1.3e-17	4.4e-18	4.1e-16	1.4e-16	1.2e-16	True	False
74.0	3.8e-18	1.3e-18	3.0e-16	1.0e-16	1.8e-16	True	False
75.0	4.0e-18	1.3e-18	1.5e-16	5.0e-17	1.1e-16	True	False
76.0	1.0e-17	3.5e-18	6.5e-16	2.2e-16	1.0e-16	True	False
77.0	2.3e-18	7.7e-19	8.2e-16	2.7e-16	8.6e-17	True	False
78.0	3.0e-18	1.0e-18	6.6e-16	2.2e-16	9.4e-17	True	False
79.0	2.7e-18	9.1e-19	3.6e-16	1.2e-16	1.3e-16	True	False
80.0	4.5e-18	1.5e-18	3.4e-16	1.1e-16	1.2e-16	True	False
81.0	2.3e-18	7.8e-19	2.4e-16	8.0e-17	1.1e-16	True	False
82.0	2.4e-18	7.9e-19	3.5e-16	1.2e-16	8.8e-17	True	False
83.0	3.8e-18	1.3e-18	1.9e-16	6.2e-17	9.0e-17	True	False
84.0	2.9e-18	9.6e-19	3.6e-16	1.2e-16	1.1e-16	True	False
85.0	2.1e-18	7.0e-19	7.6e-16	2.5e-16	1.0e-16	True	False
86.0	7.0e-17	2.3e-17	3.5e-15	1.2e-15	9.3e-17	True	False
87.0	7.4e-18	2.5e-18	3.0e-16	1.0e-16	1.0e-16	True	False
88.0	2.7e-18	9.0e-19	8.6e-17	2.9e-17	1.0e-16	True	False
89.0	4.8e-18	1.6e-18	2.3e-16	7.8e-17	9.8e-17	True	False
90.0	3.2e-18	1.1e-18	3.5e-16	1.2e-16	1.1e-16	True	False
91.0	7.1e-17	2.4e-17	3.1e-15	1.0e-15	9.0e-17	True	False
92.0	4.1e-18	1.4e-18	2.8e-16	9.4e-17	7.3e-17	True	False
93.0	8.2e-18	2.7e-18	2.4e-16	8.1e-17	6.6e-17	True	False
94.0	3.8e-18	1.3e-18	3.0e-16	1.0e-16	1.1e-16	True	False
95.0	3.3e-18	1.1e-18	2.1e-16	7.1e-17	8.6e-17	True	False
96.0	1.2e-17	4.1e-18	4.2e-16	1.4e-16	8.1e-17	True	False
97.0	2.7e-18	9.1e-19	2.7e-16	8.9e-17	7.2e-17	True	False
98.0	2.6e-18	8.6e-19	8.0e-16	2.7e-16	1.2e-16	True	False
99.0	2.9e-18	9.8e-19	1.6e-16	5.3e-17	6.6e-17	True	False
100.0	3.1e-17	1.0e-17	1.5e-15	4.9e-16	1.2e-16	True	False
101.0	2.0e-18	6.8e-19	5.4e-16	1.8e-16	1.1e-16	True	False
102.0	2.4e-18	8.0e-19	2.5e-16	8.3e-17	7.0e-17	True	False
103.0	5.1e-18	1.7e-18	2.0e-16	6.6e-17	7.9e-17	True	False
104.0	6.8e-18	2.3e-18	3.0e-16	9.9e-17	6.9e-17	True	False
105.0	2.4e-18	8.1e-19	1.5e-16	4.9e-17	8.1e-17	True	False
106.0	3.5e-17	1.2e-17	1.8e-15	5.9e-16	7.8e-17	True	False
107.0	5.6e-18	1.9e-18	5.1e-16	1.7e-16	8.3e-17	True	False
108.0	2.5e-18	8.3e-19	2.7e-16	9.1e-17	8.5e-17	True	False
109.0	2.5e-18	8.4e-19	2.1e-16	7.0e-17	1.2e-16	True	False
110.0	2.7e-18	8.9e-19	5.2e-16	1.7e-16	1.1e-16	True	False
111.0	3.5e-18	1.2e-18	5.7e-16	1.9e-16	1.1e-16	True	False
112.0	6.7e-18	2.2e-18	8.9e-16	3.0e-16	1.4e-16	True	False
113.0	4.9e-18	1.6e-18	2.3e-16	7.6e-17	1.1e-16	True	False
114.0	1.6e-18	5.5e-19	3.1e-16	1.0e-16	7.6e-17	True	False
115.0	4.8e-18	1.6e-18	3.7e-16	1.2e-16	6.5e-17	True	False
116.0	1.1e-17	3.7e-18	6.5e-16	2.2e-16	9.7e-17	True	False
117.0	2.2e-18	7.4e-19	7.2e-16	2.4e-16	9.9e-17	True	False

118.0	2.1e-18	6.9e-19	1.7e-16	5.6e-17	7.3e-17	True	False
119.0	2.6e-18	8.5e-19	7.2e-16	2.4e-16	1.6e-16	True	False
120.0	1.0e-17	3.3e-18	3.6e-16	1.2e-16	6.8e-17	True	False
121.0	3.2e-18	1.1e-18	1.2e-16	3.9e-17	7.7e-17	True	False
122.0	4.8e-18	1.6e-18	2.1e-15	7.1e-16	1.3e-16	True	False
123.0	3.7e-18	1.2e-18	1.9e-16	6.4e-17	1.6e-16	True	False
124.0	1.5e-17	4.9e-18	8.2e-16	2.7e-16	1.5e-16	True	False
125.0	9.5e-18	3.2e-18	3.9e-16	1.3e-16	7.6e-17	True	False
126.0	9.3e-18	3.1e-18	1.2e-15	3.9e-16	1.3e-16	True	False
127.0	4.3e-18	1.4e-18	4.2e-16	1.4e-16	8.4e-17	True	False
128.0	2.8e-18	9.2e-19	3.3e-16	1.1e-16	7.4e-17	True	False
129.0	3.8e-18	1.3e-18	4.7e-16	1.6e-16	9.3e-17	True	False
130.0	6.8e-18	2.3e-18	3.2e-16	1.1e-16	6.9e-17	True	False
131.0	3.3e-18	1.1e-18	1.8e-16	6.1e-17	7.7e-17	True	False
132.0	3.2e-18	1.1e-18	1.8e-16	5.9e-17	1.2e-16	True	False
133.0	1.5e-17	4.9e-18	5.5e-16	1.8e-16	7.0e-17	True	False
134.0	1.2e-17	4.1e-18	7.5e-16	2.5e-16	8.6e-17	True	False
135.0	2.6e-18	8.7e-19	4.9e-16	1.6e-16	9.2e-17	True	False
136.0	8.1e-18	2.7e-18	6.0e-16	2.0e-16	7.0e-17	True	False
137.0	8.9e-18	3.0e-18	5.5e-16	1.8e-16	7.3e-17	True	False
138.0	2.4e-18	8.2e-19	6.4e-16	2.1e-16	9.6e-17	True	False
139.0	3.4e-18	1.1e-18	3.5e-16	1.2e-16	8.0e-17	True	False
140.0	2.8e-18	9.3e-19	7.7e-16	2.6e-16	1.1e-16	True	False
141.0	3.2e-18	1.1e-18	6.4e-16	2.1e-16	9.7e-17	True	False

HeI 7281$\mathring{A}$

Star ID	*f(peak)* erg/Å/s/cm^2	Line peak RMS erg/Å/s/cm^2	F erg/s/cm^2	ΔF_{RMS} erg/s/cm^2	ΔF_{sky} erg/s/cm^2	Upper limit	Good flux
0.0	3.6e-18	1.2e-18	6.5e-17	2.2e-17	5.2e-17	True	False
1.0	7.0e-16	2.3e-16	1.9e-14	6.3e-15	2.0e-16	True	False
2.0	1.5e-17	4.8e-18	2.3e-16	7.6e-17	5.9e-17	True	False
3.0	3.7e-18	1.2e-18	6.2e-17	2.1e-17	5.0e-17	True	False
4.0	1.4e-17	4.5e-18	7.7e-16	2.6e-16	8.9e-17	True	False
5.0	2.9e-18	9.8e-19	5.4e-17	1.8e-17	5.6e-17	True	False
6.0	2.7e-18	8.9e-19	3.6e-17	1.2e-17	4.8e-17	True	False
7.0	3.9e-18	1.3e-18	1.3e-16	4.2e-17	5.6e-17	True	False
8.0	2.9e-18	9.6e-19	4.7e-16	1.6e-16	5.0e-17	True	False
9.0	7.5e-18	2.5e-18	1.5e-16	4.8e-17	1.0e-16	True	False
10.0	8.0e-18	2.7e-18	1.4e-16	4.6e-17	1.0e-16	True	False
11.0	1.3e-17	4.2e-18	2.6e-16	8.6e-17	5.2e-17	True	False
12.0	2.6e-17	8.5e-18	4.5e-16	1.5e-16	6.4e-17	True	False
13.0	1.3e-17	4.3e-18	2.5e-16	8.4e-17	5.9e-17	True	False
14.0	3.6e-18	1.2e-18	1.0e-16	3.5e-17	8.8e-17	True	False
15.0	1.7e-17	5.6e-18	3.1e-16	1.0e-16	4.9e-17	True	False
16.0	1.1e-17	3.7e-18	1.9e-16	6.4e-17	5.6e-17	True	False
17.0	9.6e-18	3.2e-18	2.0e-16	6.8e-17	5.3e-17	True	False
18.0	3.7e-17	1.2e-17	6.8e-16	2.3e-16	5.0e-17	True	False
19.0	9.5e-18	3.2e-18	1.7e-16	5.7e-17	5.2e-17	True	False
20.0	4.3e-18	1.4e-18	7.4e-17	2.5e-17	6.7e-17	True	False
21.0	4.7e-18	1.6e-18	1.3e-16	4.5e-17	5.0e-17	True	False
22.0	1.1e-17	3.8e-18	2.2e-16	7.5e-17	7.5e-17	True	False
23.0	6.5e-18	2.2e-18	1.3e-16	4.3e-17	6.8e-17	True	False
24.0	1.8e-17	6.1e-18	3.3e-16	1.1e-16	5.4e-17	True	False
25.0	1.7e-17	5.8e-18	3.7e-16	1.2e-16	4.3e-17	True	False
26.0	4.3e-18	1.4e-18	8.6e-17	2.9e-17	5.2e-17	True	False
27.0	5.2e-17	1.7e-17	6.9e-16	2.3e-16	5.3e-17	True	False
28.0	1.5e-17	5.0e-18	2.5e-16	8.2e-17	4.8e-17	True	False
29.0	5.3e-17	1.8e-17	8.2e-16	2.7e-16	9.6e-17	True	False
30.0	4.3e-18	1.4e-18	7.9e-17	2.6e-17	5.8e-17	True	False
31.0	3.5e-18	1.2e-18	5.3e-17	1.8e-17	1.2e-16	True	False
32.0	2.9e-18	9.8e-19	6.8e-17	2.3e-17	5.4e-17	True	False
33.0	8.3e-18	2.8e-18	1.5e-16	4.9e-17	4.9e-17	True	False
34.0	2.3e-17	7.8e-18	4.0e-16	1.3e-16	9.2e-17	True	False
35.0	8.1e-18	2.7e-18	1.3e-16	4.5e-17	1.5e-16	True	False
36.0	8.0e-18	2.7e-18	1.5e-16	4.8e-17	6.5e-17	True	False
37.0	3.2e-18	1.1e-18	6.0e-17	2.0e-17	4.9e-17	True	False
38.0	9.7e-18	3.2e-18	1.5e-16	4.9e-17	7.1e-17	True	False
39.0	5.1e-18	1.7e-18	9.1e-17	3.0e-17	1.1e-16	True	False
40.0	3.3e-18	1.1e-18	7.8e-17	2.6e-17	5.0e-17	True	False
41.0	2.4e-18	8.1e-19	5.0e-17	1.7e-17	5.8e-17	True	False
42.0	2.9e-18	9.7e-19	4.7e-17	1.6e-17	5.9e-17	True	False
43.0	9.0e-18	3.0e-18	1.8e-16	5.9e-17	6.8e-17	True	False
44.0	6.7e-18	2.2e-18	1.2e-16	4.1e-17	5.0e-17	True	False
45.0	2.5e-18	8.4e-19	7.6e-17	2.5e-17	5.4e-17	True	False
46.0	1.6e-17	5.4e-18	2.6e-16	8.5e-17	7.3e-17	True	False
47.0	4.9e-18	1.6e-18	9.1e-17	3.0e-17	8.7e-17	True	False
48.0	3.0e-18	9.9e-19	5.5e-17	1.8e-17	4.3e-17	True	False
49.0	1.3e-17	4.3e-18	2.3e-16	7.7e-17	8.4e-17	True	False
50.0	2.8e-18	9.4e-19	6.2e-17	2.1e-17	9.5e-17	True	False
51.0	2.3e-17	7.6e-18	4.0e-16	1.3e-16	1.2e-16	True	False
52.0	2.1e-17	6.9e-18	3.7e-16	1.2e-16	5.8e-17	True	False
53.0	3.1e-18	1.0e-18	5.0e-17	1.7e-17	4.8e-17	True	False
54.0	4.1e-16	1.4e-16	9.0e-15	3.0e-15	1.0e-16	True	False
55.0	1.7e-17	5.6e-18	2.8e-16	9.4e-17	6.1e-17	True	False

56.0	7.1e-18	2.4e-18	1.3e-16	4.2e-17	1.1e-16	True	False
57.0	1.7e-17	5.6e-18	3.0e-16	1.0e-16	6.3e-17	True	False
58.0	9.6e-18	3.2e-18	1.9e-16	6.3e-17	6.7e-17	True	False
59.0	1.4e-17	4.8e-18	3.0e-16	9.9e-17	6.3e-17	True	False
60.0	2.7e-17	9.0e-18	4.3e-16	1.4e-16	4.9e-17	True	False
61.0	4.6e-18	1.5e-18	8.5e-17	2.8e-17	5.6e-17	True	False
62.0	1.8e-18	5.9e-19	5.9e-17	2.0e-17	5.1e-17	True	False
63.0	5.9e-18	2.0e-18	1.2e-16	3.8e-17	6.2e-17	True	False
64.0	6.1e-18	2.0e-18	1.5e-16	5.0e-17	5.9e-17	True	False
65.0	1.1e-17	3.7e-18	1.7e-16	5.8e-17	6.9e-17	True	False
66.0	1.0e-17	3.3e-18	1.8e-16	6.0e-17	1.3e-16	True	False
67.0	2.3e-17	7.8e-18	4.3e-16	1.4e-16	7.3e-17	True	False
68.0	1.1e-17	3.6e-18	2.1e-16	7.0e-17	5.7e-17	True	False
69.0	1.3e-17	4.4e-18	2.8e-16	9.3e-17	6.8e-17	True	False
70.0	8.8e-17	2.9e-17	1.4e-15	4.6e-16	6.9e-17	True	False
71.0	1.2e-15	4.2e-16	8.4e-14	2.8e-14	4.5e-16	True	False
72.0	3.3e-17	1.1e-17	6.3e-16	2.1e-16	8.5e-17	True	False
73.0	1.4e-17	4.5e-18	2.5e-16	8.3e-17	6.6e-17	True	False
74.0	5.3e-18	1.8e-18	7.9e-17	2.6e-17	9.3e-17	True	False
75.0	5.8e-18	1.9e-18	1.0e-16	3.5e-17	6.0e-17	True	False
76.0	2.1e-17	7.0e-18	3.6e-16	1.2e-16	5.3e-17	True	False
77.0	2.7e-18	8.8e-19	5.3e-17	1.8e-17	4.5e-17	True	False
78.0	3.7e-18	1.2e-18	8.9e-17	3.0e-17	4.9e-17	True	False
79.0	2.7e-18	9.0e-19	4.5e-17	1.5e-17	7.2e-17	True	False
80.0	3.6e-18	1.2e-18	7.0e-17	2.3e-17	6.5e-17	True	False
81.0	2.9e-18	9.7e-19	5.8e-17	1.9e-17	5.5e-17	True	False
82.0	2.2e-18	7.4e-19	3.7e-17	1.2e-17	4.8e-17	True	False
83.0	3.8e-18	1.3e-18	6.7e-17	2.2e-17	5.9e-17	True	False
84.0	2.9e-18	9.7e-19	4.6e-17	1.5e-17	5.8e-17	True	False
85.0	2.6e-18	8.6e-19	6.6e-17	2.2e-17	4.8e-17	True	False
86.0	1.2e-16	4.2e-17	2.3e-15	7.7e-16	5.9e-17	True	False
87.0	1.1e-17	3.6e-18	1.9e-16	6.5e-17	6.3e-17	True	False
88.0	3.0e-18	1.0e-18	9.0e-17	3.0e-17	5.9e-17	True	False
89.0	6.1e-18	2.0e-18	1.1e-16	3.7e-17	5.8e-17	True	False
90.0	4.0e-18	1.3e-18	7.5e-17	2.5e-17	5.9e-17	True	False
91.0	1.2e-16	3.9e-17	1.7e-15	5.5e-16	5.1e-17	True	False
92.0	6.1e-18	2.0e-18	1.1e-16	3.5e-17	4.7e-17	True	False
93.0	1.0e-17	3.3e-18	2.1e-16	7.1e-17	4.1e-17	True	False
94.0	4.8e-18	1.6e-18	8.2e-17	2.7e-17	5.3e-17	True	False
95.0	3.8e-18	1.3e-18	6.8e-17	2.3e-17	5.6e-17	True	False
96.0	1.4e-17	4.7e-18	2.2e-16	7.3e-17	4.7e-17	True	False
97.0	2.7e-18	9.1e-19	3.9e-17	1.3e-17	4.7e-17	True	False
98.0	3.3e-18	1.1e-18	9.7e-17	3.2e-17	5.5e-17	True	False
99.0	4.4e-18	1.5e-18	7.9e-17	2.6e-17	4.6e-17	True	False
100.0	5.3e-17	1.8e-17	7.2e-16	2.4e-16	5.6e-17	True	False
101.0	2.4e-18	7.9e-19	5.5e-17	1.8e-17	5.2e-17	True	False
102.0	2.2e-18	7.3e-19	3.1e-17	1.0e-17	4.3e-17	True	False
103.0	5.7e-18	1.9e-18	1.1e-16	3.6e-17	4.7e-17	True	False
104.0	1.1e-17	3.6e-18	1.8e-16	6.1e-17	4.5e-17	True	False
105.0	2.7e-18	8.9e-19	4.8e-17	1.6e-17	5.3e-17	True	False
106.0	6.1e-17	2.0e-17	1.3e-15	4.2e-16	4.8e-17	True	False
107.0	7.5e-18	2.5e-18	1.4e-16	4.6e-17	4.6e-17	True	False
108.0	2.6e-18	8.8e-19	3.5e-17	1.2e-17	4.7e-17	True	False
109.0	2.5e-18	8.5e-19	3.8e-17	1.3e-17	5.8e-17	True	False
110.0	3.3e-18	1.1e-18	6.6e-17	2.2e-17	5.0e-17	True	False
111.0	5.0e-18	1.7e-18	8.3e-17	2.8e-17	5.3e-17	True	False
112.0	7.8e-18	2.6e-18	2.0e-16	6.6e-17	6.0e-17	True	False
113.0	6.3e-18	2.1e-18	1.1e-16	3.8e-17	5.7e-17	True	False
114.0	2.4e-18	7.9e-19	3.8e-17	1.3e-17	4.7e-17	True	False
115.0	5.8e-18	1.9e-18	1.2e-16	3.9e-17	4.1e-17	True	False
116.0	1.3e-17	4.4e-18	2.2e-16	7.3e-17	5.1e-17	True	False
117.0	3.2e-18	1.1e-18	5.9e-17	2.0e-17	5.6e-17	True	False

118.0	2.5e-18	8.3e-19	3.5e-17	1.2e-17	4.5e-17	True	False
119.0	2.5e-18	8.3e-19	5.6e-17	1.9e-17	7.1e-17	True	False
120.0	1.2e-17	3.9e-18	2.3e-16	7.7e-17	4.2e-17	True	False
121.0	2.6e-18	8.6e-19	4.1e-17	1.4e-17	4.8e-17	True	False
122.0	6.8e-18	2.3e-18	2.1e-16	7.0e-17	6.2e-17	True	False
123.0	4.0e-18	1.3e-18	8.4e-17	2.8e-17	7.3e-17	True	False
124.0	2.5e-17	8.4e-18	4.0e-16	1.3e-16	6.5e-17	True	False
125.0	8.7e-18	2.9e-18	2.2e-16	7.5e-17	4.3e-17	True	False
126.0	1.3e-17	4.2e-18	2.6e-16	8.6e-17	5.9e-17	True	False
127.0	6.9e-18	2.3e-18	1.3e-16	4.4e-17	4.7e-17	True	False
128.0	3.3e-18	1.1e-18	6.2e-17	2.1e-17	4.4e-17	True	False
129.0	7.9e-18	2.6e-18	1.3e-16	4.4e-17	5.0e-17	True	False
130.0	9.5e-18	3.2e-18	1.7e-16	5.6e-17	4.2e-17	True	False
131.0	4.1e-18	1.4e-18	6.8e-17	2.3e-17	4.5e-17	True	False
132.0	3.2e-18	1.1e-18	6.7e-17	2.2e-17	5.8e-17	True	False
133.0	2.5e-17	8.4e-18	3.8e-16	1.3e-16	4.3e-17	True	False
134.0	1.5e-17	5.0e-18	2.7e-16	8.9e-17	4.8e-17	True	False
135.0	2.4e-18	8.1e-19	5.3e-17	1.8e-17	4.8e-17	True	False
136.0	1.1e-17	3.8e-18	2.0e-16	6.7e-17	4.2e-17	True	False
137.0	1.4e-17	4.8e-18	2.0e-16	6.8e-17	4.6e-17	True	False
138.0	2.3e-18	7.6e-19	4.4e-17	1.5e-17	5.4e-17	True	False
139.0	5.2e-18	1.7e-18	8.8e-17	2.9e-17	4.8e-17	True	False
140.0	3.9e-18	1.3e-18	7.8e-17	2.6e-17	5.8e-17	True	False
141.0	3.2e-18	1.1e-18	1.5e-16	4.9e-17	5.1e-17	True	False

[NII] 6548$\mathring{A}$

Star ID	*f(peak)* erg/Å/s/cm^2	Line peak RMS erg/Å/s/cm^2	F erg/s/cm^2	ΔF_{RMS} erg/s/cm^2	ΔF_{sky} erg/s/cm^2	Upper limit	Good flux
0.0	3.2e-18	1.1e-18	1.0e-15	3.4e-16	2.4e-16	True	False
1.0	5.8e-16	1.9e-16	4.3e-14	1.4e-14	3.7e-16	True	False
2.0	1.4e-17	4.7e-18	2.8e-15	9.2e-16	2.3e-16	True	False
3.0	2.8e-18	9.2e-19	2.6e-15	8.7e-16	2.3e-16	True	False
4.0	1.3e-17	4.2e-18	8.1e-15	2.7e-15	2.5e-16	True	False
5.0	2.9e-18	9.6e-19	1.5e-15	5.0e-16	2.1e-16	True	False
6.0	2.9e-18	9.8e-19	2.8e-15	9.3e-16	2.1e-16	True	False
7.0	3.4e-18	1.1e-18	6.5e-15	2.2e-15	2.6e-16	True	False
8.0	3.1e-18	1.0e-18	6.2e-15	2.1e-15	2.5e-16	True	False
9.0	4.4e-18	1.5e-18	3.1e-15	1.0e-15	2.1e-16	True	False
10.0	4.6e-18	1.5e-18	1.9e-15	6.4e-16	2.2e-16	True	False
11.0	7.1e-18	2.4e-18	1.3e-15	4.2e-16	1.6e-16	True	False
12.0	7.9e-18	2.6e-18	6.6e-16	2.2e-16	2.2e-16	True	False
13.0	3.8e-18	1.3e-18	2.2e-15	7.3e-16	1.8e-16	True	False
14.0	3.6e-18	1.2e-18	7.8e-15	2.6e-15	3.3e-16	True	False
15.0	6.7e-18	2.2e-18	5.5e-16	1.8e-16	1.6e-16	True	False
16.0	4.3e-18	1.4e-18	1.7e-15	5.6e-16	1.7e-16	True	False
17.0	5.5e-18	1.8e-18	5.8e-15	1.9e-15	1.9e-16	True	False
18.0	1.7e-17	5.8e-18	1.5e-15	4.9e-16	2.1e-16	True	False
19.0	4.1e-18	1.4e-18	3.4e-15	1.1e-15	2.4e-16	True	False
20.0	2.6e-18	8.7e-19	2.9e-15	9.5e-16	2.5e-16	True	False
21.0	2.6e-18	8.6e-19	2.7e-15	9.0e-16	1.9e-16	True	False
22.0	5.3e-18	1.8e-18	2.8e-15	9.2e-16	2.5e-16	True	False
23.0	3.5e-18	1.2e-18	4.1e-15	1.4e-15	2.2e-16	True	False
24.0	5.0e-18	1.7e-18	3.1e-15	1.0e-15	2.0e-16	True	False
25.0	7.4e-18	2.5e-18	4.2e-15	1.4e-15	2.1e-16	True	False
26.0	3.0e-18	9.9e-19	1.1e-15	3.7e-16	1.6e-16	True	False
27.0	3.5e-17	1.2e-17	6.3e-15	2.1e-15	2.1e-16	True	False
28.0	8.8e-18	2.9e-18	1.9e-15	6.2e-16	1.9e-16	True	False
29.0	3.5e-17	1.2e-17	1.8e-15	6.0e-16	2.3e-16	True	False
30.0	4.3e-18	1.4e-18	3.0e-15	9.8e-16	2.0e-16	True	False
31.0	4.0e-18	1.3e-18	3.2e-15	1.1e-15	2.8e-16	True	False
32.0	3.1e-18	1.0e-18	2.7e-15	8.9e-16	1.9e-16	True	False
33.0	4.5e-18	1.5e-18	1.8e-15	6.0e-16	2.3e-16	True	False
34.0	1.4e-17	4.8e-18	2.9e-15	9.8e-16	2.4e-16	True	False
35.0	7.0e-18	2.3e-18	1.2e-15	4.1e-16	2.7e-16	True	False
36.0	4.7e-18	1.6e-18	5.0e-15	1.7e-15	1.9e-16	True	False
37.0	3.0e-18	9.9e-19	4.0e-15	1.3e-15	2.6e-16	True	False
38.0	7.1e-18	2.4e-18	1.5e-15	4.9e-16	2.6e-16	True	False
39.0	4.2e-18	1.4e-18	2.1e-15	7.0e-16	2.4e-16	True	False
40.0	3.0e-18	1.0e-18	3.9e-15	1.3e-15	2.5e-16	True	False
41.0	2.9e-18	9.7e-19	7.5e-15	2.5e-15	3.0e-16	True	False
42.0	3.0e-18	9.9e-19	2.1e-15	7.0e-16	2.6e-16	True	False
43.0	4.2e-18	1.4e-18	1.8e-15	6.0e-16	2.1e-16	True	False
44.0	3.9e-18	1.3e-18	2.0e-15	6.8e-16	2.5e-16	True	False
45.0	3.0e-18	1.0e-18	5.0e-15	1.7e-15	2.4e-16	True	False
46.0	1.3e-17	4.4e-18	1.7e-15	5.7e-16	2.5e-16	True	False
47.0	3.5e-18	1.2e-18	3.1e-15	1.0e-15	2.7e-16	True	False
48.0	2.7e-18	9.0e-19	3.7e-15	1.2e-15	2.5e-16	True	False
49.0	4.8e-18	1.6e-18	1.9e-15	6.4e-16	3.5e-16	True	False
50.0	3.5e-18	1.2e-18	3.0e-15	1.0e-15	3.1e-16	True	False
51.0	7.3e-18	2.4e-18	1.4e-15	4.5e-16	2.6e-16	True	False
52.0	4.9e-18	1.6e-18	2.8e-15	9.3e-16	2.6e-16	True	False
53.0	3.1e-18	1.0e-18	2.4e-15	7.9e-16	2.4e-16	True	False
54.0	2.8e-16	9.4e-17	2.2e-14	7.2e-15	2.3e-16	True	False
55.0	9.2e-18	3.1e-18	2.9e-15	9.5e-16	3.4e-16	True	False

56.0	4.0e-18	1.3e-18	3.7e-15	1.2e-15	3.2e-16	True	False
57.0	1.1e-17	3.7e-18	1.4e-15	4.7e-16	2.2e-16	True	False
58.0	4.0e-18	1.3e-18	7.7e-15	2.6e-15	2.4e-16	True	False
59.0	8.1e-18	2.7e-18	3.2e-15	1.1e-15	2.1e-16	True	False
60.0	1.7e-17	5.7e-18	1.8e-15	6.0e-16	1.9e-16	True	False
61.0	3.0e-18	9.9e-19	3.2e-15	1.1e-15	2.0e-16	True	False
62.0	3.5e-18	1.2e-18	1.4e-15	4.7e-16	3.1e-16	True	False
63.0	3.5e-18	1.2e-18	2.0e-15	6.7e-16	3.7e-16	True	False
64.0	3.7e-18	1.2e-18	8.8e-15	2.9e-15	2.3e-16	True	False
65.0	4.1e-18	1.4e-18	1.4e-15	4.8e-16	2.5e-16	True	False
66.0	4.2e-18	1.4e-18	3.0e-15	9.9e-16	2.8e-16	True	False
67.0	1.0e-17	3.3e-18	7.1e-16	2.4e-16	2.1e-16	True	False
68.0	3.9e-18	1.3e-18	2.8e-15	9.5e-16	3.9e-16	True	False
69.0	4.1e-18	1.4e-18	1.5e-15	5.1e-16	3.1e-16	True	False
70.0	7.3e-17	2.4e-17	2.3e-15	7.8e-16	2.2e-16	True	False
71.0	9.5e-16	3.2e-16	1.6e-13	5.3e-14	4.7e-16	True	False
72.0	1.3e-17	4.4e-18	2.8e-15	9.4e-16	3.2e-16	True	False
73.0	8.2e-18	2.7e-18	8.5e-16	2.8e-16	2.4e-16	True	False
74.0	4.5e-18	1.5e-18	1.1e-15	3.6e-16	2.7e-16	True	False
75.0	3.2e-18	1.1e-18	9.6e-16	3.2e-16	3.1e-16	True	False
76.0	5.8e-18	1.9e-18	3.1e-15	1.0e-15	2.9e-16	True	False
77.0	2.6e-18	8.6e-19	6.9e-15	2.3e-15	2.8e-16	True	False
78.0	2.7e-18	9.0e-19	5.5e-15	1.8e-15	2.9e-16	True	False
79.0	3.0e-18	1.0e-18	2.6e-15	8.7e-16	2.7e-16	True	False
80.0	4.4e-18	1.5e-18	1.8e-15	5.9e-16	2.3e-16	True	False
81.0	3.3e-18	1.1e-18	3.4e-16	1.1e-16	2.2e-16	True	False
82.0	2.8e-18	9.3e-19	2.6e-15	8.8e-16	2.1e-16	True	False
83.0	3.3e-18	1.1e-18	8.2e-16	2.7e-16	1.3e-16	True	False
84.0	3.3e-18	1.1e-18	2.8e-15	9.5e-16	2.1e-16	True	False
85.0	1.9e-18	6.5e-19	5.1e-15	1.7e-15	2.5e-16	True	False
86.0	5.2e-17	1.7e-17	1.9e-15	6.5e-16	1.3e-16	True	False
87.0	4.0e-18	1.3e-18	8.8e-16	2.9e-16	1.7e-16	True	False
88.0	3.3e-18	1.1e-18	7.3e-16	2.4e-16	2.1e-16	True	False
89.0	3.0e-18	9.9e-19	7.3e-16	2.4e-16	1.9e-16	True	False
90.0	3.4e-18	1.1e-18	2.9e-15	9.6e-16	2.4e-16	True	False
91.0	7.4e-17	2.5e-17	2.9e-15	9.7e-16	2.0e-16	True	False
92.0	3.7e-18	1.2e-18	1.9e-15	6.3e-16	1.1e-16	True	False
93.0	8.2e-18	2.7e-18	2.3e-15	7.6e-16	1.1e-16	True	False
94.0	3.4e-18	1.1e-18	2.2e-15	7.5e-16	2.6e-16	True	False
95.0	2.9e-18	9.7e-19	1.9e-15	6.4e-16	1.3e-16	True	False
96.0	1.1e-17	3.8e-18	2.8e-15	9.5e-16	1.1e-16	True	False
97.0	2.9e-18	9.5e-19	1.9e-15	6.3e-16	1.0e-16	True	False
98.0	2.9e-18	9.7e-19	5.7e-15	1.9e-15	3.1e-16	True	False
99.0	2.9e-18	9.6e-19	1.1e-15	3.5e-16	9.9e-17	True	False
100.0	3.4e-17	1.1e-17	2.6e-15	8.7e-16	1.9e-16	True	False
101.0	2.9e-18	9.7e-19	3.5e-15	1.2e-15	1.9e-16	True	False
102.0	2.6e-18	8.7e-19	1.7e-15	5.8e-16	1.4e-16	True	False
103.0	3.8e-18	1.3e-18	5.4e-16	1.8e-16	1.5e-16	True	False
104.0	3.2e-18	1.1e-18	8.5e-16	2.8e-16	1.2e-16	True	False
105.0	2.9e-18	9.6e-19	2.0e-15	6.7e-16	1.4e-16	True	False
106.0	6.5e-17	2.2e-17	2.6e-15	8.7e-16	1.4e-16	True	False
107.0	4.2e-18	1.4e-18	4.3e-15	1.4e-15	1.1e-16	True	False
108.0	2.7e-18	9.1e-19	1.8e-15	6.0e-16	1.1e-16	True	False
109.0	2.7e-18	8.9e-19	2.7e-15	8.9e-16	2.2e-16	True	False
110.0	3.2e-18	1.1e-18	3.5e-15	1.2e-15	2.1e-16	True	False
111.0	3.2e-18	1.1e-18	3.5e-15	1.2e-15	2.0e-16	True	False
112.0	4.2e-18	1.4e-18	6.3e-15	2.1e-15	4.1e-16	True	False
113.0	3.4e-18	1.1e-18	1.8e-15	6.0e-16	1.8e-16	True	False
114.0	2.6e-18	8.6e-19	2.5e-15	8.5e-16	1.4e-16	True	False
115.0	3.4e-18	1.1e-18	3.5e-15	1.2e-15	1.4e-16	True	False
116.0	9.4e-18	3.1e-18	4.4e-15	1.5e-15	1.7e-16	True	False
117.0	2.8e-18	9.2e-19	5.7e-15	1.9e-15	1.3e-16	True	False

118.0	3.0e-18	9.9e-19	1.1e-15	3.8e-16	1.3e-16	True	False
119.0	2.9e-18	9.6e-19	6.7e-15	2.2e-15	2.8e-16	True	False
120.0	6.7e-18	2.2e-18	6.6e-16	2.2e-16	9.0e-17	True	False
121.0	2.5e-18	8.5e-19	1.2e-15	4.0e-16	9.4e-17	True	False
122.0	3.3e-18	1.1e-18	1.3e-14	4.4e-15	2.6e-16	True	False
123.0	3.6e-18	1.2e-18	2.9e-15	9.7e-16	3.1e-16	True	False
124.0	1.4e-17	4.8e-18	2.0e-15	6.5e-16	2.6e-16	True	False
125.0	6.7e-18	2.2e-18	1.2e-15	4.0e-16	1.4e-16	True	False
126.0	7.0e-18	2.3e-18	9.0e-15	3.0e-15	2.8e-16	True	False
127.0	3.0e-18	1.0e-18	3.1e-15	1.0e-15	1.6e-16	True	False
128.0	2.8e-18	9.5e-19	2.2e-15	7.2e-16	1.4e-16	True	False
129.0	2.8e-18	9.4e-19	2.2e-15	7.3e-16	1.8e-16	True	False
130.0	4.8e-18	1.6e-18	1.4e-15	4.6e-16	1.5e-16	True	False
131.0	3.5e-18	1.2e-18	5.5e-16	1.8e-16	1.2e-16	True	False
132.0	3.0e-18	9.9e-19	1.0e-15	3.4e-16	1.4e-16	True	False
133.0	1.7e-17	5.6e-18	9.7e-16	3.2e-16	2.1e-16	True	False
134.0	1.3e-17	4.5e-18	2.9e-15	9.7e-16	2.6e-16	True	False
135.0	2.6e-18	8.7e-19	4.6e-15	1.5e-15	1.6e-16	True	False
136.0	4.5e-18	1.5e-18	4.0e-15	1.3e-15	1.6e-16	True	False
137.0	1.2e-17	3.9e-18	4.4e-15	1.5e-15	1.1e-16	True	False
138.0	2.5e-18	8.5e-19	4.5e-15	1.5e-15	3.3e-16	True	False
139.0	4.0e-18	1.3e-18	3.2e-15	1.1e-15	2.6e-16	True	False
140.0	2.9e-18	9.7e-19	3.5e-15	1.2e-15	2.3e-16	True	False
141.0	3.7e-18	1.2e-18	5.1e-15	1.7e-15	1.6e-16	True	False

[NII] 6583$\mathring{A}$

Star ID	*f(peak)* erg/Å/s/cm^2	Line peak RMS erg/Å/s/cm^2	F erg/s/cm^2	ΔF_{RMS} erg/s/cm^2	ΔF_{sky} erg/s/cm^2	Upper limit	Good flux
0.0	3.2e-18	1.1e-18	1.2e-15	3.8e-16	8.1e-16	True	False
1.0	5.8e-16	1.9e-16	4.8e-14	1.6e-14	9.4e-16	True	False
2.0	1.4e-17	4.5e-18	3.2e-15	1.1e-15	6.9e-16	True	False
3.0	2.9e-18	9.6e-19	3.0e-15	1.0e-15	7.2e-16	True	False
4.0	8.5e-18	2.8e-18	9.4e-15	3.1e-15	7.7e-16	True	False
5.0	3.0e-18	9.9e-19	1.7e-15	5.7e-16	6.1e-16	True	False
6.0	2.9e-18	9.8e-19	3.3e-15	1.1e-15	6.7e-16	True	False
7.0	3.4e-18	1.1e-18	7.6e-15	2.5e-15	7.9e-16	True	False
8.0	2.9e-18	9.7e-19	7.2e-15	2.4e-15	7.5e-16	True	False
9.0	4.9e-18	1.6e-18	3.6e-15	1.2e-15	5.8e-16	True	False
10.0	4.9e-18	1.6e-18	2.3e-15	7.5e-16	5.6e-16	True	False
11.0	7.1e-18	2.4e-18	1.4e-15	4.7e-16	4.9e-16	True	False
12.0	8.7e-18	2.9e-18	7.8e-16	2.6e-16	6.2e-16	True	False
13.0	3.4e-18	1.1e-18	2.6e-15	8.5e-16	4.9e-16	True	False
14.0	2.9e-18	9.6e-19	9.1e-15	3.0e-15	9.0e-16	True	False
15.0	7.1e-18	2.4e-18	6.3e-16	2.1e-16	4.5e-16	True	False
16.0	4.4e-18	1.5e-18	1.9e-15	6.5e-16	5.1e-16	True	False
17.0	4.9e-18	1.6e-18	6.7e-15	2.2e-15	5.5e-16	True	False
18.0	1.4e-17	4.5e-18	1.6e-15	5.5e-16	6.4e-16	True	False
19.0	4.0e-18	1.3e-18	3.9e-15	1.3e-15	7.6e-16	True	False
20.0	2.8e-18	9.3e-19	3.3e-15	1.1e-15	7.1e-16	True	False
21.0	2.6e-18	8.6e-19	3.1e-15	1.0e-15	5.6e-16	True	False
22.0	5.2e-18	1.7e-18	3.2e-15	1.1e-15	7.1e-16	True	False
23.0	3.3e-18	1.1e-18	4.8e-15	1.6e-15	6.3e-16	True	False
24.0	5.6e-18	1.9e-18	3.6e-15	1.2e-15	5.9e-16	True	False
25.0	7.4e-18	2.5e-18	4.9e-15	1.6e-15	6.5e-16	True	False
26.0	2.9e-18	9.8e-19	1.3e-15	4.3e-16	4.8e-16	True	False
27.0	3.3e-17	1.1e-17	7.3e-15	2.4e-15	6.2e-16	True	False
28.0	8.6e-18	2.9e-18	2.1e-15	7.1e-16	5.4e-16	True	False
29.0	3.3e-17	1.1e-17	2.1e-15	7.0e-16	6.3e-16	True	False
30.0	4.3e-18	1.4e-18	3.4e-15	1.1e-15	6.1e-16	True	False
31.0	3.9e-18	1.3e-18	3.8e-15	1.3e-15	7.9e-16	True	False
32.0	3.2e-18	1.1e-18	3.0e-15	1.0e-15	5.4e-16	True	False
33.0	4.4e-18	1.5e-18	2.1e-15	7.0e-16	7.4e-16	True	False
34.0	1.3e-17	4.4e-18	3.4e-15	1.1e-15	6.5e-16	True	False
35.0	6.8e-18	2.3e-18	1.4e-15	4.7e-16	6.6e-16	True	False
36.0	4.6e-18	1.5e-18	5.7e-15	1.9e-15	6.0e-16	True	False
37.0	3.0e-18	9.9e-19	4.6e-15	1.5e-15	7.9e-16	True	False
38.0	6.4e-18	2.1e-18	1.7e-15	5.6e-16	7.3e-16	True	False
39.0	4.2e-18	1.4e-18	2.4e-15	8.1e-16	6.0e-16	True	False
40.0	3.2e-18	1.1e-18	4.6e-15	1.5e-15	8.0e-16	True	False
41.0	2.9e-18	9.6e-19	8.7e-15	2.9e-15	9.7e-16	True	False
42.0	2.9e-18	9.7e-19	2.4e-15	8.1e-16	7.6e-16	True	False
43.0	4.2e-18	1.4e-18	2.0e-15	6.5e-16	6.6e-16	True	False
44.0	3.9e-18	1.3e-18	2.3e-15	7.7e-16	7.6e-16	True	False
45.0	2.9e-18	9.8e-19	5.8e-15	1.9e-15	7.3e-16	True	False
46.0	1.2e-17	4.0e-18	2.0e-15	6.6e-16	7.2e-16	True	False
47.0	3.5e-18	1.2e-18	3.7e-15	1.2e-15	7.4e-16	True	False
48.0	2.7e-18	9.0e-19	4.4e-15	1.5e-15	7.7e-16	True	False
49.0	4.8e-18	1.6e-18	2.2e-15	7.4e-16	1.1e-15	True	False
50.0	3.1e-18	1.0e-18	3.5e-15	1.2e-15	1.0e-15	True	False
51.0	7.5e-18	2.5e-18	1.5e-15	5.0e-16	7.2e-16	True	False
52.0	4.9e-18	1.6e-18	3.2e-15	1.1e-15	7.9e-16	True	False
53.0	2.6e-18	8.6e-19	2.8e-15	9.3e-16	7.3e-16	True	False
54.0	1.0e-16	3.5e-17	2.5e-14	8.3e-15	6.5e-16	True	False
55.0	9.0e-18	3.0e-18	3.3e-15	1.1e-15	1.1e-15	True	False

56.0	4.1e-18	1.4e-18	4.2e-15	1.4e-15	8.6e-16	True	False
57.0	8.8e-18	2.9e-18	1.6e-15	5.4e-16	6.6e-16	True	False
58.0	4.0e-18	1.3e-18	9.0e-15	3.0e-15	7.9e-16	True	False
59.0	8.1e-18	2.7e-18	3.6e-15	1.2e-15	6.0e-16	True	False
60.0	1.6e-17	5.4e-18	2.0e-15	6.6e-16	5.4e-16	True	False
61.0	3.0e-18	9.9e-19	3.7e-15	1.2e-15	6.0e-16	True	False
62.0	3.5e-18	1.2e-18	1.7e-15	5.5e-16	9.7e-16	True	False
63.0	3.5e-18	1.2e-18	2.2e-15	7.2e-16	1.2e-15	True	False
64.0	3.7e-18	1.2e-18	1.0e-14	3.4e-15	7.4e-16	True	False
65.0	4.3e-18	1.4e-18	1.7e-15	5.5e-16	7.2e-16	True	False
66.0	4.0e-18	1.3e-18	3.5e-15	1.2e-15	6.9e-16	True	False
67.0	9.4e-18	3.1e-18	8.2e-16	2.7e-16	6.1e-16	True	False
68.0	3.7e-18	1.2e-18	3.2e-15	1.1e-15	1.2e-15	True	False
69.0	4.1e-18	1.4e-18	1.7e-15	5.8e-16	8.9e-16	True	False
70.0	6.7e-17	2.2e-17	2.6e-15	8.6e-16	6.5e-16	True	False
71.0	9.4e-16	3.1e-16	1.8e-13	6.1e-14	8.9e-16	True	False
72.0	1.3e-17	4.4e-18	3.3e-15	1.1e-15	8.9e-16	True	False
73.0	8.0e-18	2.7e-18	9.6e-16	3.2e-16	6.7e-16	True	False
74.0	3.7e-16	1.5e-18	1.0e-15	2.7e-16	8.3e-16	False	False
75.0	3.3e-18	1.1e-18	1.1e-15	3.6e-16	9.0e-16	True	False
76.0	6.1e-18	2.0e-18	3.6e-15	1.2e-15	9.0e-16	True	False
77.0	2.5e-18	8.3e-19	8.0e-15	2.7e-15	8.3e-16	True	False
78.0	2.8e-18	9.3e-19	6.3e-15	2.1e-15	8.5e-16	True	False
79.0	3.0e-18	1.0e-18	3.1e-15	1.0e-15	7.3e-16	True	False
80.0	3.6e-18	1.2e-18	2.0e-15	6.8e-16	6.6e-16	True	False
81.0	2.9e-18	9.8e-19	3.8e-16	1.3e-16	7.3e-16	True	False
82.0	2.8e-18	9.2e-19	3.1e-15	1.0e-15	6.4e-16	True	False
83.0	3.3e-18	1.1e-18	9.0e-16	3.0e-16	3.3e-16	True	False
84.0	3.3e-18	1.1e-18	3.3e-15	1.1e-15	5.9e-16	True	False
85.0	2.0e-18	6.5e-19	5.9e-15	2.0e-15	8.1e-16	True	False
86.0	5.2e-17	1.7e-17	2.3e-15	7.8e-16	3.4e-16	True	False
87.0	4.0e-18	1.3e-18	7.8e-16	2.6e-16	4.8e-16	True	False
88.0	3.1e-18	1.0e-18	7.6e-16	2.5e-16	5.6e-16	True	False
89.0	3.1e-18	1.0e-18	7.6e-16	2.5e-16	5.5e-16	True	False
90.0	3.1e-18	1.0e-18	3.3e-15	1.1e-15	7.0e-16	True	False
91.0	7.2e-17	2.4e-17	3.3e-15	1.1e-15	6.1e-16	True	False
92.0	3.5e-18	1.2e-18	2.2e-15	7.4e-16	3.1e-16	True	False
93.0	6.3e-18	2.1e-18	2.6e-15	8.7e-16	3.4e-16	True	False
94.0	3.4e-18	1.1e-18	2.5e-15	8.5e-16	8.2e-16	True	False
95.0	2.8e-18	9.4e-19	2.3e-15	7.5e-16	3.5e-16	True	False
96.0	9.3e-18	3.1e-18	3.3e-15	1.1e-15	3.2e-16	True	False
97.0	2.9e-18	9.7e-19	2.2e-15	7.3e-16	3.0e-16	True	False
98.0	2.8e-18	9.5e-19	6.6e-15	2.2e-15	1.0e-15	True	False
99.0	2.8e-18	9.4e-19	1.2e-15	4.0e-16	2.8e-16	True	False
100.0	2.9e-17	9.7e-18	3.1e-15	1.0e-15	6.2e-16	True	False
101.0	2.7e-18	9.1e-19	4.0e-15	1.3e-15	5.9e-16	True	False
102.0	2.6e-18	8.7e-19	2.0e-15	6.7e-16	4.2e-16	True	False
103.0	3.8e-18	1.3e-18	6.3e-16	2.1e-16	4.6e-16	True	False
104.0	3.4e-18	1.1e-18	9.8e-16	3.3e-16	3.5e-16	True	False
105.0	2.9e-18	9.8e-19	2.3e-15	7.6e-16	3.7e-16	True	False
106.0	5.1e-17	1.7e-17	3.1e-15	1.0e-15	4.2e-16	True	False
107.0	4.4e-18	1.5e-18	5.0e-15	1.7e-15	3.3e-16	True	False
108.0	2.8e-18	9.3e-19	2.1e-15	7.0e-16	3.0e-16	True	False
109.0	2.6e-18	8.7e-19	3.1e-15	1.0e-15	6.7e-16	True	False
110.0	3.2e-18	1.1e-18	4.1e-15	1.4e-15	6.8e-16	True	False
111.0	3.2e-18	1.1e-18	4.1e-15	1.4e-15	6.1e-16	True	False
112.0	4.3e-18	1.4e-18	7.3e-15	2.4e-15	1.3e-15	True	False
113.0	3.2e-18	1.1e-18	2.1e-15	6.9e-16	5.4e-16	True	False
114.0	2.7e-18	8.9e-19	2.9e-15	9.7e-16	4.2e-16	True	False
115.0	3.4e-18	1.1e-18	4.1e-15	1.4e-15	4.3e-16	True	False
116.0	8.6e-18	2.9e-18	5.2e-15	1.7e-15	5.6e-16	True	False
117.0	2.8e-18	9.2e-19	6.7e-15	2.2e-15	3.6e-16	True	False

118.0	2.8e-18	9.4e-19	1.3e-15	4.4e-16	3.8e-16	True	False
119.0	3.0e-18	1.0e-18	7.9e-15	2.6e-15	9.1e-16	True	False
120.0	6.7e-18	2.2e-18	7.6e-16	2.5e-16	2.5e-16	True	False
121.0	2.5e-18	8.4e-19	1.4e-15	4.7e-16	2.7e-16	True	False
122.0	3.3e-18	1.1e-18	1.5e-14	5.1e-15	8.6e-16	True	False
123.0	3.2e-18	1.1e-18	3.3e-15	1.1e-15	9.5e-16	True	False
124.0	1.1e-17	3.6e-18	2.2e-15	7.3e-16	8.2e-16	True	False
125.0	6.7e-18	2.2e-18	1.4e-15	4.6e-16	4.3e-16	True	False
126.0	7.3e-18	2.4e-18	1.1e-14	3.5e-15	9.1e-16	True	False
127.0	3.1e-18	1.0e-18	3.5e-15	1.2e-15	4.8e-16	True	False
128.0	2.6e-18	8.8e-19	2.5e-15	8.4e-16	4.0e-16	True	False
129.0	2.8e-18	9.4e-19	2.5e-15	8.3e-16	6.0e-16	True	False
130.0	4.8e-18	1.6e-18	1.5e-15	5.0e-16	4.6e-16	True	False
131.0	3.6e-18	1.2e-18	6.2e-16	2.1e-16	3.6e-16	True	False
132.0	2.9e-18	9.7e-19	1.1e-15	3.6e-16	4.6e-16	True	False
133.0	1.5e-17	5.0e-18	1.1e-15	3.6e-16	6.3e-16	True	False
134.0	1.2e-17	4.2e-18	3.4e-15	1.1e-15	7.8e-16	True	False
135.0	2.6e-18	8.7e-19	5.3e-15	1.8e-15	4.6e-16	True	False
136.0	4.6e-18	1.5e-18	4.7e-15	1.6e-15	4.8e-16	True	False
137.0	1.1e-17	3.7e-18	5.2e-15	1.7e-15	3.0e-16	True	False
138.0	2.5e-18	8.5e-19	5.2e-15	1.7e-15	1.0e-15	True	False
139.0	3.8e-18	1.3e-18	3.7e-15	1.2e-15	8.2e-16	True	False
140.0	1.9e-18	6.4e-19	4.1e-15	1.4e-15	6.9e-16	True	False
141.0	3.3e-18	1.1e-18	5.6e-15	1.9e-15	4.6e-16	True	False

Appendix C

This appendix shows the integrated fluxes as a function of: the star effective temperature, the stellar mass, the FUV field in G_0 units and the bolometric luminosity of the star. These plots are listed for each line. Every page has a title in which is contained the name of the emission line and its wavelength. As for the plots shown in chapter 5, the blue dots are the so-called acceptable integrated flux values, the cyan dots are the integration results in which the line is detected but the sky subtraction brings uncertainties and the grey arrows are the upper limits. For some of the selected lines all the results are upper limits. Only two lines present some good integrated line fluxes results.

Hα 6583$\mathring{A}$

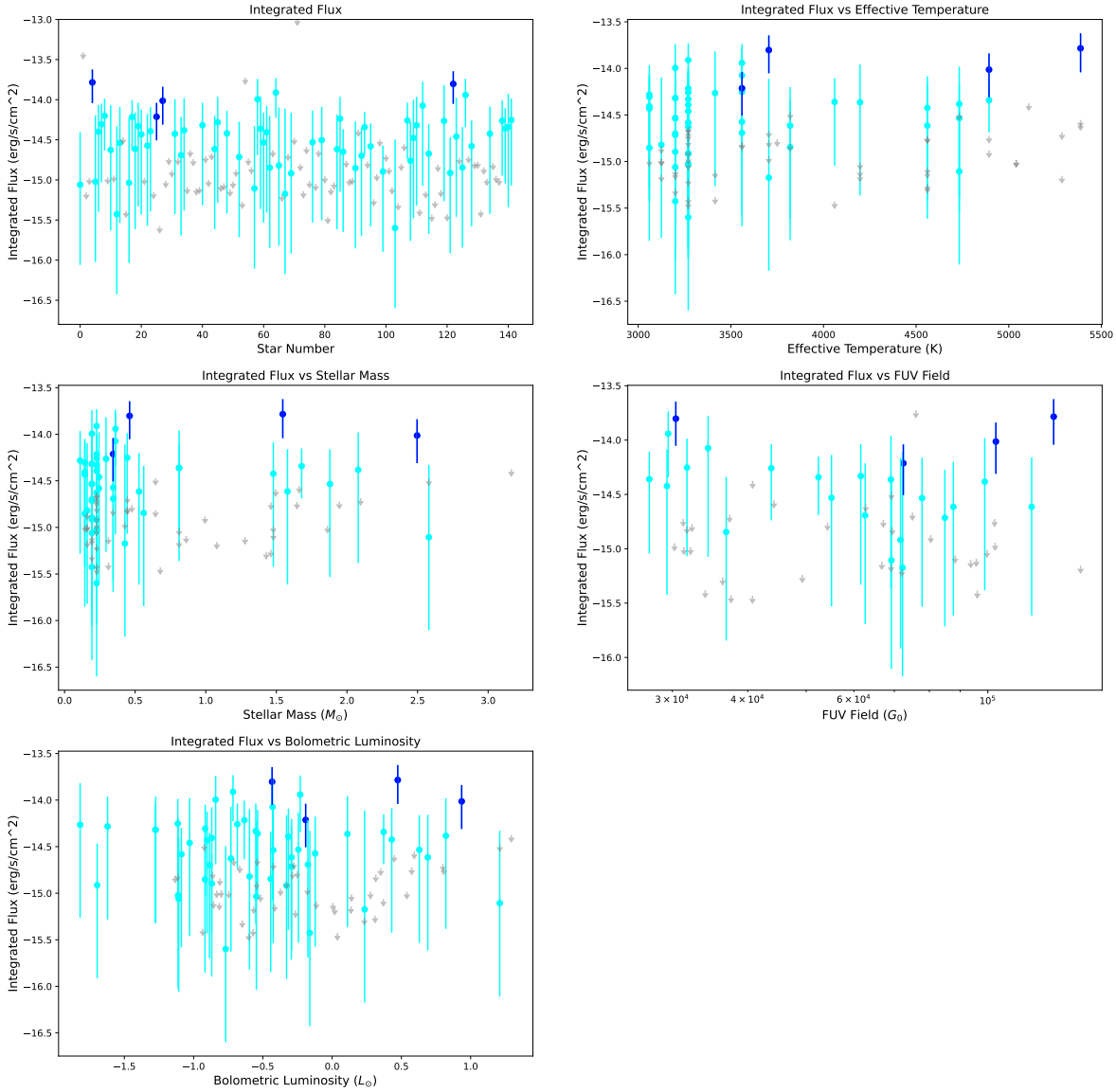

Figure C.1: *Top left: integrated flux results for each star; top right: integrated fluxes as a function of effective temperature; central left: integrated fluxes as a function of stellar mass; central right: integrated fluxes as function of FUV field and bottom left: integrated fluxes as function of the bolometric luminosity. Grey arrows are upper limits, cyan dots are the integrated flux results with large uncertainties and blue dots are the acceptable measurements.*

$\mathbf{H}\beta$ **4861**$\mathring{A}$

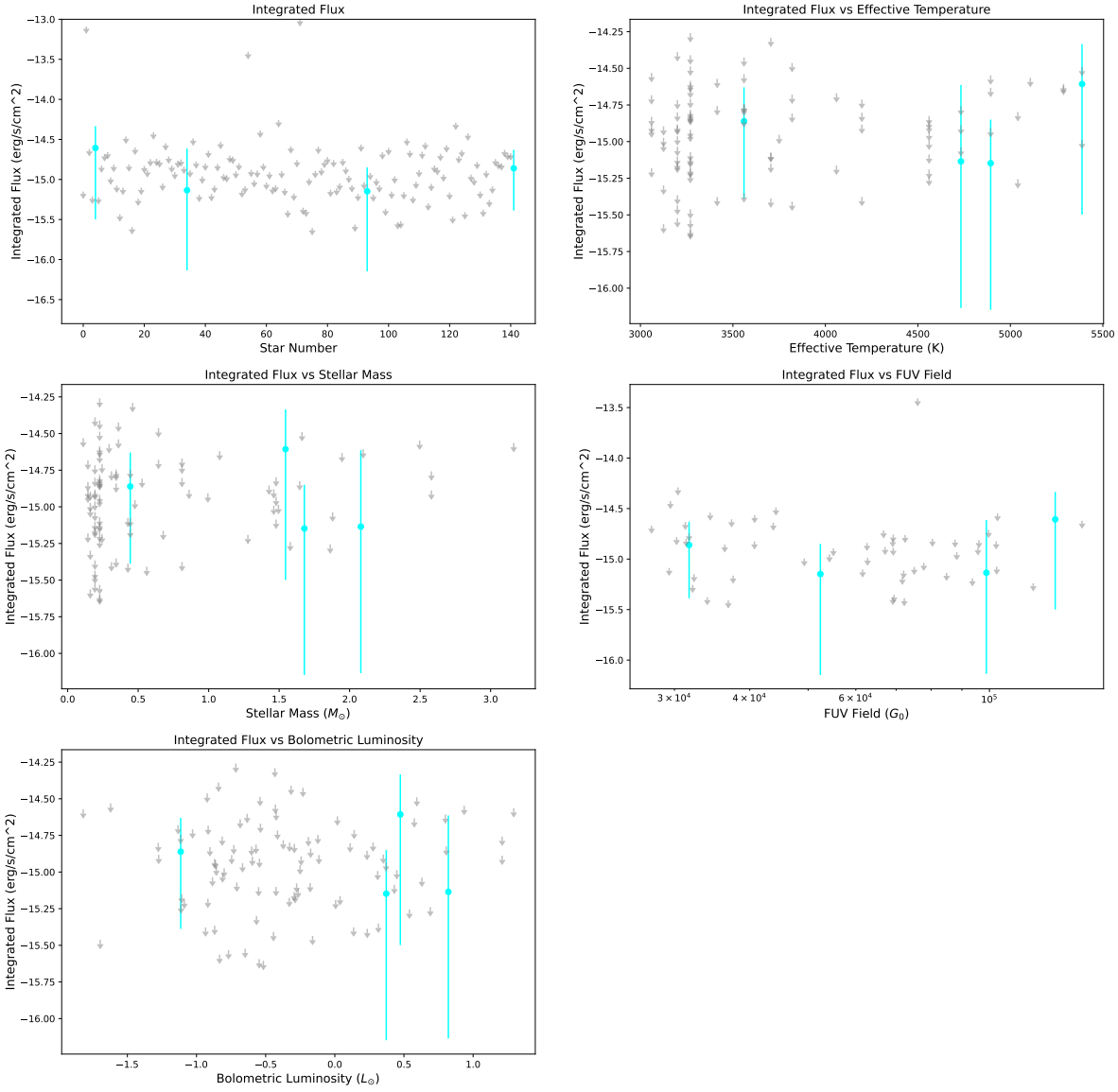

Figure C.2: *Same caption of figure C.1*

[OI] 6300$\AA$

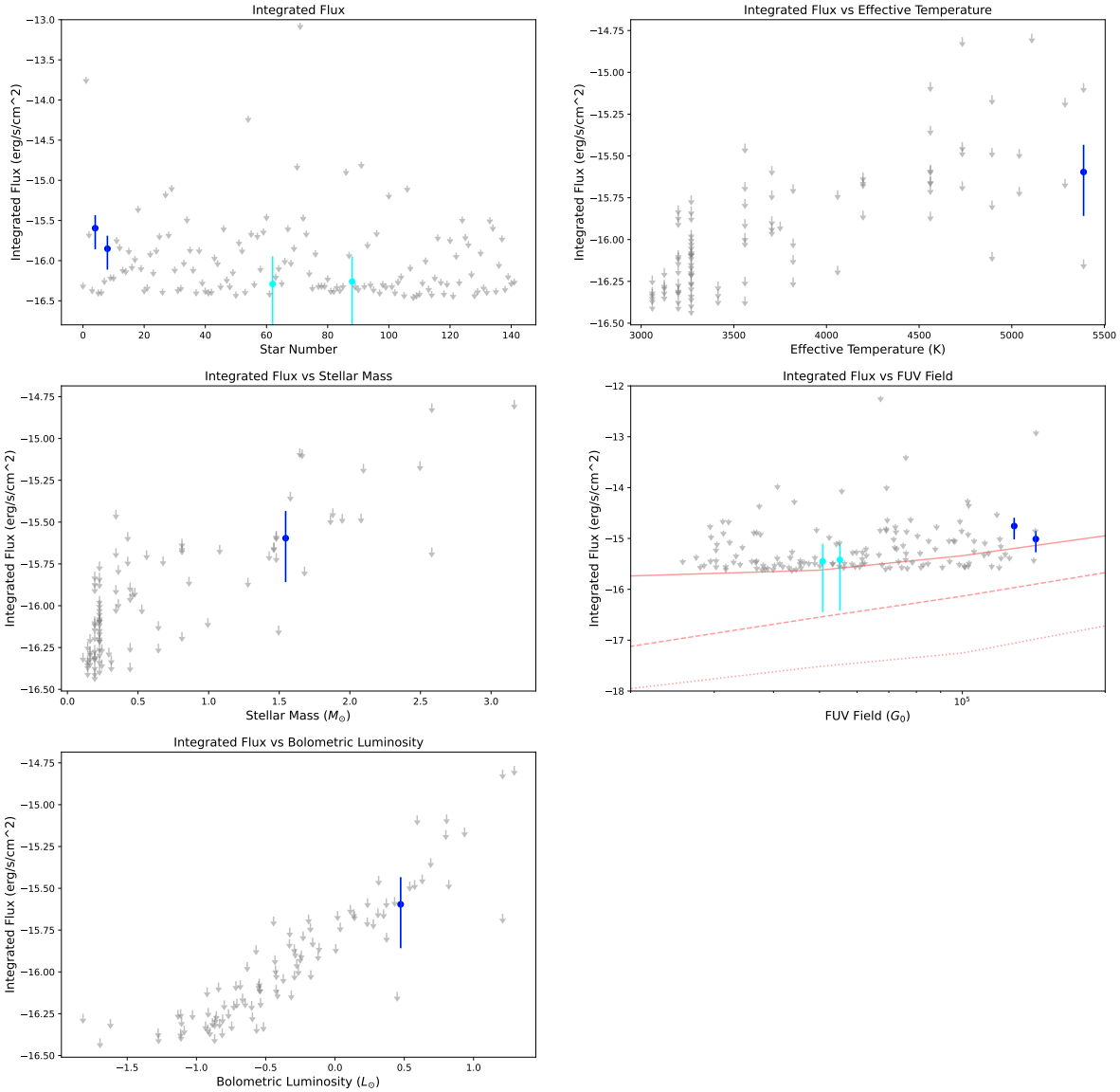

Figure C.3: *Same caption of figure C.1. The central right plot is the figure 5.1*

OI 8446$\mathring{A}$

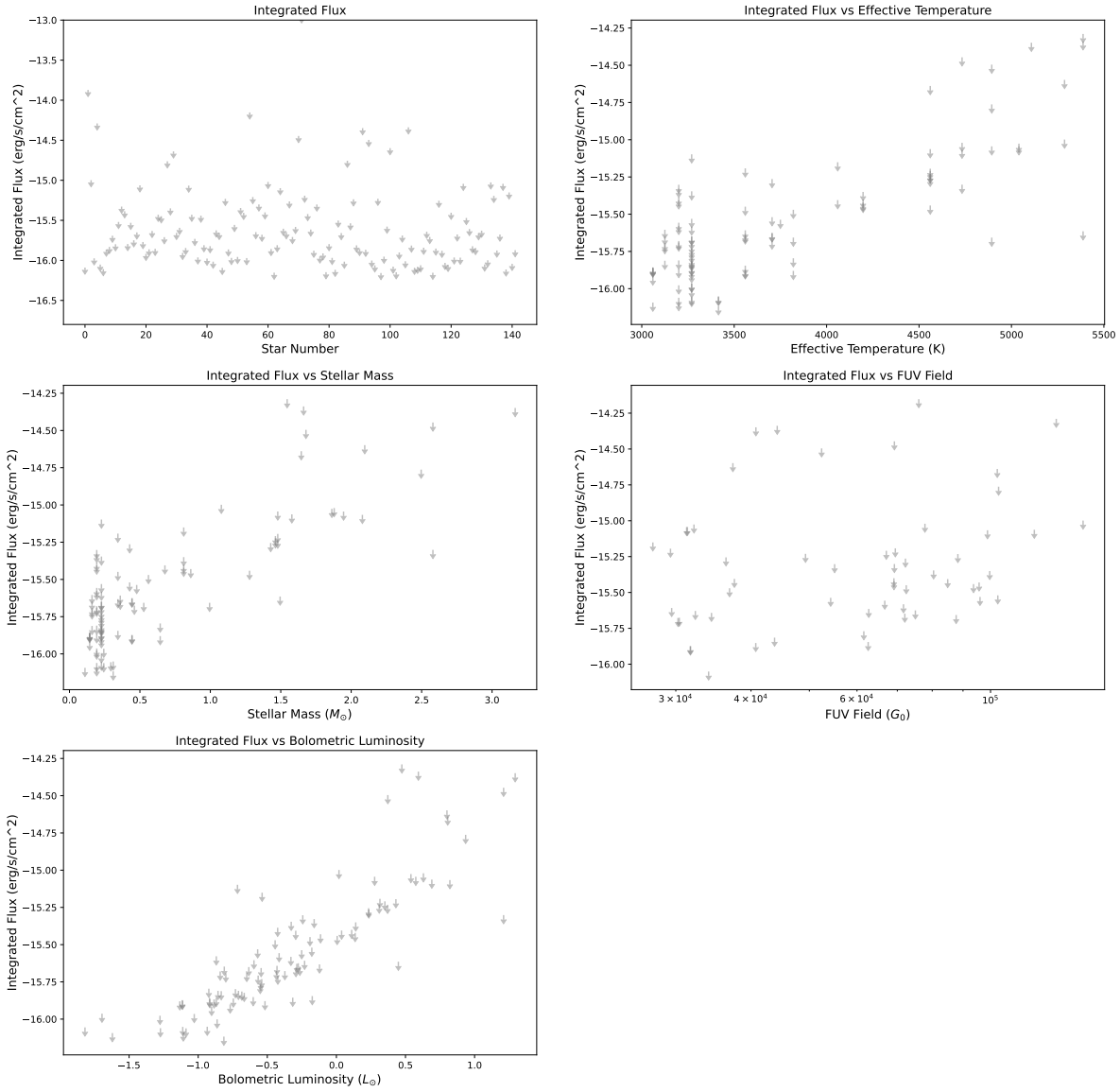

Figure C.4: *Same caption of figure C.1*

HeI 5876$\AA$

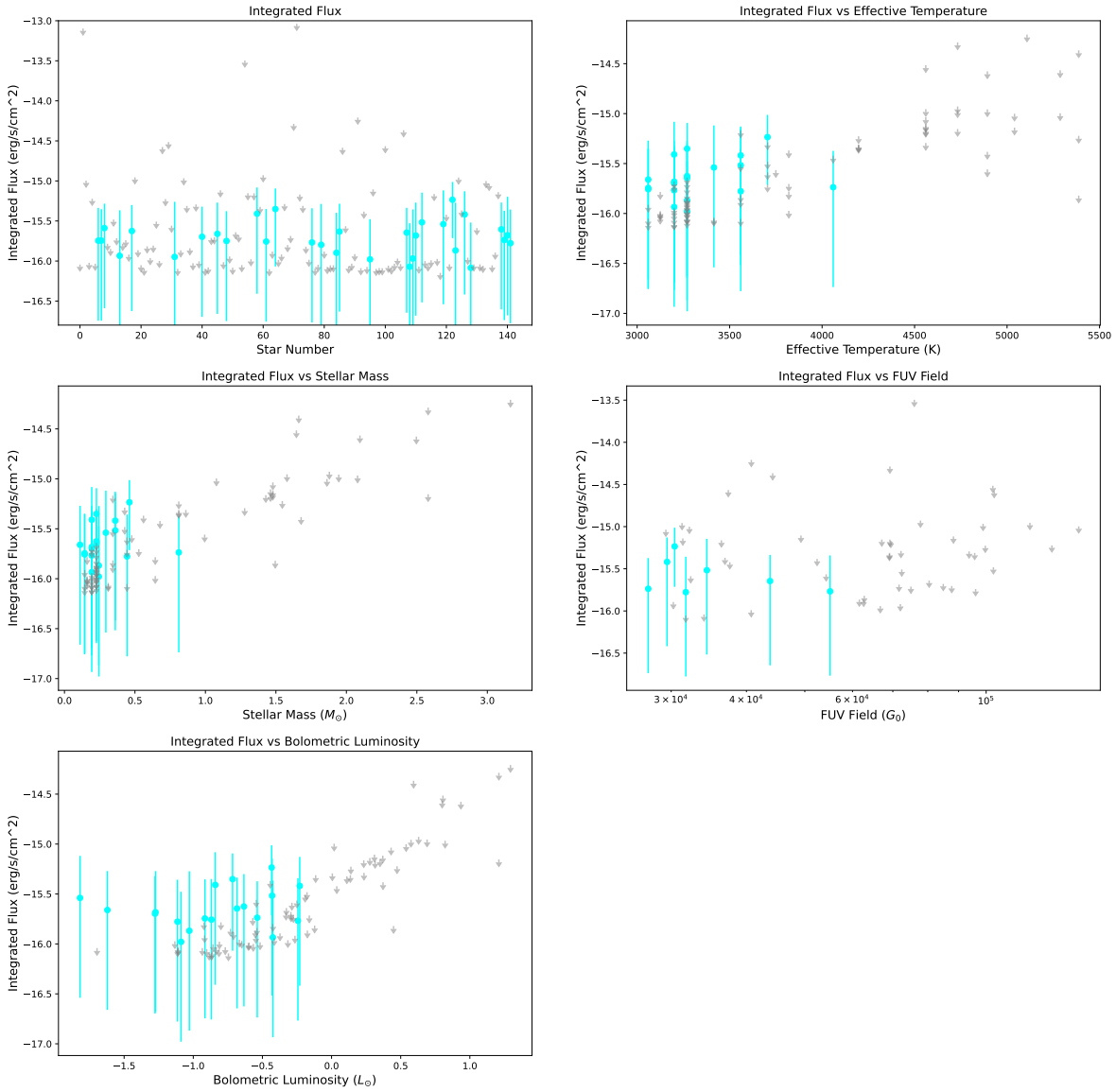

Figure C.5: *Same caption of figure C.1*

HeI 6678$\mathring{A}$

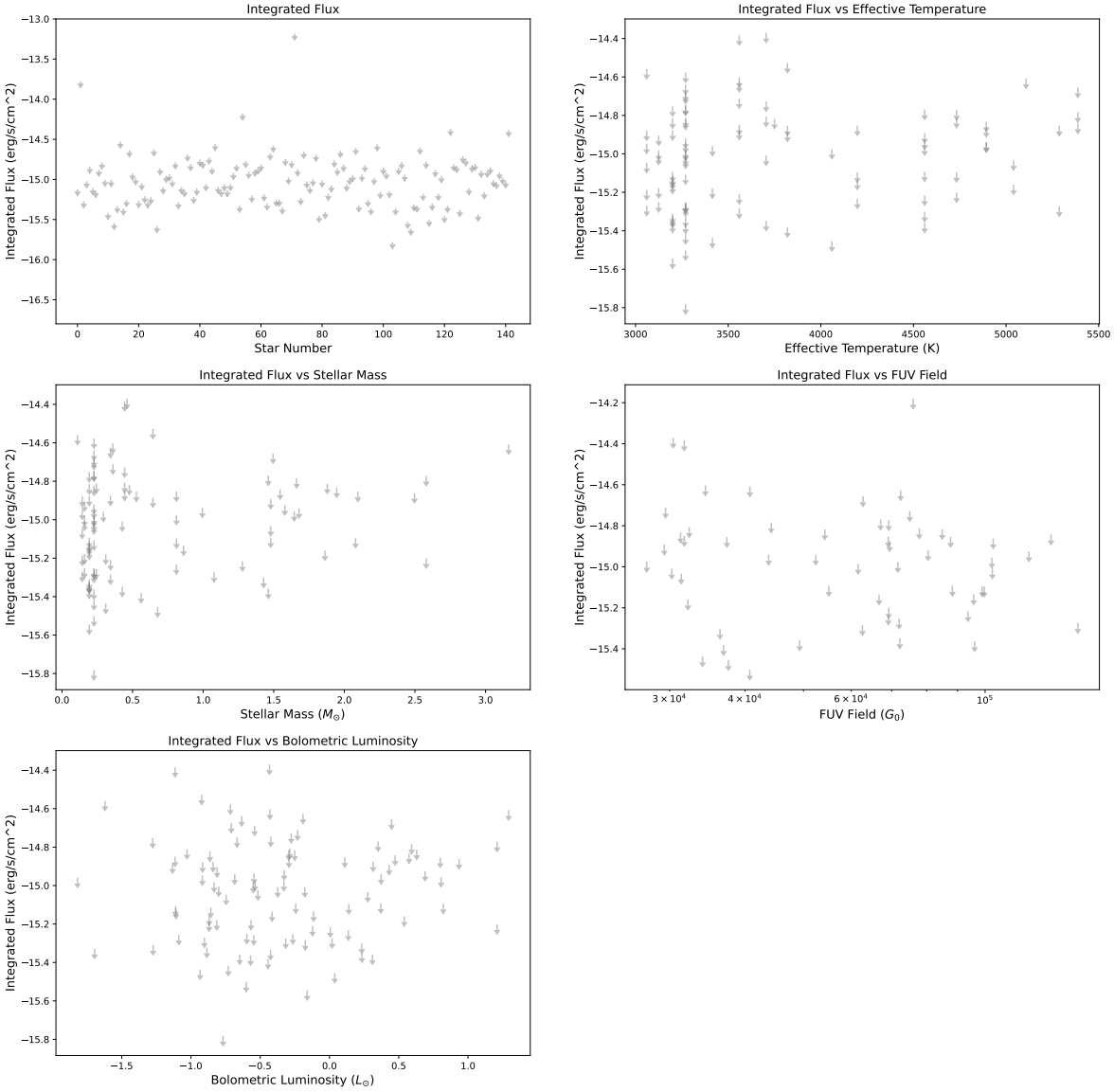

Figure C.6: *Same caption of figure C.1*

HeI 7065$\mathring{A}$

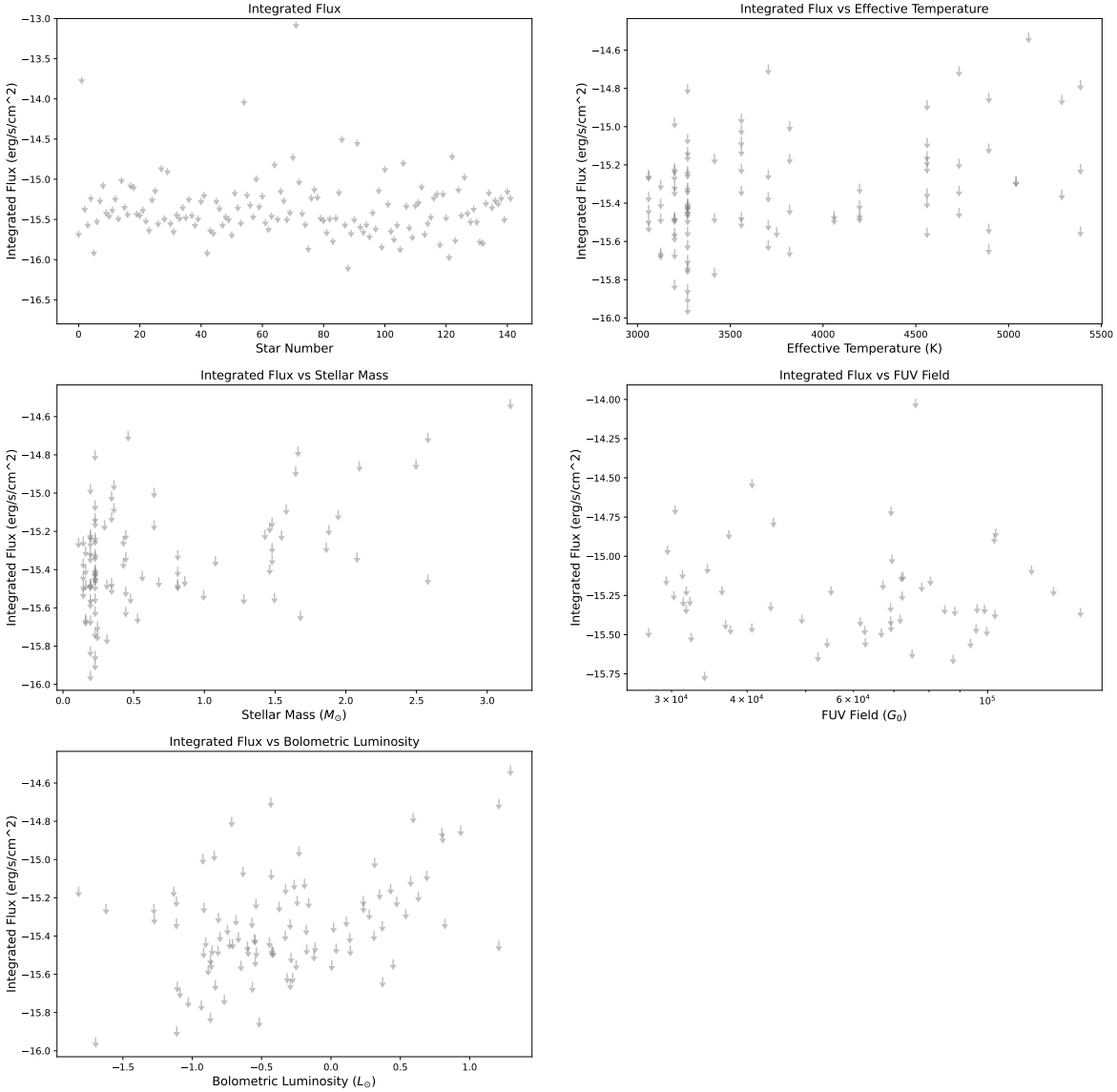

Figure C.7: *Same caption of figure C.1*

HeI 7281$\mathring{A}$

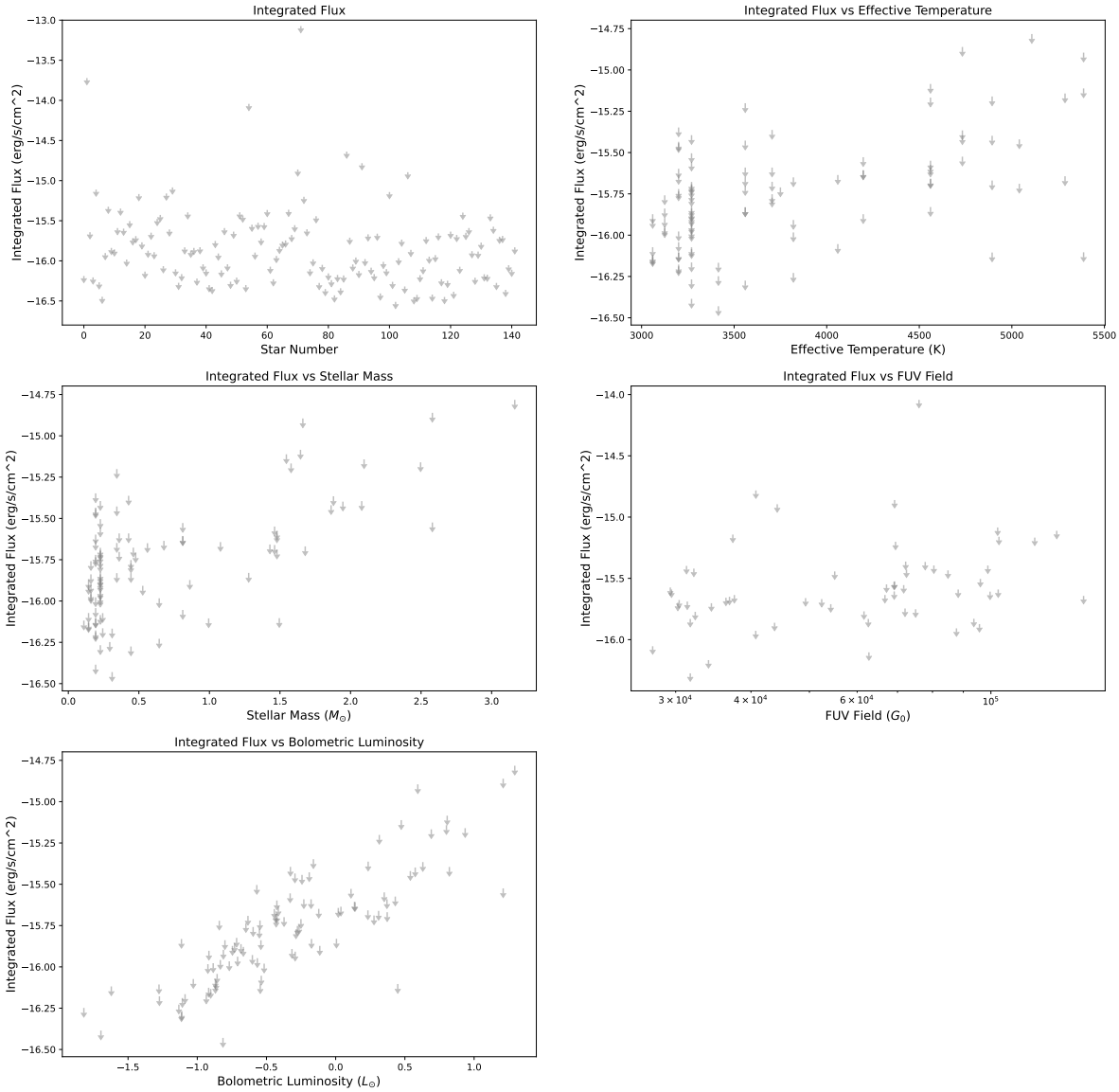

Figure C.8: *Same caption of figure C.1*

[NII] 6548$\mathring{A}$

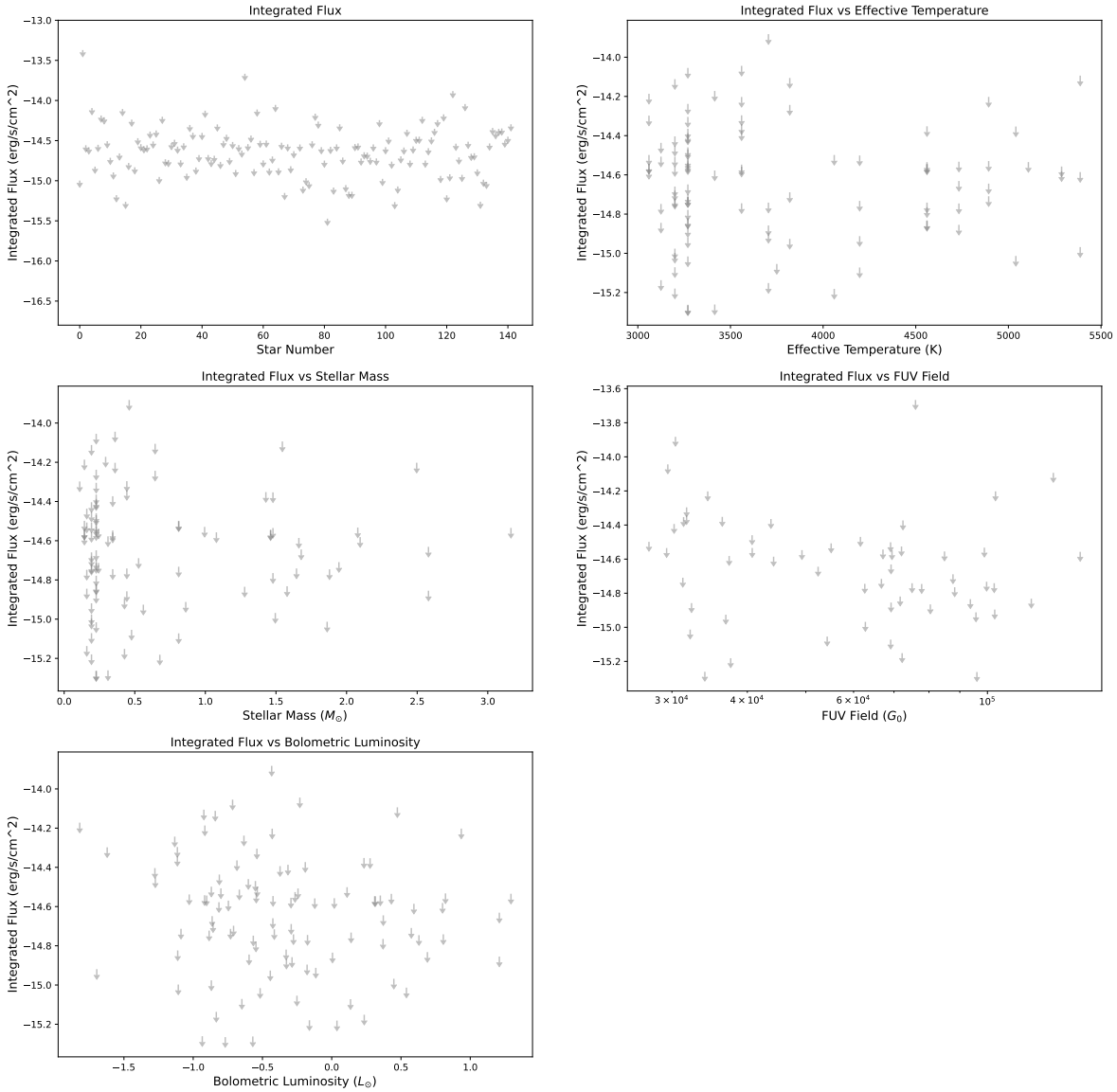

Figure C.9: *Same caption of figure C.1*

[NII] 6583$\mathring{A}$

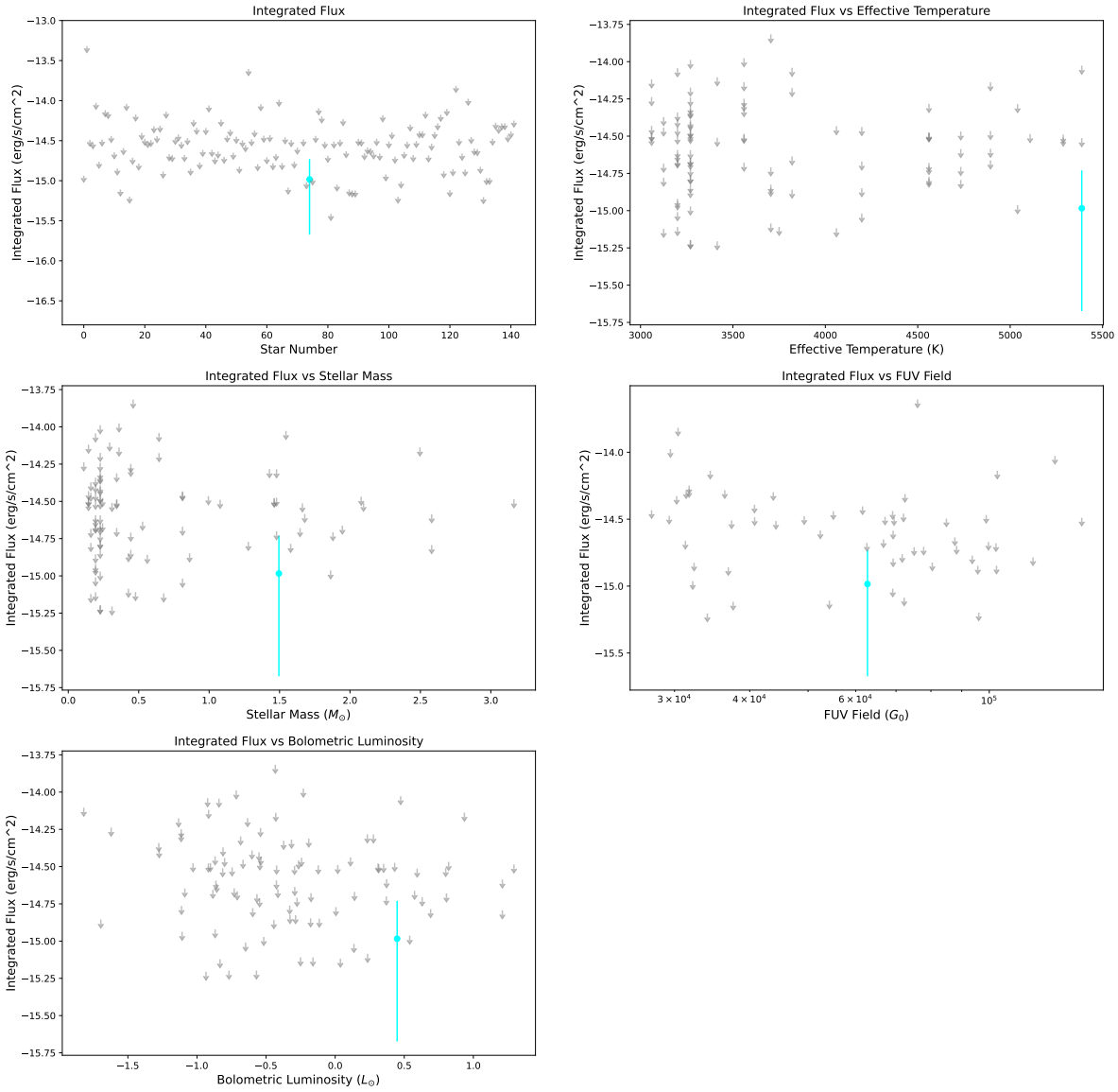

Figure C.10: *Same caption of figure C.1*

Bibliography

[1] Frank H. Shu, Fred C. Adams, and Susana Lizano. Star formation in molecular clouds: observation and theory. , 25:23–81, January 1987.

[2] W. D. Langer, T. Velusamy, T. B. H. Kuiper, S. Levin, E. Olsen, and V. Migenes. Study of Structure and Small-Scale Fragmentation in TMC-1. , 453:293, November 1995.

[3] A. Heithausen, F. Bensch, J. Stutzki, E. Falgarone, and J. F. Panis. The IRAM key project: small-scale structure of pre-star forming regions. Combined mass spectra and scaling laws. , 331:L65–L68, March 1998.

[4] Christopher F. McKee and Eve C. Ostriker. Theory of star formation. *Annual Review of Astronomy and Astrophysics*, 45(1):565–687, 2007.

[5] John J. Tobin, Lee Hartmann, Hsin-Fang Chiang, David J. Wilner, Leslie W. Looney, Laurent Loinard, Nuria Calvet, and Paola D'Alessio. Modeling the resolved disk around the class 0 protostar l1527. *The Astrophysical Journal*, 771(1):48, jun 2013.

[6] A. Frank, T. P. Ray, S. Cabrit, P. Hartigan, H. G. Arce, F. Bacciotti, J. Bally, M. Benisty, J. Eislöffel, M. Güdel, S. Lebedev, B. Nisini, and A. Raga. Jets and outflows from star to cloud: Observations confront theory. In *Protostars and Planets VI*. University of Arizona Press, 2014.

[7] A. J. Frost. *The circumstellar environment of massive young stellar objects - a multi-scale analysis*. PhD thesis, University of Leeds, UK, January 2020.

[8] D. Lynden-Bell and J. E. Pringle. The evolution of viscous discs and the origin of the nebular variables. , 168:603–637, September 1974.

[9] N. I. Shakura and R. A. Sunyaev. Black holes in binary systems. Observational appearance. , 24:337–355, January 1973.

[10] R. Alexander, I. Pascucci, S. Andrews, P. Armitage, and L. Cieza. The dispersal of protoplanetary disks. In *Protostars and Planets VI*. University of Arizona Press, 2014.

[11] Bradley S. Meyer. Accretion processes in star formation, 2nd edition, by lee hartmann. *Meteoritics & Planetary Science*, 44(4):621–621, 2009.

[12] Lee Hartmann, Gregory Herczeg, and Nuria Calvet. Accretion onto Pre-Main-Sequence Stars. , 54:135–180, September 2016.

[13] A J Winter, C J Clarke, G Rosotti, J Ih, S Facchini, and T J Haworth. Erratum to: Protoplanetary disc truncation mechanisms in stellar clusters: comparing external photoevaporation and tidal encounters. *Monthly Notices of the Royal Astronomical Society*, 480(4):5384–5384, 08 2018.

[14] Dominika Itrich, Leonardo Testi, Giacomo Beccari, Carlo F. Manara, Megan Reiter, Thomas Preibisch, Anna F. McLeod, Giovanni Rosotti, Ralf Klessen, Sergio Molinari, and Patrick Hennebelle. The population of young low-mass stars in Trumpler 14. *arXiv e-prints*, page arXiv:2309.14168, September 2023.

[15] C. Göppl and T. Preibisch. igaia/iEDR3 distances of the young stellar clusters in the extended carina nebula complex. *Astronomy &amp Astrophysics*, 660:A11, mar 2022.

[16] Nolan R. Walborn, Ian D. Howarth, Daniel J. Lennon, Philip Massey, M. S. Oey, Anthony F. J. Moffat, Gwen Skalkowski, Nidia I. Morrell, Laurent Drissen, and Joel Wm. Parker. A new spectral classification system for the earliest o stars: Definition of type o2. *The Astronomical Journal*, 123(5):2754, may 2002.

[17] N. Morrell, B. García, and H. Levato. Spectral morphology in the open clusters Tr 14 and Tr 15. *Boletin de la Asociacion Argentina de Astronomia La Plata Argentina*, 34:194–195, January 1988.

[18] Laura R. Penny, Douglas R. Gies, William I. Hartkopf, Brian D. Mason, and Nils H. Turner. The Frequency of Binary Stars in the Young Cluster Trumpler 14. , 105:588, June 1993.

[19] Philip Massey, Kathleen DeGioia-Eastwood, and Elizabeth Waterhouse. The progenitor masses of wolf-rayet stars and luminous blue variables determined from cluster turnoffs. ii. results from 12 galactic clusters and ob associations. *The Astronomical Journal*, 121(2):1050, feb 2001.

[20] A. Feinstein, H. G. Marraco, and J. C. Muzzio. A single young open cluster comprising TR 14 and TR 16. , 12:331, December 1973.

[21] Carraro, G., Romaniello, M., Ventura, P., and Patat, F. The star cluster collinder 232 in the carina complex and its relation to trumpler 14/16 ***. *A&A*, 418(2):525–537, 2004.

[22] R. A. Vazquez, G. Baume, A. Feinstein, and P. Prado. Investigation on the region of the open cluster Tr 14. , 116:75–94, March 1996.

[23] K. DeGioia-Eastwood, H. Throop, G. Walker, and K. M. Cudworth. The star formation history of trumpler 14 and trumpler 16. *The Astrophysical Journal*, 549(1):578, mar 2001.

[24] Mauricio Tapia, Miguel Roth, Rubén A. Vázquez, and Alejandro Feinstein. Imaging study of NGC 3372, the Carina nebula - I.

UBVRIJHK photometry of Tr 14, Tr 15, Tr 16 and Car I. , 339(1):44–62, February 2003.

[25] Leisa K. Townsley. Not Your Grandmother's HII Regions: An X-ray Tour of Massive Star-forming Regions. In *AAS/High Energy Astrophysics Division #9*, volume 9 of *AAS/High Energy Astrophysics Division*, page 3.01, September 2006.

[26] J. Ascenso, J. Alves, S. Vicente, and M. T. V. T. Lago. NTT and VLT diffraction limited imaging of Trumpler 14: revealing a massive core-halo cluster. , 476(1):199–215, December 2007.

[27] Nathan Smith and Kate J. Brooks. The carina nebula: A laboratory for feedback and triggered star formation, 2008.

[28] Peter B. Stetson. Daophot: A computer program for crowded-field stellar photometry. *Publications of the Astronomical Society of the Pacific*, 99(613):191, mar 1987.

[29] Giulia Ballabio, Thomas J. Haworth, and W. J. Henney. [O I] 6300 Å emission as a probe of external photoevaporation of protoplanetary discs. , 518(4):5563–5575, February 2023.

[30] Jason A. Cardelli, Geoffrey C. Clayton, and John S. Mathis. The Relationship between Infrared, Optical, and Ultraviolet Extinction. , 345:245, October 1989.

[31] A. Natta, L. Testi, J. M. Alcalá, E. Rigliaco, E. Covino, B. Stelzer, and V. D'Elia. X-shooter spectroscopy of young stellar objects. V. Slow winds in T Tauri stars. , 569:A5, September 2014.

Acknowledgement

I want to thank my supervisor Prof. Leonardo Tesi and co-supervisors Dr. Giacomo Beccari and Dr. Dominika Itrich for their kindness and availability. In these months of work, preparing the thesis, I have had the opportunity to learn many things about the topics covered. For the first time I was able to work like a real astrophysicist and I am grateful to you for having the patience to teach me how to approach a scientific study. This experience was truly formative for me and I am truly grateful to have met you.